Holographic Particle Image Velocimetry for Wall Turbulence Measurements

Juliana Kuhlmann Abrantes

N° d'ordre: 178

ÉCOLE CENTRALE DE LILLE

THÈSE

présentée en vue
d'obtenir le grade de

DOCTEUR

en

Mécanique

par

Juliana Kuhlmann Abrantes

DOCTORAT DELIVRÉ SIMULTANEMENT PAR L'ÉCOLE CENTRALE DE LILLE ET LA PUC-RIO DANS LE CADRE D'UNE COTUTELLE INTERNATIONALE DE THÈSE

Titre de la Thèse:

Vélocimétrie par Image de Particules Holographique pour les Mesures de Turbulence de Paroi

Soutenue le 30 mars 2012 devant le jury d'examen:

Président	M. Paulo Roberto de Souza Mendes, Professeur, PUC-Rio, Brésil
Rapporteur	M. Joseph Katz, Professeur, Johns Hopkins, Baltimore, États Unis
Rapporteur	M. Átila Pantaleão Silva Freire, Professeur, COPPE/UFRJ, Brésil
Examinateur	M. Francisco Ricardo da Cunha, Professeur, UnB, Brésil
Examinateur	M. Paulo Roberto de Souza Mendes, Professeur, PUC-Rio, Brésil
Directeur de thèse	M. Michel Stanislas, Professeur, École Centrale de Lille
Directeur de thèse	M. Luis Fernando Alzuguir Azevedo, Professeur, PUC-Rio, Brésil

Thèse préparée au Laboratoire de Mécanique de Lille et au Laboratoire de Mécanique de Fluides (PUC-Rio, Brésil)

École Doctorale SPI 072 (Lille I, Lille III, Artois, ULCO, UVHC, EC Lille)
PRES Université Lille Nord-de-France

École centrale de lille

PhD THESIS

submitted to obtain the joint degree of

Docteur de l'École Centrale de Lille
Doutor em Ciências da PUC-Rio

in

Mechanical Engineering

Juliana Kuhlmann Abrantes

Holographic Particle Image Velocimetry for Wall Turbulence Measurements

Oral defence on the 30th of March 2012

Examination Board

President	Paulo Roberto de Souza Mendes, Professor, PUC-Rio, Brazil
Reviewer	Joseph Katz, Professor, Johns Hopkins University, Baltimore, USA
Reviewer	Átila Pantaleão Silva Freire, Professor, COPPE/UFRJ, Brazil
Examiner	Francisco Ricardo da Cunha, Professor, UnB, Brazil
Examiner	Paulo Roberto de Souza Mendes, Professor, PUC-Rio, Brazil
Supervisor	Michel Stanislas, Professor, École Centrale de Lille
Supervisor	Luis Fernando Alzuguir Azevedo, Professor, PUC-Rio, Brazil

Acknowledgments

To my advisors, Professors Michel Stanislas and Luis Fernando Azevedo, for their continuous guidance and support throughout the periods spent in both France and Brazil.

To PUC-Rio, for the financial support, without which this work would not have been realized.

To all my family, who is constantly there for me.

To Thiago, who is always by my side.

To my colleagues at PUC-Rio, and to the friends I made at École Centrale de Lille, who are very dear to me.

To the people at the Mechanical Engineering Department for the constant help, particularly to Grace, Marcia and Rosely.

To professors and researchers at the Laboratoire de Mécanique de Lille, particularly Sebastien Coudert, Jean Marc Foucaut and Matthieu Marquillie, who provided valuable contributions to the work of this thesis.

To the staff at École Centrale de Lille, who was so helpful during the whole process.

Abstract

Constinuously improving the understanding of wall turbulence dynamics has been the goal of many experimental and numerical studies for decades. The main practical aspect that makes this knowledge so crucial is the fact that the wall shear stress is closely related to the dynamics of the near-wall structures. Experimental techniques in fluid mechanics have also experienced a great amount of advances in recent years. The present work details the development of an experimental configuration aimed at providing 3D-3C flow measurements in the very near-wall region of a large wind tunnel facility, which can lead to the assessment of the wall shear stress with improved accuracy. With that goal, a technique known as *Holographic Particle Image Velocimetry* is used, and measurements are made in small volumes close to the wall in the wind tunnel at the *Laboratoire de Mécanique de Lille*. Full measurements in volumes as small as 1.5 mm^3 are made possible with the use of a microscope objective for magnification of the object field. Particles are illuminated from the side and the 90^o scattered field recombines with reference wave for holographic in-line recording. A calibration procedure is performed in order to relate reconstruction space coordinates to real measurement volume coordinates. Analysis of resulting particle fields shows that particle images reconstruct with very good axial accuracy, leading to believe that the configuration is indeed suited for this type of measurement. However, in this first attempt to use this configuration, despite careful alignments and adjustments, the inherent sensitivity of the coherent holographic process with respect to different factors prevented particles from being detected with enough equivalence in *PIV* frames 1 and 2, and not all particle pairs could be retrieved successfully. Thus, some optimizations and adjustments which might be needed in order to improve the particle tracking results are discussed. Nevertheless, results are promising and discussions about them provide interesting insight to some important issues.

Extended abstract in french (Résumé en Français)

Ce travail de thèse porte sur le développement d'une configuration spécifique de Vélocimétrie par Image de Particules Holographique (en anglais, "*Holographic Particle Image Velocimetry*", *HPIV*), adapté pour effectuer des mesures tridimensionnelles de vitesse dans un petit volume à proximité de la paroi d'une grande soufflerie. L'objectif initial est d'acquérir assez de vecteurs à l'intérieur du volume pour être capable de tracer un profil de vitesse axiale moyenne dans la région immédiatement voisine de la paroi, ce qui peut à son tour fournir une mesure directe et précise de la contrainte de cisaillement. En outre, selon les conditions, cette technique peut être poussée jusqu'à fournir des champs de vitesse instantanés en haute résolution spatiale, permettant d'améliorer la compréhension de la dynamique des structures turbulentes proche de paroi et leur relation avec la contrainte de cisaillement.

Chapitre I: Introduction

Les écoulements turbulents pariétaux sont parmi les plus importants en termes d'applications d'ingénierie. En particulier, c'est très proche de la paroi que la plupart de la production de turbulence a lieu. Dans une couche limite turbulente, l'énergie de l'écoulement libre est convertie en fluctuations et puis dissipée par l'action visqueuse sur la paroi dans un processus continu. La contrainte pariétale de cisaillement est donc étroitement liée à la dynamique des structures turbulentes proches de la paroi, et cette relation rend la connaissance de ce domaine si cruciale en pratique.

Ainsi, l'objectif du travail de développement de la technique présentée dans cette thèse est d'essayer de fournir des mesures tridimensionnelles dans la région pariétale des écoulements turbulents. Il est donc important de présenter les principales définitions de la théorie de couche limite. La section I.1 comprend une brève description des types de structure rencontrés dans la région proche de la paroi, ainsi que les principales équations et paramètres de la couche limite, parmi lesquels la contrainte de cisaillement et le coefficient de frottement. Les techniques de mesure pour les écoulements de fluides sont brièvement décrites dans la section I.2. Les techniques de mesure de vitesse sont abordées, avec une attention particulière pour la technique *PIV*. La configuration *PIV* classique permet d'accéder à la distribution instantanée de vitesse dans un plan d'illumination à l'intérieur de l'écoulement d'intérêt. Elle est ainsi classifiée comme 2D-2C (D représente le nombre de dimensions dans l'espace et C le nombre de composantes mesurées). Pour la *PIV* stéréoscopique, deux caméras sont utilisées pour visionner les particules illuminées dans l'écoulement sous différents angles et, en conséquence, la composante hors-plan peut être évaluée, ce qui caractérise une technique 2D-3C. L'étape suivante est alors de couvrir l'espace 3D, c'est-à-dire, d'utiliser une technique 3D-3C, dans le but d'obtenir un aperçu plus complet de certains phénomènes de l'écoulement. Une façon d'y parvenir est par le biais de la *PIV* tomographique, où plusieurs cameras sont utilisées afin de retrouver les positions des particules

dans le volume illuminé de l'écoulement. Une autre alternative est la *PIV* holographique, qui est la technique explorée dans le travail présenté ici.

Ensuite, les techniques directes et indirectes les plus utilisées pour mesurer la contrainte de cisaillement pariétale sont mentionnées. L'attention est portée sur le fait que, en moyenne, il est assez difficile d'obtenir une incertitude inférieure à 1 – 2%. Parmi toutes les méthodes mentionnées, celles qui évaluent la friction à travers des mesures du profil de vitesse près de la paroi sont mises en évidence. En particulier, la méthode du profil sous-couche visqueuse est une méthode directe basée sur la quantification du gradient moyen de la vitesse axiale dans le voisinage immédiat de la paroi (voir l'équation I.1.5 et la figure I.1). Cela implique une mesure précise de la partie linéaire du profil de vitesse axiale, $U^+ = y^+$, ce qui est proposé dans ce travail, sur la base de la technique *PIV* holographique. Enfin, à la fin du chapitre, un aperçu global du travail de thèse est donné. Les objectifs sont une fois de plus énoncés et les étapes principales sont décrites.

Chapitre II: Holographie

Le contexte théorique de l'holographie est présenté dans ce chapitre, en commençant par une brève explication des principaux concepts physiques mis en jeu, tels que les ondes électromagnétiques, leur cohérence, interférence et la diffraction. La nature ondulatoire de la lumière explique certains phénomènes optiques importants tels que l'interférence et la diffraction, qui ne peuvent pas être compris par la seule approche géométrique. Dans la plupart des cas, seul le champ électrique est représenté, et les ondes, caractérisées par leur amplitude et leur phase, peuvent être écrits sous forme d'une exponentielle. Le principe de superposition des ondes lumineuses est discuté, ainsi que la notion de cohérence. Avec la superposition d'ondes et l'interférence convenablement décrites, le principe de Huygens — qui montre pourquoi et comment le phénomène de diffraction a lieu — peut être introduit. La compréhension de ces phénomènes est fondamentale pour travailler avec l'holographie.

Après une discussion sur certains aspects du phénomène de diffraction dans ses deux formes principales, à savoir les diffractions de *Fresnel* et de *Fraunhofer*, le procédé holographique lui-même est décrit à la section II.2, en ses deux étapes: l'enregistrement et la reconstruction d'hologrammes. La tâche fondamentale de l'holographie consiste à enregistrer, et puis reconstruire, l'amplitude et la phase d'une onde optique qui provient d'un objet éclairé de manière cohérente. Dans un premier moment, l'holographie "conventionnelle"est considérée; c'est le cas dans lequel une plaque holographique est utilisée comme moyen d'enregistrement. Dans l'étape d'enregistrement, les informations de phase de l'onde doivent être en quelque sorte transformées en variations d'intensité qui peuvent ainsi être enregistrées par la plaque, et la façon d'y parvenir est par le biais d'interférence. Ainsi, une onde secondaire — l'onde de référence, qui est cohérente avec celle provenant de l'objet et qui a son amplitude et sa phase connues — se superpose à l'onde inconnue de l'objet, et ils interfèrent. L'hologramme est ainsi l'enregistrement de la figure d'interférence entre les ondes d'objet et de référence. Plus tard, lors de l'étape de reconstruction, l'hologramme est éclairé par une onde de reconstruction, et le front d'onde transmis est composé de quatre termes, l'un d'eux étant propor-

tionnel à l'onde d'objet et l'autre au conjugué de celle-ci (correspondant aux images virtuelle et réelle). De cette façon, en regardant à travers l'hologramme, on peut voir une image en trois dimensions de l'objet. Les détails de ces processus sont fournis et, dans un premier temps, les processus sont expliqués dans le contexte de l'holographie hors axe, configuration dans laquelle il y a un angle entre les faisceaux d'objet et de référence. Dans la section suivante, l'holographie en ligne est décrite. Dans ce cas la configuration est le long de l'axe optique, de sorte que les images réelle et virtuelle sont toutes deux centrées sur l'axe de l'hologramme. Ainsi lorsque l'image réelle se rapproche de la mise au point, elle est toujours accompagnée d'une image virtuelle floue et vice-versa. La section II.4 présente la version numérique du procédé holographique.

Chapitre III: Configuration Holographique en Ligne pour les Premiers Tests

Ce chapitre décrit un montage de Gabor en ligne pour les tests préliminaires. Celui-ci est représenté par la figure III.1, et a pour but non seulement de fournir des hologrammes de test pour les développements logiciels initiaux, mais aussi pour se familiariser avec le procédé holographique. Le faisceau traverse un filtre spatial et est maintenu divergent après. Des hologrammes d'une réglette et d'un groupe de particules issues d'un jet d'eau ont été pris et ensuite reconstruits. Un critère de détection de bord basé sur le gradient spatial de la distribution d'intensité est présenté, et peut être utilisé comme un moyen d'évaluer la position de remise au point des particules. Des hologrammes et des champs reconstruits par cette expérience se prêtent bien à l'illustration de certains concepts introduits dans le chapitre précédent. La figure III.6, par exemple, montre l'iso-contour d'une seule particule à 75% de l'intensité maximale, et l'allongement en profondeur est notable, reflétant les limitations de résolution axiale. Le résultat est une image qui semble être à peu près mise au point le long d'une grande profondeur. Ce problème peut être plus grave dans les montages avec diffusion frontale (en anglais, "*forward scattering*"), en raison du lobe central étroit dans le modèle de diffusion de Mie.

Chapitre IV: Configuration spécifique pour les mesures en soufflerie

La configuration *PIV* holographique pour la soufflerie est présentée en détail dans ce chapitre. Tout d'abord, dans la section IV.1, la soufflerie du Laboratoire de Mécanique de Lille (LML) est décrite. C'est une soufflerie de 1m $\times$ 2m de section transversale, où une couche limite d'épaisseur importante peut être obtenue, ce qui permet une très bonne résolution spatiale pour des mesures de vitesse. Pendant la période où les expériences ont été menées, un modéle en forme de bosse était monté pour l'étude de gradients de pression adverses et de séparation, et la position du volume de mesure holographique est indiquée sur la figure IV.2.

La section IV.2 décrit la configuration spécifique, en dispersion latérale ("*side-scattering*"), pour les mesures en soufflerie. Le faisceau sortant du laser est séparé par un diviseur de faisceau, de sorte que les deux faisceaux séparés

puissent être utilisés pour l'éclairage de l'objet et pour la référence avec ratio de 99/1, respectivement. Des particules du petit volume de mesure près de la paroi de la soufflerie sont éclairées sur le côté et dispersent la lumière à 90^o. Cette lumière dispersée par l'objet — l'onde de l'objet — passe ensuite par un objectif de microscope qui l'agrandi. L'onde de l'objet ainsi magnifiée est finalement recombinée avec le faisceau de référence pour interférer, et le front d'onde d'interférence est enregistré au capteur CCD. Les détails sont décrits dans le dessin schématique de la figure IV.4.

La section IV.3 détaille le processus d'étalonnage pour les essais en tunnel. Dans le régime optique choisi, spécialement parce qu'une lentille de fort angrandissement est utilisée, la précision de l'étalonnage est d'une importance capitale. Des équations extraites à l'aide de ce procédé permettent d'associer à la localisation des images de particules, détectées dans le volume reconstruit, leurs positions d'origine dans le volume de mesure situé dans la soufflerie. Pour cette configuration particulière, le processus d'étalonnage a posé un véritable défi. Des objets et des systèmes d'éclairage différents ont été testés dans une tentative d'enregistrer des hologrammes de bonne qualité qui pourraient être reconstruits sans problèmes. Mais dans tous les cas testés, des effets divers ont empêché l'interférence d'avoir lieu. La décision finale a été d'utiliser un trou de 15 μm comme objet d'étalonnage. La figure IV.14 montre la configuration de ce montage. Des hologrammes du trou positionné à plusieurs distances de la paroi ont été enregistrés. La figure IV.15 montre un exemple de reconstruction (une série de quatre images en profondeur, dans la direction de la mise au point) du trou dans une position donnée dans la soufflerie. Les équations d'imagerie pour l'ensemble du système impliquent à la fois les équations holographiques et l'équation de la lentille. Les hologrammes du trou sont utilisés pour déterminer les positions des lentilles internes de l'objectif, les paramètres d_i et d_o figurant dans les équations finales (IV.3.18 à IV.3.20). Ces équations sont donc celles qui vont récupérer les coordonnées 3D réelles de la soufflerie à partir des coordonnées de particules dans l'espace de reconstruction. Le tableau IV.1 indique le changement de nomenclature de coordonnées optiques à coordonnées de volume réel. La figure IV.20 présente la forme trapézoïdale du volume final en coordonnées réelles.

Chapitre V: Résultats pour la Soufflerie: Hologrammes de Particules, Champs de Particules Reconstruits, et Algorithme de *Tracking* des Particules

Les hologrammes des particules prises dans les conditions d'écoulement en soufflerie sont finalement présentés dans ce chapitre, avec des exemples de plans reconstruits, comme sur la figure V.2(a), dans laquelle un plan de reconstruction d'une profondeur donnée est présenté. La figure V.2(b) montre l'évolution en profondeur d'une seule particule, en zoom, entrant et sortant de la mise au point. La structure de données mise en œuvre dans le logiciel pour le stockage du volume reconstruit est décrite. Les données concernant l'intensité, mais aussi le gradient spatial d'intensité et les parties réelles et imaginaires du champ reconstruit sont stockées, plan par plan.

Ensuite, les procédures de traitement d'image et algorithmes pour la détection, validation et localisation des particules sont présentées dans la

section V.3. À partir des données brutes d'intensité dans le volume reconstruit, une analyse d'histogramme est réalisée pour la détection de points lumineux. Les coordonnées de leurs positions centrales sont stockées et traitées comme les positions des "candidats-particules". Ensuite, un critère de validation est appliqué, afin de vérifier si chaque candidat est en effet une particule ou un bruit lumineux. Autour de chaque candidat-particule, une structure "tubulaire", semblable à la structure pour les volumes, est crée pour une analyse plus détaillée. Un "tube" est constitué d'une série de plans découpés, étroitement espacés en profondeur, autour de la position centrale du candidat. Pour chaque tube, un critère de validation est appliqué à travers de l'évaluation de la pente de décroissance a partir du pic de l'histogramme de l'image volumétrique du tube, qui est en relation avec le contraste entre les pixels les plus clairs et le fond à l'intérieur du tube (les histogrammes sont présentés pour trois particules différentes dans figures V.6 à V.8. La particule C, de la figure V.8, est rejetée sur la base de ce critère). Comme cela, certains candidats sont éliminés, et seuls les candidats validés comme particules sont stockés. Les figures V.9 et V.10 montrent des exemples de structures tubulaires crées autour de deux particules valides, colorées selon la distribution de l'intensité.

Une fois que seules les particules valides restent, des critères différents sont évalués sur chaque plan, pour tous les tubes de particules. Des critères basés sur les données d'intensité et de gradient (comme l'intensité maximale et la variance maximale, par exemple) sont placés sur un graphe comme fonction de la profondeur du tube, puis multipliés afin d'offrir une caractéristique de pic plus facile à discerner, et offrir ainsi un critère final pour l'estimation de la position en profondeur des particules (détection de mise au point). Les figures V.13 et V.14 montrent les graphes de ces critères pour les particules A et B. Enfin, des tests de double exposition et l'implémentation de l'algorithme de *tracking* de particules sont commentés, ainsi que quelques résultats.

Chapitre VI: Considérations Finales

Dans ce dernier chapitre, une discussion des résultats, de la réalisation et des perspectives est présentée. Comme les tests de double exposition (avec des données provenant d'un lot avec Δt très bas, les particules des cadres *PIV* 1 et 2 ont été superposées sur la même image) ont montré que certaines paires sont récupérées mais plusieurs particules restent non appariées, les sources possibles du problème et les optimisations futures envisagées pour le montage optique sont analysées. Considérant que les lots acquis sont le résultat de la première tentative expérimentale d'employer un montage optique qui a exigé un certain nombre d'ajustements non triviaux, des résultats peuvent être appréciés comme très positifs. Le manuscrit couvre les différentes étapes du travail de thèse, de l'enregistrement à la reconstruction et extraction de coordonnées de particules. Les images de particules dans les "tubes" et les graphiques d'évolution en profondeur présentés dans le chapitre V montrent que, en effet, une bonne précision axiale est obtenue pour la détection des particules, qui se traduit par une incertitude faible en coordonnées réelles du volume de mesure.

Contents

List of Figures

List of Tables

I
Introduction

In this first chapter, a review of some of the important concepts and definitions concerning wall turbulence and boundary layer flows is presented. The ultimate motivation for the development of velocity-measuring techniques such as the one proposed here is to be able to provide better understanding of the flow of interest. Here, in particular, the development of a specific *holographic PIV* configuration — which constitutes the core work of this thesis — is aimed at making measurements with improved accuracy in the very-near wall region of a turbulent boundary layer flow in a wind tunnel. As this is the main goal, a description of the theoretical background is in order.

However, the main focus of the thesis is the development of the technique itself, and the required theoretical background on optics and holography is properly described in Chapter II. Later on, all the steps comprising the implementation of the specific setup employed in the wind tunnel experiments are described, followed by a presentation of the results, and it will be seen that some difficulties related to the complexity of the optical setup were encountered. Some issues and optimizations to be made in the setup are then discussed.

I.1 Wall Flows

Wall-bounded flows, specially turbulent flows, are among the most important in terms of engineering applications. In these flows, the wall friction is a particularly important parameter that imposes constraints to many situations. For example, skin-friction drag constitutes a large fraction of the total drag on aircrafts and any reduction in drag results in substantial energy savings. However, any optimization or successful control requires a thorough understanding of the physics involved in the flow phenomena. Thus, the velocity field in the near-wall region is of considerable interest and is the focus of many investigations. This is the region where most of the production of turbulence takes place and, right at the wall, the shear stress manifests itself through the mean velocity gradient.

In a turbulent boundary layer, energy from the free-stream flow is converted into fluctuations and then dissipated by viscous action in a continuous process, and the relationship between the near wall structures and the wall shear stress is a very interesting and recurrent theme of research, concerning both practical developments and fundamental studies.

Recognition of the existence of well-organized turbulent structures and the importance of their role in the wall-layer dynamics are among the major advances in turbulent boundary layer research in past decades. The extensive numerical and experimental studies up to now have identified that there are characteristic turbulent structures or quasi-coherent structures in wall-bounded flows. The usual structures in this region are low and high speed streaks ([Kline *et al*, 1967], [Robinson,1991]), which consist mostly of spanwise modulations of the streamwise velocity. These streaks are created by streamwise vortices, which are roughly aligned in the streamwise direction. Because of their ability to transport momentum across the mean velocity gradient, such vortical structures are a very important feature of near-wall turbulence.

It has also been recognized, in large part due to numerical investigations, that streamwise vortices are related to the high skin friction drag observed in turbulent flows ([Kravchenko *et al*, 1993]). The work of [Hanratty and Brooke, 1993] suggested that streamwise vortices regenerate themselves through a process that is weakly dependent on the outer flow. However, despite continuously being the focus of many investigations, some aspects of the mechanisms involved remain unclear.

Numerical simulations are still somewhat restricted in terms of the Reynolds numbers they can achieve. Thus, the ability to perform spatially-resolved experimental measurements in the near-wall region is fundamental to the progress in the research of turbulent wall flows. Particularly, for the detailed study of the relation between near-wall turbulent structures and the skin friction distribution, simultaneous measurement of both with sufficient spatial resolution is required.

The very near-wall region is, however, difficult to study experimentally, partly because of strong demands on spatial resolution, but also because the presence of the wall itself can, depending on the technique, influence the performance of the measurements.

Although complete, spatially and temporally-resolved measurements are highly desirable for continually improving the knowledge on the dynamics of near-wall structures and their relation with the local wall shear stress, for many practical flow applications one simply has to assess the mean profiles and the

mean wall shear stress.

Next, a brief description of the important physical quantities and scales in turbulent boundary layers is presented (for a detailed study, see [Schlichting, 1979]).

Boundary Layer Flows In the simplest case of a flat-plate, statistically two-dimensional boundary layer flow in the (x,y) plane, where x is the streamwise and y the wall-normal direction, the flow is generated by a constant free stream velocity, U_∞, flowing over the smooth plate located in the $y = 0$ plane of semi-infinite extent ($x \geq 0$). The boundary layer thickness $\delta(x)$ develops continuously in the flow direction (the mean flow is predominantly in the x direction), and is taken to be the y position where $U(y) = 0.99U_\infty$ — increasing with x. Statistics vary primarily with the y direction, being independent of z, and of course, depend on the x direction.

The free-stream pressure is related to the free-stream velocity U_∞ through Euler's equation so that

$$-\frac{\mathrm{d}p_\infty}{\mathrm{d}x} = \rho U_\infty \frac{\mathrm{d}U_\infty}{\mathrm{d}x}, \tag{I.1.1}$$

where ρ is the fluid density. Accelerating flow $\frac{\mathrm{d}U_\infty}{\mathrm{d}x}>0$ corresponds to a *favorable* pressure gradient, and $\frac{\mathrm{d}U_\infty}{\mathrm{d}x}<0$ to an *adverse* pressure gradient, which can eventually lead the flow to separation. In the simpler zero-pressure-gradient case, $U_\infty(x)$ is constant.

Apart from the boundary layer thickness $\delta(x)$ definition, other integral measures characterizing the boundary layer at the different streamwise positions are the *displacement thickness*

$$\delta^*(x) \equiv \int_0^\delta \left(1 - \frac{\bar{U}}{U_\infty}\right) \mathrm{d}y, \tag{I.1.2}$$

and the *momentum thickness*

$$\theta(x) \equiv \int_0^\delta \frac{\bar{U}}{U_\infty}\left(1 - \frac{\bar{U}}{U_\infty}\right) \mathrm{d}y, \tag{I.1.3}$$

where $\bar{U}$ is the mean streamwise velocity.

The Reynolds number for different streamwise stations can be defined in various ways, using x ($\mathrm{Re}_x = \frac{U_\infty x}{\nu}$), or any of the thicknesses defined above ($\mathrm{Re}_\delta = \frac{U_\infty \delta}{\nu}$, $\mathrm{Re}_{\delta^*} = \frac{U_\infty \delta^*}{\nu}$, $\mathrm{Re}_\theta = \frac{U_\infty \theta}{\nu}$).

With the boundary layer assumptions and the axial stress gradients being small compared to cross-stream gradients, the mean axial momentum equation is written as

$$\begin{aligned} \bar{U}\frac{\partial \bar{U}}{\partial x} + \bar{V}\frac{\partial \bar{U}}{\partial y} &= \nu\frac{\partial^2 \bar{U}}{\partial y^2} - \frac{\partial \overline{uv}}{\partial y} - \frac{1}{\rho}\frac{\mathrm{d}p_\infty}{\mathrm{d}x} \\ &= \frac{1}{\rho}\frac{\partial \tau}{\partial y} + U_\infty \frac{\mathrm{d}U_\infty}{\mathrm{d}x}, \end{aligned} \tag{I.1.4}$$

where ν is the kinematic viscosity of the fluid, u and v are the streamwise and wall-normal velocity fluctuations, $\overline{uv}$ is the Reynolds stress and $\tau(x, y)$ is the total shear stress given by $\tau = \rho\nu\frac{\partial \bar{U}}{\partial y} - \rho\overline{uv}$.

The shear stress at the wall, τ_w, an important quantity characterizing the flow and whose measurement is often desired in research experiments and practical applications, is then

$$\tau_w(x) = \rho\nu \left(\frac{\partial \bar{U}}{\partial y}\right)_{y=0}, \tag{I.1.5}$$

since at the wall all the convective terms are zero. The so-called *skin-friction coefficient* is expressed as

$$C_f \equiv \frac{\tau_w}{\frac{1}{2}\rho U_\infty^2}. \tag{I.1.6}$$

To obtain an expression for the wall shear stress in terms of the displacement and momentum thicknesses instead of the normal gradient of the axial velocity at the wall as in eq.(I.1.5), the momentum equation (I.1.4) can be integrated from zero to infinity, so that the *von Kármán's integral momentum equation* is obtained,

$$\frac{\tau_w}{\rho} = \frac{\mathrm{d}}{\mathrm{d}x}(U_\infty^2\theta) + \delta^* U_\infty \frac{\mathrm{d}U_\infty}{\mathrm{d}x}, \tag{I.1.7}$$

and hence, for the skin-friction coefficient,

$$C_f \equiv \frac{\tau_w}{\frac{1}{2}\rho U_\infty^2} = 2\frac{\mathrm{d}\theta}{\mathrm{d}x} + \frac{(4\theta + 2\delta^*)}{U_\infty}\frac{\mathrm{d}U_\infty}{\mathrm{d}x}. \tag{I.1.8}$$

Equations (I.1.7) and (I.1.8) are general and suited for the cases of negative, zero and positive pressure gradients.

In turbulent boundary layers, the mean velocity profiles usually rise much more steeply from the wall than in the laminar case, and are flatter away from the wall. The *shape factor* $H \equiv \delta^*/\theta$, defined as the ratio between displacement and momentum thicknesses, quantifies the "flatness" of the mean velocity profile.

Clearly, close to the wall, the viscosity ν and the wall shear stress τ_w are important parameters. Thus, *viscous scales* are defined, which are appropriate velocity scales and length scales in the near-wall region. The *friction velocity* is given by

$$u_\tau \equiv \sqrt{\frac{\tau_w}{\rho}}, \tag{I.1.9}$$

and the viscous length scale,

$$\delta_\nu \equiv \nu\sqrt{\frac{\rho}{\tau_w}} = \frac{\nu}{u_\tau}. \tag{I.1.10}$$

The distance from the wall measured in viscous lengths - or *wall units* - is $y^+ \equiv y/\delta_\nu = u_\tau y/\nu$, and the non-dimensional mean axial velocity is defined by $U^+ \equiv \bar{U}/u_\tau$.

Different regions — or layers — in the proximity of the wall are defined with respect to y^+. In the *viscous wall region* $y^+ < 50$, there is a direct effect of molecular viscosity on the shear stress. In the *viscous sublayer*, $y^+ < 5$, inside the viscous wall region, the Reynolds stress is negligible compared to the viscous stress, and a linear relation for the non-dimensional velocity profile holds, $U^+ = y^+$. The region between $y^+ > 30$ and $y/\delta < 0.3$ is denominated the *log-law region*, where the log law, $U^+ = \frac{1}{\kappa}\ln y^+ + B$, generally holds. The von Kármán constant κ and B are empirical constants. The region between the viscous sublayer and the log-law region is referred to as *buffer layer*.

As the Reynolds number of the flow increases, the fraction of the near-wall region occupied by the viscous wall region decreases.

The physical significance of these scaling parameters is not only relevant to theoretical formulations, but is of central importance when considering the rational design of experiments.

I.2 Fluid Flow Measurements

Because of the aforementioned motivations, related to both practical applications and academic research, the spatially-resolved measurement of near-wall velocity and velocity gradients is often crucial and desirable. From one side, knowledge of the flow characteristics and the wall shear stress can make a significant difference in the design of equipments, aircrafts, etc. From the other, increasingly accurate and detailed measurements provide a relevant contribution to the comprehension of the complex mechanisms that control the motion of the large and small-scale structures in turbulent flows.

In this section, a brief description of some techniques for velocity and

wall shear stress measurement is presented. This description is intended to contextualize the contribution that the *Holographic PIV* technique, in all its configurations, can provide.

I.2.1 Velocity Measurements

Problems in fluid dynamics are often quite challenging and concern complex, non-stationary, three-dimensional flows. Thus, there is a constant need for the development of tools and techniques, both numerical and experimental, that can fulfill these demands. At the very near wall region, experimental measurements are very difficult because of strong demands on spatial resolution. Strong gradients can also make measurements difficult.

Nevertheless, experimental techniques have gone through a great amount of development in recent years, and with the newest possibilities, experimentalists have the chance to contribute even more deeply, providing further insight into the physics of turbulence. The availability of fast, high energy pulsed laser sources and digital cameras with increasing spatial and temporal resolution has been enabling the use of tools that steadily go towards 3D time-resolved measurements of complex flows.

One of the challenges in the case of turbulent wall-bounded flows is that often the goal is to perform time-resolved measurements in the very near-wall region — in order to study the small-scale structures, their generation mechanisms and their relation to the wall shear stress — and this is not easily attained for most techniques.

Here, however, the focus will be on presenting a brief overview regarding *PIV*-based techniques. Other usual and extremely relevant techniques such as thermal anemometry and Laser Doppler Anemometry will not be described, but are important tools in flow characterization.

Particle Image Velocimetry, or *PIV*, has spread widely into many distinct applications, from micro flows to supersonic flows, combustion and others, for both industrial and research needs (see [Schroeder and Willert, 2008] and [Adrian and Westerweel, 2011] for a thorough description of historical development, theory, and state-of-the-art applications). It is a non-intrusive optical measurement technique which allows capturing several thousand velocity vectors within flow fields instantaneously. Tracer particles that are assumed to faithfully follow the dynamics are added to the flow, and instantaneous images are captured of the light scattered by the particles as they are illuminated with a sheet of laser light. Pairs of images taken with a known time spacing between

them are then analyzed with the aid of correlation tools in order to calculate the velocity field through the measurement of the displacements of groups of particles between the two exposures.

In this way, for the most basic *PIV* configuration that can be employed, the two-component (2C) velocity field in a 2D plane of the flow can be evaluated, and thus this form of the technique is classified as "2D-2C". The step that followed the use of this "classical" form of *PIV* was the stereoscopic version, based on the same fundamental principle as human eye-sight. A light sheet is used to illuminate the plane of interest in the flow and two cameras are used to image the illuminated flow particles from different angles. The combination of both camera projections and a correct calibration procedure allows reconstruction of the particle displacements with evaluation of all three velocity components within the illuminated plane, thus characterizing a 2D-3C technique, which is currently well consolidated and extensively used in fluid dynamics research ([Prasad, 2000], [Schroeder and Willert, 2008]).

With *Stereoscopic PIV* becoming standard to obtain three-component (3C) velocity data, what is left is to cover the 3D space in an attempt to achieve more complete insight into some flow phenomena. One technique that is currently being explored is called *Tomographic PIV* ([Elsinga *et al*, 2006], [Elsinga *et al*, 2007], [Atkinson *et al*, 2008]), in which multiple instantaneous views of a seeded flow field are used to estimate the three-dimensional distribution of particles in the flow. Three-dimensional cross-correlation is then used to determine the displacements and the corresponding 3D-3C velocity vectors. This technique has limitations concerning the requirement of instantaneous synchronized images and the limited number of cameras and optical access points that are generally found in most fluid measurement facilities.

Making use of holography is another way of achieving 3D-3C measurements. The advances in electronics have led to the availability of cameras with high spatial resolution, which in turn made their use for recording digital holograms possible ([Schnars and Juptner, 1994], [Meng *et al*, 2004]). In this way, following the *PIV* principle of imaging the flow at two instants separated from each other, pairs of holograms are recorded with a known time interval between them. Once the holograms are reconstructed into volumes (3D fields of particles), one can establish the displacement between exposures of the particles within the volume — either using cross-correlation, particle tracking algorithms, or a combination of both — and consequently calculate the 3D-3C velocity field (e.g., [Sheng *et al*, 2008] and [Amili and Soria, 2009]). This technique is referred to as *Digital Holographic PIV* (*DHPIV*), and details of all steps involved in the process will be explained in subsequent chapters of this

thesis, since this is the technique explored here.

All these *PIV*-related techniques aim in some way at observing the instantaneous flow structures and at clarifying the dynamics of the underlying flow. Several types of statistical quantities — the most basic being the mean velocity field — can be calculated from sequences of instantaneous fields.

With the use of *Holographic PIV*, one can aim not only at obtaining experimental mean 3D velocity fields and computing quantities such as the mean shear stress at the wall, but also at looking into instantaneous volumetric information that can clarify the three-dimensional turbulent interactions and their enhacing effect on the skin-friction. For some specific holographic configurations and flow conditions, though, the latter task may be more challenging than for others.

I.2.2 Wall Shear Stress Measurements

As mentioned before, in most fluid mechanics applications, a knowledge of the shear stress over a solid surface is essential for the performance of the system, as well as for conceptual understanding of the flow.

The primary mechanism of the turbulent boundary layer, when viewed as a whole, relates to its capacity to convert free-stream momentum into a shear force acting over the surface. Indeed, when viewed in this way the skin friction coefficient from equation (I.1.6) is a measure of this capacity, as it constitutes the ratio of the mean wall shear stress to the axial free-stream momentum flux per unit area. From the perspective of engineering applications, the accurate prediction of C_f is, of course, required for the design of systems, aircrafts, and so on.

Similarly, the wall shear stress is an essential parameter in theoretical descriptions of boundary layers, with $\overline{\tau_w}$ (often through u_τ) constituting a primary scaling parameter relative to theoretical treatments of wall turbulence. It is valuable to be able to measure its distribution with the highest possible accuracy, since this leads to a better knowledge and representation of the near wall flow.

Lastly, the instantaneous, fluctuating surface stress has relevance to improved methods of flow management and control, with purposes like drag reduction or separation delay, as well as input to numerical methods such as large eddy simulation.

When it comes to measuring the wall shear stress (see [Tropea *et al*, 2007]), depending on the application and objectives, there

are several techniques that have been explored and implemented. However, all of these techniques suffer to different degrees from limitations. Reviews are available (for example, [Naughton and Sheplak, 2002]) that describe most of them. Here, the main distinct categories and methods of measuring wall shear stress are briefly presented. For most of them, different challenges make it difficult, or even impossible, to have an accuracy better than ± 1 or 2 %.

Time-averaged wall shear stress

Methods involving measurements at the surface

Oil Film Interferometry. This is a method for the direct measurement of skin friction, meaning it directly measures the force applied to the wall by the fluid and does not depend on flow field assumptions or equations modeling flow conditions. It consists of measuring the thinning rate of an oil film as it is being acted upon by the wall shear, allowing reasonably accurate measurements of the mean skin friction without specific and expensive equipment. A simple camera and a monochromatic light source are the only devices needed. Optical access to the facility test section and a proper calibration of the oil viscosity against temperature are also necessary.

The variation of the oil-film thickness being acted upon is measured with an interferometric technique. The monochromatic light is reflected from both the oil surface and the underlying wall, producing an interference fringe pattern that is recorded on a CCD camera for proper analysis. The pattern is related to the wall shear stress through the variation of the oil-film thickness.

Some of the error sources and difficulties associated with this method include dust, humidity, high-shear situations, oil property variations, oil evaporation, shear stress variation, surface tension, pressure gradients, gravity effects and flow modification by the oil film.

The utilization of this technique was demonstrated in a number of studies. In the work of [Ruedi *et al*, 2003], it was used in a turbulent boundary layer wind tunnel flow, to measure the skin friction magnitude and also its direction in two or three-dimensional flows. The method was employed by [Ng *et al*, 2007] in a high Reynolds number turbulent boundary layer facility and in fully-developed turbulent channel flow, with the results of the latter being validated against skin friction results known from the pressure gradient along the channel. Average wall shear stress obtained from the oil film

technique was found to agree with values obtained from the pressure gradient to within ±2.5% for a range of Reynolds numbers.

Although the basic form of the technique is for time-invariant wall shear stress, methods have been developed for cases where the shear stress is time-dependent ([Naughton and Sheplak, 2002]).

Oil Droplet Interferometry. An alternative approach to the oil film for measuring skin friction in high gradient wall regions consists in applying small oil droplets ([Barricau *et al*, 2009]), in order to have small area elements over which the wall shear stress can be considered as constant, providing interferometric patterns with a constant inter-fringe. The surface must be perfectly flattened in order to prevent disturbances in the interferometric patterns.

The equation for the wall shear stress governing this method shows that the accuracy of the measurement depends upon potential uncertainties in the evaluation of the oil viscosity, calibration coefficient, evaluation of fringe spacing and optical characteristics of the oil. The uncertainty estimated by [Barricau *et al*, 2009] was of ±3%, which was confirmed by repeated measurements. Experimental test cases included zero and adverse pressure gradient wind tunnel boundary layers. In the zero pressure gradient case, results showed fair agreement with other techniques, and very low levels could be measured. In the adverse pressure gradient case (achieved with a bump in the tunnel), there was low deviation between various repeated measurements at the end of the sloping region of the bump, where the magnitude of the shear stress is close to zero.

Elastic Film Shear Stress sensor. This is another direct measurement method, similar to the oil film, but consisting of mounting a thin film made of a linear elastic material on the surface. The geometry and mechanical properties of the material are known, and particles acting as markers are applied to the top surface of the film. An optical technique is then used to measure the film deformation caused by the flow. The shear stress distribution over the film is determined by implementing a shear strain - shear stress relationship in a way that the local thickness is a function of the applied force, the film initial thickness, and the film shear modulus. This was employed by [Amili and Soria, 2009] in an open-circuit wind tunnel, where a film was flush-mounted to the wall. Static calibration was performed and average wall shear stress was examined, based on the film deformation, by a planar multi-grid cross correlation *PIV* algorithm of flow-off and flow-on images. Temporal and

spatial-averaging of the stress over the entire field of view were performed for mean results, which had an overall estimated uncertainty of 3.5%.

Other simple methods such as the mean pressure gradient method and the Preston tube present restrictions in terms of the flow conditions in which they can be employed, and thus have very low applicability in more complex flows.

The mean pressure gradient method is a simple, yet highly accurate, method for measuring the average wall shear stress in fully developed internal flows. In this case, the mean wall shear stress can be calculated from the measured axial pressure gradient. Unfortunately, the applicability of this method is obviously quite limited in practice. Even in channel flows of high aspect ratio, the apparent effect of the side walls can be felt in the core flow.

The Preston tube method uses stagnation pressure information derived from a tube placed on the wall. It relies on the correlation between τ_w and the difference between the surface static pressure and the stagnation pressure produced by the portion of the mean velocity profile in the region of the flow where the so-called law of the wall is valid. Hence, it is restricted to the assumption that a logarithmic law-of-the-wall region exists and that the tube opening is inside or below this portion of the profile, being thus innapropriate for nonequilibrium wall flows or other situations where the logarithmic portion of the mean profile has been altered.

Mean-Profile-Based Methods

There are different methods for determining the time-averaged shear stress from mean velocity profile data. Basically, the choice depends on the velocity measurement technique employed, that is, on the region of the near-wall flow it can measure and the spatial resolution it can achieve.

The Von Kármán Momentum Integral method. This method relies on the computation of the displacement and momentum thicknesses, and thus requires measurements of the mean velocity profile.

For two-dimensional developing flows, the surface stress is related to the momentum and displacement thicknesses by Von Kármán's momentum integral equation (I.1.7). The equation includes the effects of axial pressure gradient, and thus for flat-plate boundary layer flow the last term is zero.

When using techniques that are able to provide good measurements of the normal Reynolds stresses and the Reynolds shear stress, the complete

axial momentum equation can be integrated in y and applied. The key point is that the left-hand side of the equation depends only on x, and, thus, so must the sum of all terms on the right-hand side. In [Johansson, 2009], for example, the author performed *LDA* measurements trying to reach as much as possible the very near-wall region, and proposed explanations for the detected malfunctioning of the system when measuring very close to the wall. Then the momentum integral method was used with the equation including all the terms. The work studied in more detail the contributions of the various terms (viscous shear stress, Reynolds shear stress, momentum integrals, pressure gradient) and argued that the degree to which the sum of all terms is constant is a measure of the accuracy of the velocity-measuring method. It was noticed that very close to the wall the sum deviates considerably from the value attained further out, due to measurement difficulties in this region. It was also observed that the momentum intregral method has the advantage that it can be used also for high Reynolds numbers, and for rough surfaces, where the wall shear stress is not easily measured with other methods. On the other hand, it is very sensitive even to small secondary flows, and it has been found that the pressure gradient can in practice never be neglected, but these features are not necessarily drawbacks. The method can be used to detect if a secondary flow is present, and to investigate to what extent a small variation in the free stream speed affects the force balance in the boundary layer.

Clauser Plot Method. The so-called Clauser plot method is also an indirect technique, and is essentially a graphical method which relies on the observed correlation between the wall shear stress and the properties of the logarithmic mean velocity profile characteristic of wall-bounded flows. Implicit in this technique is the assumption of a universal logarithmic mean velocity profile.

The attractive feature of this method is that velocity measurements in the viscous sublayer portion of the profile, that are often difficult to obtain, are not required. Conversely, however, deviations from the assumed behavior may preclude its use.

The method is capable of producing reasonably accurate results, say $\pm 5\%$, but it is neither a direct nor independent method, and should be viewed as a useful means of approximating the value of the friction velocity, since it relies on the existence and validity of the logarithmic law. It is clearly not appropriate, for example, for flow conditions such as those with strong pressure gradients or separation. Additionally, the accuracy of the method is dependent on the selection of κ and B, the parameters in the logarithmic law equation.

Finally, as with all other mean-profile-based methods, another common source of uncertainty can be associated with the method of measuring the velocity profile itself.

Viscous sublayer profile or Mean wall gradient method. The viscous sublayer profile method can be considered direct in the sense that it is based upon quantifying the mean gradient of the axial velocity in the immediate vicinity of the wall (see figure I.1). According to its definition, the mean shear stress produced at a point on a bounding solid surface by a flowing fluid is given by equation (I.1.5). Thus, for a fluid with known properties, the task is to experimentally determine the slope of the axial velocity profile at the wall.

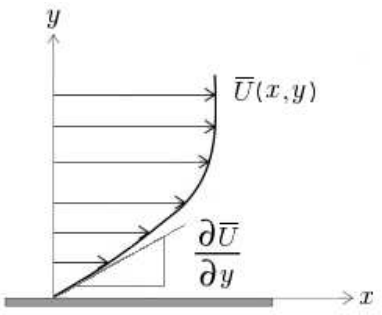

Figure I.1: Mean velocity gradient at the viscous sublayer: accurate velocity measurements in the linear region lead to the direct assessment of the wall shear stress.

This involves accurately measuring the linear portion (say within $y^+ < 5$) of the mean velocity profile in the immediate vicinity of the surface. It is a theoretically exact method in the case of smooth wall flows in which a linear profile region $U^+ = y^+$ is sure to exist (in proximity of a point of separation, for example, such a region can be expected to become diminishingly small or even non-existent and in flows over rough surfaces one can not count on the presence of a linear region), but is, of course, prone to errors in the experimental evaluation of the velocity profile.

Under the vast majority of flow conditions, the physical dimension of the region of linear dependence is small: typically a fraction of a millimeter. Because of this, the sensing dimension of the measurement probe should be very small as well or, more generally, the spatial resolution of the measurement technique should be quite high. In air this is specially difficult to achieve because of the extremely thin viscous sub-layer and the very low flow velocities close to the wall.

The determination of τ_w through this method with the use of well-established measurement techniques such as hot wire anemometry, however,

is — even under ideal conditions — only possible with a measurement uncertainty of approximately 5%. At a certain distance from the wall, hot wire signals, for example, start to become contaminated by wall-interference, and measurements should be taken preferably in a region above where wall effects are significant and below the upper bound of the viscous sublayer.

Laser-Doppler Anemometry would be a non-intrusive option, since the diameter of the probe volume of an *LDA* system can be made quite small, providing a good enough spatial resolution at least in low Reynolds number flows. However, as witnessed in several investigations, the very near-wall region shows problems. In the aforementioned work of [Johansson, 2009], measurements on a smooth flat plate with an *LDA* system with a small probe diameter, that in theory provided sufficient spatial resolution to measure the mean velocity gradient at the wall, led to profiles that deviated from the expected behavior and presented problems that made direct evaluation of the wall shear stress inaccurate. One of the reasons pointed out by the author was that the low speed samples are systematically rejected at a higher rate than high speed samples, and, very close to walls, one always measures a too high mean velocity. The system works best at low particle concentrations, and for very small probe diameters. So, achieving the goal of accurately measuring several points in the linear region is still a challenging task in general.

A digital long-distance microscopic *PIV* system was developed by [Kähler *et al*, 2006] to non-intrusively measure the wall shear stress and the near-wall flow characteristics in laminar, transitional and turbulent boundary layer flow along a flat plate. To achieve high accuracy and spatial resolution, experimental limitations associated with seeding, light-sheet, out-of-focus particles and optical aberrations were dealt with, and a two-point ensemble correlation evaluation approach was developed.

Based on a detailed uncertainty analysis, it was estimated that the total measurement error was around 0.1% for the direct estimation of the wall-shear-stress at 10 m/s free-stream velocity. It was also argued that in the analysis of flows at large Reynolds numbers, where small spatial dimensions and strong flow gradients usually prevent accurate measurements, this technique can be applied as well, and the authors emphasized that this excellent precision could be obtained directly without any assumptions about the flow and without disturbing the experiment as required with intrusive probes.

Time-resolved wall shear stress

In a turbulent flow the time-averaged wall shear stress values are indicative of the global state of the flow along a surface, while the time-resolved part is a measure of the unsteady structures of the flow field, which are responsible for the individual momentum transfer events in the boundary layer.

In comparison to techniques designed to measure the time-averaged shear stress, those capable of producing time-resolved measurements of the instantaneous wall shear stress are considerably fewer in number. Two primary reasons for this are that the correlations constituting the basis of indirect techniques are generally not instantaneously valid, and accurately quantifying instantaneous shear stress values requires sensing systems that have both a high-frequency response and a sufficiently small size.

The time-resolved methods, thus, are associated with either the direct measurement of the shear force acting over a small element of the surface, or are effectively instantaneous versions of the viscous sublayer profile method discussed just above. Of course, general techniques designed to give the spatially and temporaly resolved wall shear stress can certainly also be used to obtain mean values.

Floating-Element Sensors

These sensors directly measure the shear force imparted on a movable, floating element portion of the wall. When subjected to flow conditions, the sensor functions either by measuring the amount of force required to keep the element in place or by correlating the displacement of the element with the applied shear force. A major positive attribute of floating-element sensors is that no assumption about the flow field, fluid properties, or surface needs to be made, and therefore they are not affected by errors associated with using simplifying assumptions or developing correlations.

In practice, however, they are often difficult to use. Some of the difficulties are: the compromise on the size of the element (it needs to be sufficiently large so that the force acting on it has a magnitude that can be measured accurately, and small enough to measure local conditions when desired), effects of gaps around the edges of the element, effects due to misalignment of the element, errors associated with pressure gradients, among others.

For fully-resolved measurements in turbulent wall-bounded flows where the characteristic dimension of the sensor is required to be very small, *MEMS* (microelectromechanical systems) sensors can be used, which can attempt

to satisfy this criterion ([Ruedi *et al*, 2003], [Löfdahl *et al*, 2003]). Those are specially manufactured sensors with very small physical size that can vastly improve both the temporal and spatial measurement bandwidth.

Instantaneous Wall Gradient Methods

Measurements of the instantaneous wall velocity gradient are possible as long as spatially and temporally well-resolved axial velocity measurements can be accurately acquired in the viscous sublayer. MicroPIV and microscopic HoloPIV are possible options for that. The former was already mentioned above, in the context of mean wall gradient methods ([Kähler *et al*, 2006]), and was demonstrated to also be able to measure instantaneous fields.

As for Holographic PIV, it is also a powerful technique that can be used as a means of directly measuring the linear velocity profile and estimate the wall shear stress with very good accuracy, and depending on the conditions, it can be used to study the near-wall flow in much more detail. A very good example of that can be found in the work of [Sheng *et al*, 2008].

In that work, a digital holographic microscopy technique was employed in a fully-developed turbulent flow in a square duct, to simultaneously measure instantaneous 3D flow structure and spatial distribution of the wall shear stress. The authors achieved a spatial resolution of 1 wall unit in the wall normal direction. Uncertainty in velocity was estimated to be less than 0.05% of the bulk velocity. A typical instantaneous volumetric velocity field obtained is shown in figure I.2(a), extracted from the referred article.

Instantaneous wall shear spatial distributions were approximated with the least square fit of velocity measurements in different sub-regions in the viscous sublayer. Then, by superimposing measured axial velocity values from all realizations, the mean streamwise wall shear stress and the wall unit were estimated from linear regression of the scatter plot within the viscous sublayer, as shown in figure I.2(b).

Finally, 3D turbulent structures associated with the wall shear stress, such as streamwise vortices, were also detected and could be related to the instantaneous shear stress distributions.

Digital holographic microscopic PIV measurements were also performed in the work of [Amili and Soria, 2009], in which instantaneous velocity profiles in the $y^+ < 5$ region were measured for a channel flow, leading to the conclusion that the technique can indeed be successfully used to measure wall shear stress.

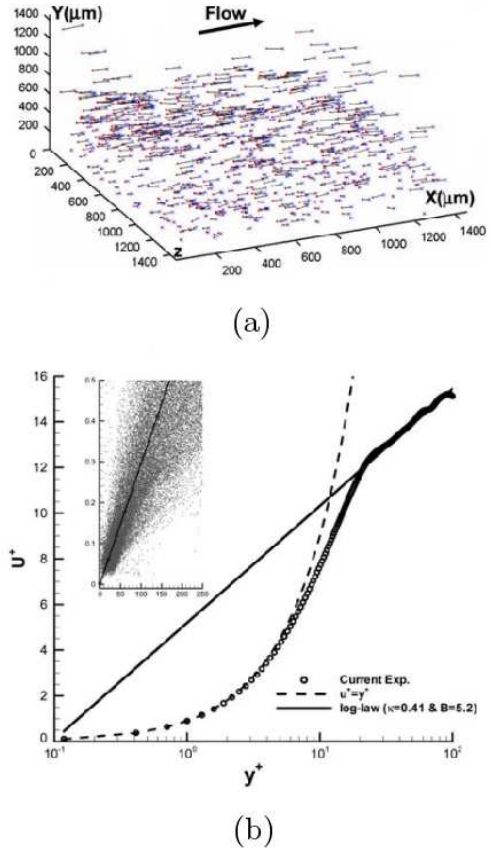

Figure I.2: Results from digital holographic microscopy measurements extracted from [Sheng *et al*, 2008]: (a) Typical instantaneous volumetric velocity field; (b) linear regression of the scatter plot of axial velocity within the viscous sublayer.

Hence, this technique was proven to be able to provide not only mean evaluation of the wall shear stress with very low uncertainty, but to go much beyond that and provide accurate instantaneous spatial distributions as well.

Needless to say, there are several other shear stress measuring techniques available, such as liquid crystals, electromechanical techniques, among others, but the overview presented above was meant to name a few that are currently being widely used, specially the ones making use of velocity field measurements. The important issue, though, is that wall-flow experimental designs should carefully consider what type of wall shear stress information is required to meet the experiment objectives.

I.3 Description of the Current Work

The present work aims primarily at developing and implementing the Digital Holographic Microscopic *PIV* technique in a distinct optical configu-

ration that provides the necessary flexibility to make measurements in different geometries, specially in large wind tunnel facilities such as the one from the *Laboratoire de Mécanique de Lille* (LML).

Following the discussions presented in this introductory chapter, it is clear that the ability to perform experimental measurements in the near-wall region of turbulent wall-bounded flows with increasing spatial and temporal resolution is quite valuable for both research development and practical applications.

It can be concluded from the overview of different techniques that the accuracy in measuring wall shear stress — whether through direct or indirect methods — can still be improved. And, since this quantity is extremely important for proper scaling and comprehension of turbulent boundary layers, attempts to promote accuracy improvements are always welcome.

In this context, the holographic *PIV* technique fits very well, as the somewhat detailed mention to the work of [Sheng *et al*, 2008] presented in the previous section demonstrated so adequately. Not only it can provide mean shear stress measurements with higher accuracy than other methods, but it can also attempt to provide the bonus of well-resolved, three-dimensional, instantaneous fields.

However, in [Sheng *et al*, 2008], the technique was applied to a water flow, and particle seeding could be made locally, in the near-wall region only. Under these conditions, one can manage to adapt the experimental configuration to use *in-line Gabor holography*, which is the simplest optical arrangement for holographic measurements. In a large, close-looped wind tunnel facility, though, seeding is usually spread all over the flow and, as will be made more clear later on, in this case it is unfortunately not possible to implement the in-line configuration. Also, sub-micron particles usually employed to seed wind tunnel flows provide an extra challenge. In the work of [Cao *et al*, 2008], particle clustering inside a wind tunnel is studied with digital holography, but the configuration has some important differences with respect to the configuration proposed here, such as the fact that no magnification is introduced.

Therefore, the goal of this thesis was to develop a side-scattering holographic configuration suited to perform measurements in the very near-wall region of the boundary layer in the LML wind tunnel facility. A scheme was developed so that the reference wave is separated from the wave that illuminates the object, although they come from the same coherent laser source. Light scattered from the object and reference wave then recombine on-axis. With this arrangement, there is a side-scattering configuration for the parti-

cles, but an in-line recording situation. Details on holographic theory will be given in chapter II, and the experimental description of the wind tunnel setup will be presented in chapter IV.

With the application of this form of the technique in the wind tunnel boundary layer, it is expected, at first, that a spatially and temporally averaged velocity profile in the viscous sublayer can be obtained, which can allow a determination of the mean wall shear stress with significantly improved accuracy.

In a preliminary test arrangement, a simpler Gabor in-line holographic setup was mounted separately, in order to make initial tests and provide some random particle spray and target hologram images, for analysis of some basic theoretical aspects. A software was then developed in C^{++} language — *HPIVlml* — for the numerical holographic reconstruction, which could be initially tested with those images.

Finally, the new setup developed for the wind tunnel measurements was mounted. After making several side tests and setting up for the best calibration procedure, wind tunnel measurement runs could be carried out. Several algorithms for all the necessary image processing steps, calibration and detection of focal position of the particles were implemented in the *HPIVlml* software and continuoulsy improved based on the raw data from these runs. Finally, a particle tracking algorithm was written to compute unstructured 3D velocity fields from pairs of reconstructed particle volumes, and from these fields an accurate mean velocity profile can in principle be obtained. Thus, a great amount of the time and effort invested in the work was directed towards the development of the technique itself, comprising both optimization of the optical configuration and software development.

As will be seen in the final chapters, some challenges were encountered along the way, mostly related to the high sensitivity of the holographic — coherent — imaging system to different factors, specially in a more complex optical configuration such as the proposed one. Results on particle detection are quite promising, but also show some need for optimization and provide very interesting topics for discussion.

II
Holography

In this chapter, an overview of important physical concepts and phenomena related to holography, such as interference and diffraction, will be presented. Holographic recording and reconstruction processes will be described, and restrictions and other considerations will be mentioned. Then, additional features will be introduced sequentially: digital holography and numerical reconstruction, holographic microscopy, and finally holograpic *PIV*.

II.1 Basic Physical Concepts

Electromagnetic Waves Some of the phenomena in the physics of light waves, like interference or diffraction, cannot be explained by the optics of rays or particles. They come up because of the wave nature of light.

The simplest waves are described by trigonometric functions such as sines, cosines or complex exponential functions. A wave is determined by its amplitude A, the wavelength λ and the argument of the trigonometric or exponential function, the *phase*. Light is an electromagnetic wave, characterized by electrical and magnetic fields that vary in time and propagate together. Normally it suffices to consider and represent the electric field only. A *transverse* wave vibrates at right angle to the direction of propagation and must be described with vector notation. The effects related to the directions of propagation and vibration are called *polarization* effects. A wave that vibrates in a single plane is called a *plane-polarized* wave.

Unless polarization effects are significant, it is not generally necessary to retain the vector nature of the wavefield and thus light waves may usually be described by the scalar equation

$$E(x,t) = A\cos\left(kx - \omega t + \phi\right), \tag{II.1.1}$$

where $E(x,t)$ is the strength of the electric field, A is the *amplitude* and x the direction of propagation. If the maximum amplitude is not at $x = 0$ and $t = 0$, a *relative phase* ϕ has to be introduced.

The *wavenumber* k is associated to the *wavelength* λ by

$$k = \frac{2\pi}{\lambda}. \tag{II.1.2}$$

The frequency ν of the wave, or number of periods per second, is $\nu = c/\lambda$, where c is the velocity of light. The *angular frequency* ω is related to the frequency ν by $\omega = 2\pi\nu$.

A *wavefront*, term that can be constantly found in holography-related literature (as the scientist who first proposed an holographic process, Dennis Gabor, referred to holography as *wavefront reconstruction*), refers to the spatial distribution of the maxima of the wave, or other surfaces of constant phase, as these surfaces propagate. The wavefronts are normal to the direction of propagation. As an obvious example, the wavefronts of a *plane wave* are planes.

In most cases, complex-exponential functions are used instead of trigonometric functions for convenience, and then the equation for the electric field can be written as

$$E(x,t) = Ae^{-j(kx-\omega t+\phi)}, \tag{II.1.3}$$

if the definition $e^{j\alpha} = \cos\alpha + j\sin\alpha$ is used. The intensity is defined as the absolute square of the electric field,

$$I(x,t) = E(x,t).E^*(x,t), \tag{II.1.4}$$

where * denotes the complex conjugate. $I(x,t)$ is always real. For the usual light detectors, such as the CCD camera sensors, the important quantity is not the field amplitude A, but the intensity I.

Interference and Diffraction The wave nature of light explains certain important optical phenomena like *interference* and *diffraction* that could not be understood with the geometrical approach alone. Diffraction is, for example, responsible for limiting the theoretical resolution of a lens. These phenomena constitute the fundamental physics behind holography (see [Young, 2000]), and their main concepts will be introduced next.

The modification of intensity obtained in the region of crossing when two or more light waves are superimposed is called *interference*. If the resultant intensity is zero or in general less than expected from the separate intensities, there is *destructive* interference, while if it is greater, there is *constructive* interference. When two waves interact, the *principle of superposition* says that the resulting wave function is the sum of the two individual ones. Considering

two waves of different amplitudes and with a phase difference $\Delta\phi = \phi_2 - \phi_1$,

$$\begin{aligned} E_1 &= A_1.e^{-j(kx-\omega t+\phi_1)}, \\ E_2 &= A_2.e^{-j(kx-\omega t+\phi_2)}, \end{aligned} \tag{II.1.5}$$

and superimposing these waves, the resulting electric field is

$$E = E_1 + E_2 = e^{-j(kx-\omega t)}[A_1 e^{-j\phi_1} + A_2 e^{-j\phi_2}], \tag{II.1.6}$$

supposing they are colinear or that only very small angles are involved (as will be seen is the case in *in-line holography*), and thus vector notation can indeed be neglected.

Using the properties of exponentials, the intensity of the superimposed fields is

$$I = A_1^2 + A_2^2 + 2A_1A_2\cos\Delta\phi = I_1 + I_2 + 2(I_1I_2)^{1/2}\cos\Delta\phi, \tag{II.1.7}$$

where I_1 and I_2 are the intensities due to the two waves acting separately. The intensity has its maximum value when $\Delta\phi = 2m\pi$ (constructive interference) and its minimum when $\Delta\phi = (2m+1)\pi$ (destructive interference).

If the waves have the same amplitude and come from the same source but have a phase difference ϕ, the intensity of the superimposed beams can be written as

$$I = 4A^2\cos^2(\phi/2). \tag{II.1.8}$$

Because energy must be conserved, it is not achievable to have constructive intereference without finding destructive interference elsewhere. The alternating light and dark bands are known as *interference fringes*. These fringes correspond to *loci* of constant phase difference (or, in other words, constant optical path difference).

So, in general, according to eq.(II.1.7), the result of superimposing two waves consists of one part that is the addition of the intensities, and another part, the interference term. In the definitions above, it has only been considered the case of *parallelly polarized waves*. In the other extreme are *orthogonally polarized waves*. These waves do not interfere, their superposition only consists of the addition of the intensities $I_1 + I_2$. For other angles between the polarization directions the field vector has to be decomposed into components of parallel and orthogonal polarizations, and the result contains interference parts as well as an addition of intensities. Because in the superposition of incoherent light one always observes a pure addition of the intensities but no interference, the additive term is often called the *incoherent part*.

The *visibility* or *contrast* of the interference pattern is defined by

$$V = \frac{(I_{max} - I_{min})}{(I_{max} + I_{min})}, \tag{II.1.9}$$

and minimum contrast $V = 0$ is expected for incoherent superposition.

Coherence Only light of sufficient coherence will exhibit the effect of interference. Roughly speaking, coherence means the ability of light waves to interefere. More precisely, coherence describes the correlation between individual light waves, or the property of a constant phase relation between two waves. It comprises both *temporal* and *spatial* coherence.

Temporal coherence describes the correlation of a wave with itself at different instants of time, separated by a delay t'. Temporal coherence tells us how monochromatic a source is. In other words, it characterizes how well a wave can interfere with itself at a different time. The delay over which the phase or amplitude wanders by a significant amount - and hence the correlation decreases by a significant amount - is defined as the coherence time ${t'}_C$. At $t' = 0$ the degree of coherence is the highest and it drops significantly by the time delay ${t'}_C$. The *coherence length* L_C is defined as the distance the wave travels in time ${t'}_C$,

$$L_C = c \cdot {t'}_C = \frac{\lambda^2}{2(\Delta\lambda)}, \tag{II.1.10}$$

where $\Delta\lambda \ll \lambda$ is the spectral width of the nearly monochromatic beam and c is the speed of light.

So, the coherence length is the length over which the phase of the beam of light is correlated. In order for interference to occur, the path length difference must be smaller than the coherence length.

Analogously, spatial coherence relates to the spatial dimension presenting a significant variation in the phase relation.

Huygens Principle When waves pass through an aperture, or past the edge of an obstacle, they always spread to some extent into the region which is not directly exposed to the oncoming waves. This phenomenon caused by the confinement of the lateral extension of a light wave is called *diffraction*, and is more pronounced when it takes place in dimensions that are comparable to the wavelength. In order to explain this bending of light, Huygens proposed that each point on a wavefront may be regarded as a new source of small spherical waves. These small waves propagate an infinitesimal distance and their resultants give rise to a "new" wavefront, which merely represents the original wavefront after having propagated for a small distance. The *Huygens*

principle is illustrated in Figure II.1.

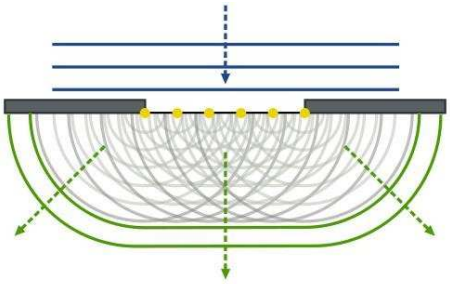

Figure II.1: Illustration of the Huygens Principle

The little waves combined produce a wavefront that is thus outlined by their tangents. The new wavefront is almost plane and almost identical to the original one. In the ends, however, some curvature is developed. In this way, the wavefront becomes spherical and the wave is therefore called *divergent*. *Double-slit* interference, for example, happens because diffraction allows light coming from the two slits to interact. This is shown in Figure II.2.

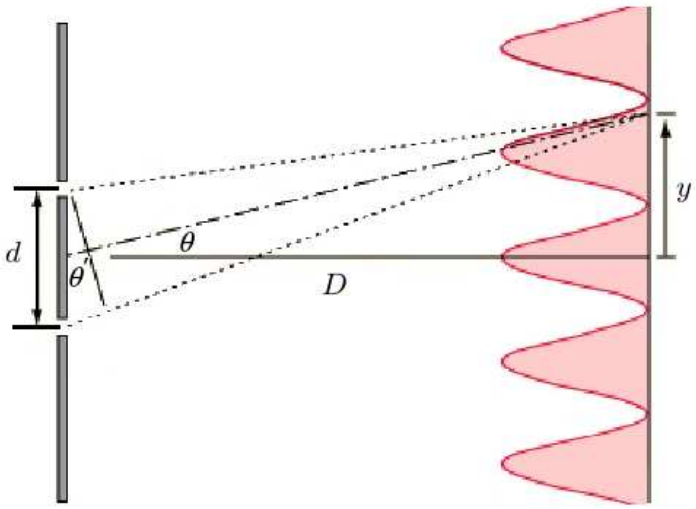

Figure II.2: Double slit interference

Near the slits, when divergence caused by diffraction is not always noticeable, interference is not observed. Far enough from the slits, when divergence is stronger, the diffracted beams begin to superimpose. From this point on, interference effects are important. This configuration describes well the basic principle of interference. Suppose that a monochromatic plane wave is incident upon a screen with two infinitesimal slits separated from each other by a distance d. Each slit behaves as a point source, radiating in all directions. An observation screen is placed at a large distance D from the slits. It is illuminated with light coming from the two slits, and the electric field at a

given point on this screen is the sum of the fields originating from each slit. If D is indeed sufficiently large, the paths are effectively parallel ($\theta' \approx \theta$) and differ only by $d\sin\theta$, which is referred to as *optical path difference*, or *OPD*, the difference between the paths each wave has traveled. The phase difference between the two waves is then $\phi = kd\sin\theta$ and, according to the superposition principles, the intensity in a given point in the observation screen is

$$I = 4A^2\cos^2(\frac{\pi}{\lambda}d\sin\theta). \tag{II.1.11}$$

Thus, for small angles, the interference pattern has a $\cos^2$ variation with y. Maximum values of intensity occur whenever the OPD is an integer multiple of π, that is $OPD = m\lambda$. Similarly, minima occur whenever $OPD = (m + 1/2)\lambda$.

The spacing i between the fringes or maxima can then be found to be

$$i = \frac{\lambda D}{d}. \tag{II.1.12}$$

Fraunhofer and Fresnel Diffraction Diffraction phenomena are divided into two general classes: those in which the source of light and the screen on which the pattern is observed are effectively at infinite distances from the aperture causing the diffraction — *Fraunhofer diffraction*, and those in which either the source or the screen, or both, are at finite distances from the aperture — *Fresnel diffraction*.

Fraunhofer diffraction, which is simpler to treat theoretically, is easily observed in practice by focusing the parallel light from a distant source on a screen, as shown in figure II.3. An objective lens O, supposedly perfect, receives a plane wave originated in a monochromatic point source S located at infinity. The incident wave Σ_0 becomes a spherical wave Σ_1 with center in S'. The image S' of the point source S is not a geometric point, but has a structure determined by diffraction.

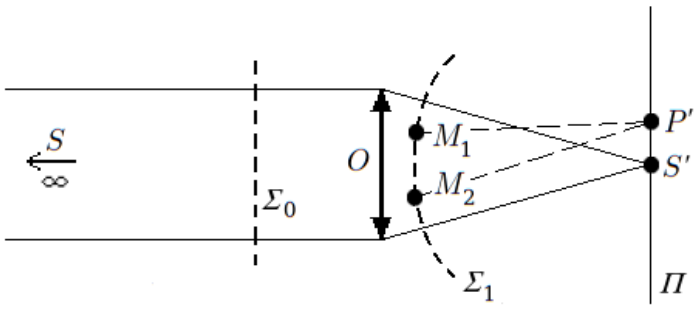

Figure II.3: Diffraction at infinity.

According to the Huygens principle, different points in Σ_1 behave as if they were synchronized coherent sources, and the waves they emit are susceptible to interfere. A given point P' on plane Π will receive the wavelets emitted from all the points in Σ_1. In Figure II.3, two "rays" diffracted by two points M_1 and M_2 are represented. The light intensity in P' is therefore a result of the interferences of the wavelets from all the points. When the intensity in several points of the plan Π is calculated in the neighborhood of S', one obtains the structure of the image of the point source S. This *diffraction image* depends on the form of the boundary that limits the objective O. This is the phenomenon of diffraction at infinity or *Fraunhofer* diffraction. It can be shown that the diffraction figure in $S^{'}$ is related to the Fourier transform of the distributions of amplitudes and phases in wavefront Σ_1.

In Fresnel diffraction, on the other hand, the plane of observation Π'' is at a closer distance to the lens aperture, as shown in figure II.4, and the effect is different from the Fraunhofer diffraction observed in Π. Fresnel diffraction can also be observed when a simple screen D with an aperture is placed between a point source S and the observation plane Π'', as in figure II.5.

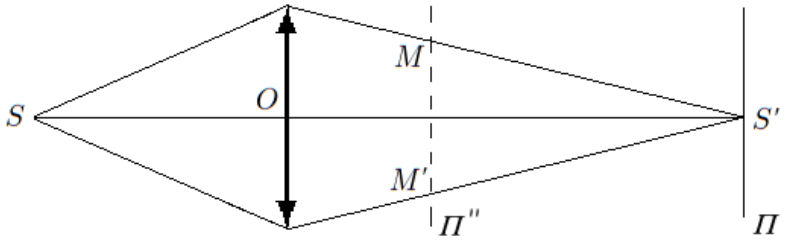

Figure II.4: Near-field or *Fresnel* diffraction at plane Π'': phenomena are practically only observed towards the borders M and M' of the beam. In the plane Π *Fraunhofer* diffraction is observed.

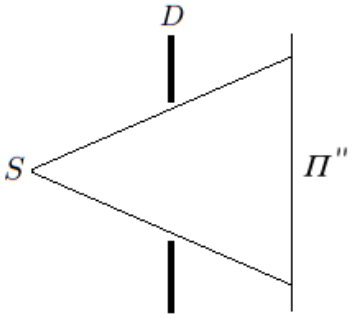

Figure II.5: *Fresnel* diffraction by a screen.

Fresnel diffraction, as mentioned above, refers to the general case in which either the aperture is not illuminated by a collimated beam or the diffracting

screen is not distant compared with the size of the aperture. Discussion of Fresnel diffraction helps in the understanding of the hologram as an imaging device.

Diffraction by a circular sinusoidal diffraction grating Considering a circular sinusoidal diffraction grating, with the law of variation of the transmission factor of the form $\cos^2\Omega^2$ (pattern of concentric rings), if we illuminate it with a beam of parallel rays, it works like a lens with two focal points, one at each side (figure II.6). That is, on the axis, we observe a virtual image S' and a real image S'', and also a direct beam S_0 that passes directly through the grating and is sometimes referred to as the *dc* component.

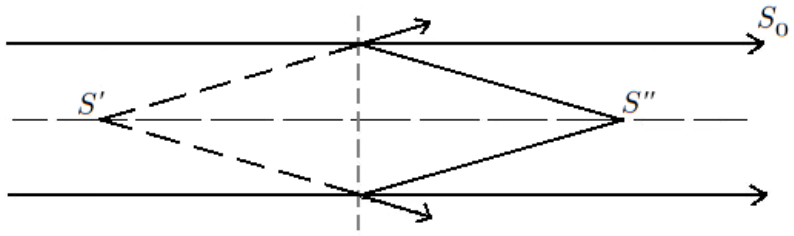

Figure II.6: Diffraction by a circular sinusoidal grating.

Scalar diffraction theory The phenomenon of diffraction introduced above plays a very important role in every field of study concerning propagation of waves. In holography specially, interference and diffraction are the most basic and important physical principles involved. To fully understand the properties of the holographic imaging process, it is essential to appreciate the effects and limitations imposed by diffraction.

A formal mathematical description of diffraction was introduced when it was treated as a scalar phenomenon, leading to the so-called *Rayleigh-Sommerfeld diffraction theory*, explained with a good level of detail in [Goodman, 1968], where the author lays all the mathematical background, based on *Green's theorem*. The theory has a fundamental simplification in which light is treated as a *scalar* phenomenon, that is, only the scalar amplitude of one transverse component of either the electric or the magnetic field is considered, assuming that any other component of interest can be treated independently in a similar way. Nevertheless, the theory yields very accurate results if the diffracting structure is large compared with the wavelength.

Following this theory, a mathematical description of the propagation of a diffracted field is reached. If an approximation considering that the

diffracted fields are not observed too close to the aperture is further introduced (the *Fresnel approximation*), the development leads to the *Fresnel diffraction integral*. It describes the propagating field past the aperture in the region of Fresnel diffraction, or in the *near field* of the aperture.

The Fresnel diffraction integral will be used in the numerical reconstruction of the holograms, which is described in more detail later in this chapter. As for the mathematical development leading to the integral, refer to [Goodman, 1968].

II.2 The Two Steps in the Holographic Process

In 1948, Dennis Gabor proposed a new optical method, lensless and consisting in two steps, which he called "wavefront reconstruction", and which was based on the observation that when a coherent reference wave is present simultaneously with the light diffracted by or scattered from an object, then information about both amplitude and phase of the diffracted or scattered waves is recorded, in spite of the fact that recording media respond only to light intensity. Gabor demonstrated that from such a recorded interference pattern (the hologram), an image of the original object can be reconstructed.

Thus, in this method, nowdays known as *holography*, the light wave used is scattered by an object and superimposed with a reference beam from the same source. In this way, amplitude and phase of the object are recorded on the sensor, in the form of an interference pattern. The pattern produced by a particle, for example, is characteristic of the particle position and size and looks like a circular sinusoidal grating. The location of the center of the pattern relates to its lateral position, and the frequency modulation of the concentric rings carries information about the particle position in depth.

The fundamental task in holography is to record, and later reconstruct, amplitude and phase of an optical wave arriving from a coherently illuminated object. So, the problem of wavefront reconstruction consists in two distinct operations: recording and reconstruction. They will now be explained separately in the context of conventional holography (as opposed to the digital holography technique that will be introduced later on and employed in the work of the thesis).

Recording of the hologram As mentioned above, holography is about detecting both amplitude and phase information. However, all recording media respond only to light intensity. It is therefore necessary that information about the phase of the wave is somehow converted into intensity variations

for purposes of recording. The way to achieve that is through *interferometry*; that is, a second wavefront, mutually coherent with the one coming from the object, and with known amplitude and phase, is superimposed to the unknown object wavefront, as shown in figure II.7.

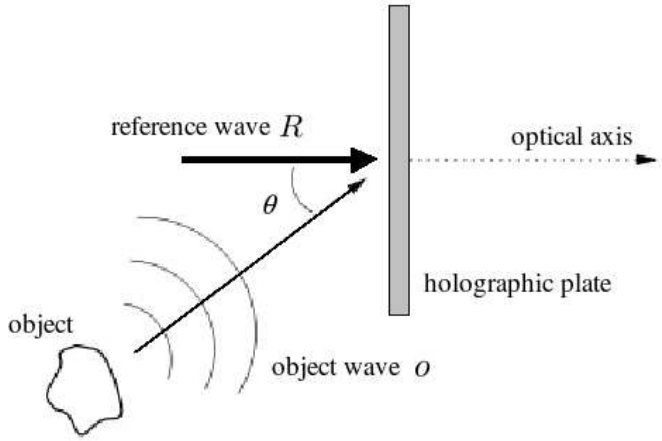

Figure II.7: Recording of a hologram.

The intensity of the sum of the two complex fields depends on both the amplitude and phase of the unknown field. Thus if

$$o(x,y) = |o(x,y)| \exp[-j\varphi(x,y)] \tag{II.2.1}$$

represents the wavefront to be detected and reconstructed (the *object wave*), and if

$$R(x,y) = |R(x,y)| \exp[-j\psi(x,y)] \tag{II.2.2}$$

represents the *reference wave* (which does not necessarily have to be a plane wave) with which $o(x,y)$ interferes, the intensity of the sum is given by

$$\begin{aligned} I(x,y) &= |R|^2 + |o|^2 + R^* o + R o^* \\ &= |R(x,y)|^2 + |o(x,y)|^2 + 2\,|R(x,y)|\,|o(x,y)| \cos[\psi(x,y) - \varphi(x,y)]. \end{aligned} \tag{II.2.3}$$

The first two terms of the bottom row expression depend only on the intensities of the individual waves, but the third depends on their relative phases. Thus, the goal of recording information about both amplitude and phase of the object wave $o(x,y)$ is achieved. The hologram is the recording of the interference pattern between object and reference waves. Because an interfering unfocused wavefront in the Fresnel region of diffraction is recorded, the holograms are called *Fresnel holograms*.

In conventional holography, the recording media is a holographic plate

and is made of a material that is assumed to provide a linear mapping of intensity incident during the detection process, given by eq.(II.2.3), into transmissivity after photographic development:

$$t_A(x,y) = t_R + \beta(|R|^2 + |o|^2 + R^*o + Ro^*), \tag{II.2.4}$$

where t_R is a uniform transmittance established by a direct reference exposure and β is a constant, characteristic of the linear behavior of the material. These plates are meant for *optical*, not digital reconstruction.

So, this kind of plate, which registers the interference pattern in the recording step, later — after being photographically developed — acts like a diffraction grating (see figure II.6) in the second step, the reconstruction step, which will be explained next.

Reconstruction of the original wavefront Having recorded amplitude and phase information about the object wave $o(x,y)$, reconstruction of that wave can be performed. If the object is removed, and the developed transparency is illuminated by a *reconstruction wave* that is a replica of the reference $R(x,y)$, the light transmitted by the transparency is

$$R(x,y)t_A(x,y) = t_R R + \beta R|R|^2 + \beta R|o|^2 + \beta R^* Ro + \beta RRo^*. \tag{II.2.5}$$

The transmitted wavefront is thus composed of four terms:

$$U(x,y) = U_1(x,y) + U_2(x,y) + U_3(x,y) + U_4(x,y), \tag{II.2.6}$$

each one of them being

$$\begin{aligned} U_1(x,y) &= \left(t_R + \beta|R|^2\right) R(x,y) \\ U_2(x,y) &= \beta R(x,y)|o(x,y)|^2 \\ U_3(x,y) &= \beta|R(x,y)|^2 o(x,y) \\ U_4(x,y) &= \beta|R(x,y)|^2 \exp[-2j\psi(x,y)]o^*(x,y). \end{aligned} \tag{II.2.7}$$

1. $U_1(x,y)$ is directly proportional to the reference wave, that is, the attenuated reference wave transmitted directly through the hologram, or the *dc* term (as in figure II.6).

2. $U_2(x,y)$ is the autocorrelation of the speckle field from the object, and can be seen as a "cloud" covering central parts of the reconstructed wavefield.

3. $U_3(x,y)$ is proportional to the object wave and gives rise to a *virtual*

image in the exact same position as the original object in the recording setup. Up to a multiplicative constant, it is an exact duplication of the original object wavefront.

4. $U_4(x, y)$ is proportional to the conjugate object wave, with a phase factor, and converges to a *real* image in front of the hologram.

The two first terms constitute the *zeroth order* diffraction. The reconstruction process is illustrated in figure II.8. By looking through the hologram, one can see a three-dimensional image that is almost impossible to distinguish from the original object, with parallax and depth of focus. This is the *virtual* image generated by U_3, as opposed to the *real* or *conjugate* image generated by U_4, which is another copy of the original object wave, but focused on the opposite side of the plate.

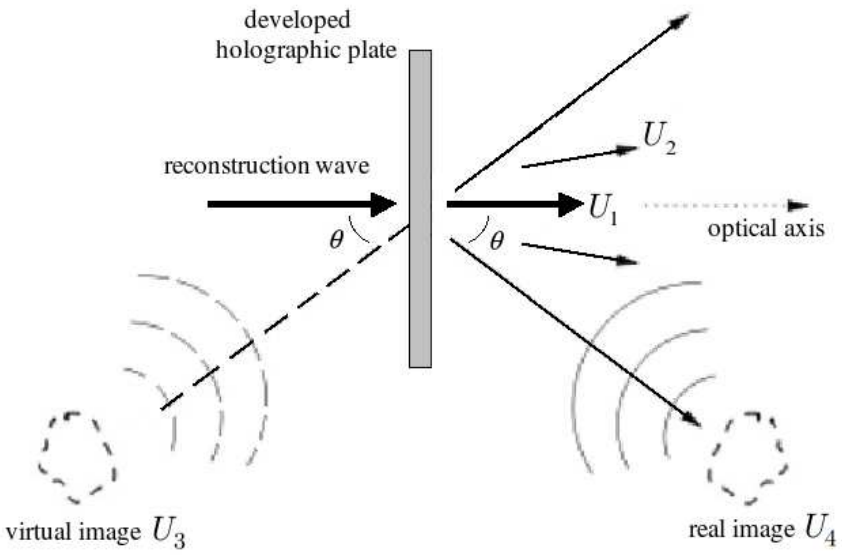

Figure II.8: Optical reconstruction of the original wavefront.

Analogously, if the conjugate of the reference wave, R^*, is used as the reconstruction wave, the term U_4 becomes proportional to the conjugate of the original wavefront. In either case, the original object is reconstructed, and the field of interest (the object field) is accompanied by three other field components.

Despite the fact that — for didactic purposes — the reasoning above refers to a case in which the reconstruction wave is exactly the same as the reference wave used in recording, this is not a necessary condition in the holographic image formation process. In fact, in some cases, specially when the reference wave used is non-collimated, it might be difficult to faithfully reproduce it in the moment of reconstruction (for a diverging wave, such

faithfullness depends mostly on the correct positioning of the reconstruction wave source). Departure from the condition in which the two waves are the same will simply affect positions and magnifications of the reconstructed real and virtual images, in a way that can be predicted by equations. Those equations, along with some considerations about this matter, are presented in Appendix A. But basically, the reason why reference/reconstruction source distances are an important issue in the case of diverging beams is that the angles of the interfering "rays" on a given plane in the optical axis will be different depending on these distances, leading to interference patterns that will in turn reconstruct differently.

II.3 In-line Holography

In figure II.7, object and reference waves are separated, and there is an angle θ between them. This configuration is called *off-axis holography*. In this case, the resulting real and virtual images are angularly separated from each other and from the other wave components U_1 and U_2 in the reconstruction.

But in the configuration originally proposed by Gabor, referred to as *in-line holography* or *Gabor holography*, all the setup is along the axis normal to the plate, the optical axis, as shown in figure II.9. The same wave that illuminates the object serves as the reference wave. This is only possible with objects that are transparent containing only small opaque details on a clear background, as in the case of a group of very small particles in *PIV*.

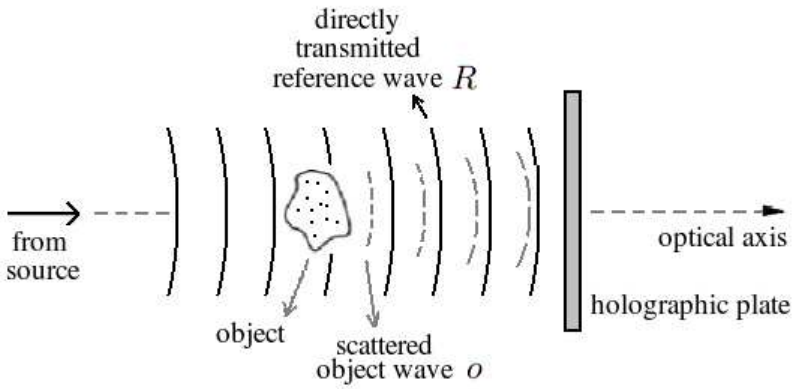

Figure II.9: Recording of an *in-line* or *Gabor* hologram.

In the reconstruction process (figure II.10), when illuminated by the reconstruction wave equal to the original reference wave, Gabor holograms generate simultaneous real and virtual images, both being centered on the hologram axis. These so-called *twin images* are separated by the axial distance $2z_0$, z_0 being the distance of the object to the hologram plane in the recording

step, and are accompanied by a coherent background coming from the other reconstruction terms. The twin images overlap; when the real image is brought to focus, it is always accompanied by an out-of focus virtual image. Likewise, an observer viewing the virtual image sees simultaneously a defocused image arising from the real image term.

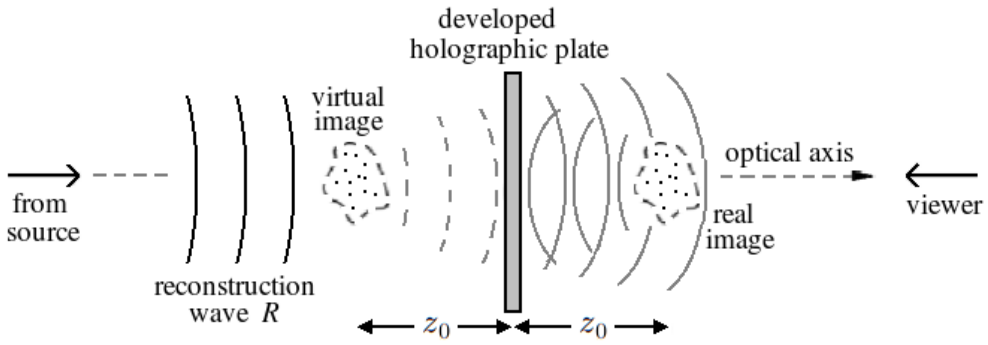

Figure II.10: Reconstruction of an in-line hologram: *twin* images are formed at a distance z_0 in each side of the hologram.

II.4 Digital Holography

A wavefront can be recorded on a digital detector and numerically reconstructed by a computer. The idea was first proposed by [Goodman and Lawrence, 1967] and [Kronrod *et al*, 1972], but at that time, insufficient computer capacity and sensor technology made applicability quite difficult. The principle of *digital holography* became recently accessible thanks to the technological advances in the computational area and in sensor resolution and performance ([Meng *et al*, 2004]).

The first step in the holographic process — recording — is performed optically, but the traditional recording medium, the holographic plate, is replaced by an electronic device such as a digital CCD camera with the lens removed. The interfering wavefront is digitized and stored in the form of a grey-level image in a computer. With the digital hologram as the basis, the second step — reconstruction — consists in a numerical simulation of wave propagation. No cumbersome chemical processing is necessary as in conventional holography.

A numerical method for the reconstruction of Fresnel holograms recorded with a CCD camera was also reported pioneerely by [Schnars and Juptner, 1994], and from then on many research groups have been applying it in different forms for various applications, among them fluid flow characterization.

The spatial frequency of the interference fringes is proportional to the angle formed by the object scattering direction and the reference beam direction. Fringe spacing is thus a function of the origin of the diffracted light, and is therefore related to the depth position of the points comprising the object (or, for example, to the depth position of a small particle, if a small particle is the object). The axial resolution of digital holographic techniques is still poor compared to traditional holography even with state-of-the-art CCD sensors because the digital sensor elements cannot resolve interference fringes finer than the pixel size, and the permissible angle between object and reference waves is limited to a few degrees (restrictions are later presented in more detail). As a consequence, only in-line configurations are employed in digital holography to the moment. Figure II.11 shows three distinct possibilities for in-line recording configurations, each of them having its particular advantages. For reasons that will be clear in chapter IV, in which the holographic setup for wind tunnel measurements is described, the chosen configuration for the present thesis work resembles the one from figure II.11(b), although it presents important differences such as the introduction of a varying magnification effect through the use of a microscope objective in the system.

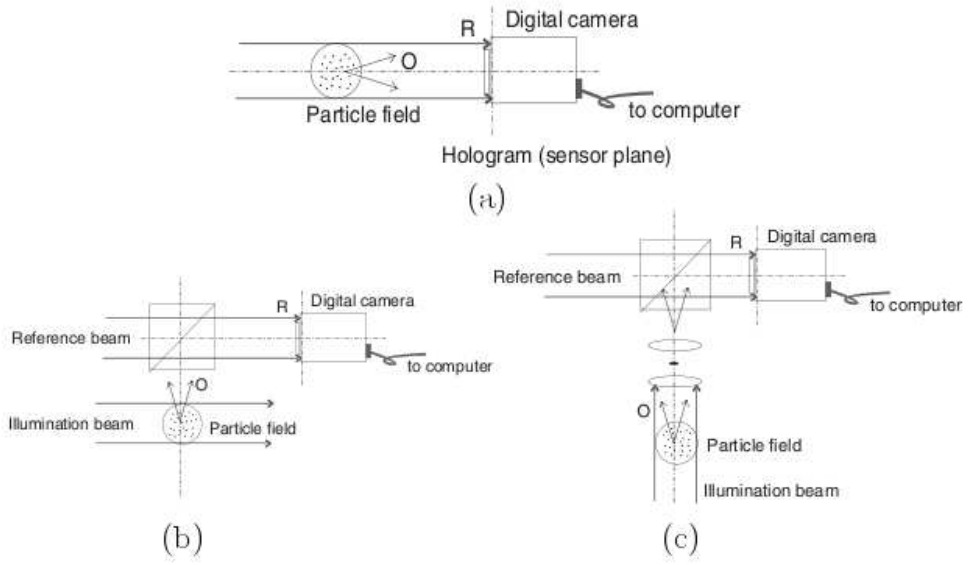

Figure II.11: Three possible recording configurations for digital *HPIV*, extracted from [Meng *et al*, 2004]: (a) single-beam in-line holography with forward scattering, (b) dual-beam in-line holography with 90^o scattering and (c) dual-beam in-line holography with forward scattering.

Numerical reconstruction The wavefront reconstruction can be explained by the diffraction theory presented earlier. The hologram acts ideally like a superposition of diffraction gratings that resemble the sinusoidal one shown

in figure II.6. This kind of diffraction grating, as shown before, gives rise to diffraction orders $+1$ and -1, thus acting like a lens with a positive and a negative focal length, corresponding in the analogy to the real and virtual images of each point in the original object. This interpretation of the hologram shows immediately not only why two reconstructions exist, but points to their locations as well.

Figure II.12 represents the reconstruction geometry, in which the z-axis is the optical axis. The hologram is positioned in the (ξ, η) plane, where $z = 0$, while (x, y) is the original object plane during the previous recording step, and (x', y') is an arbitrary plane of observation. All planes are normal to the optical axis.

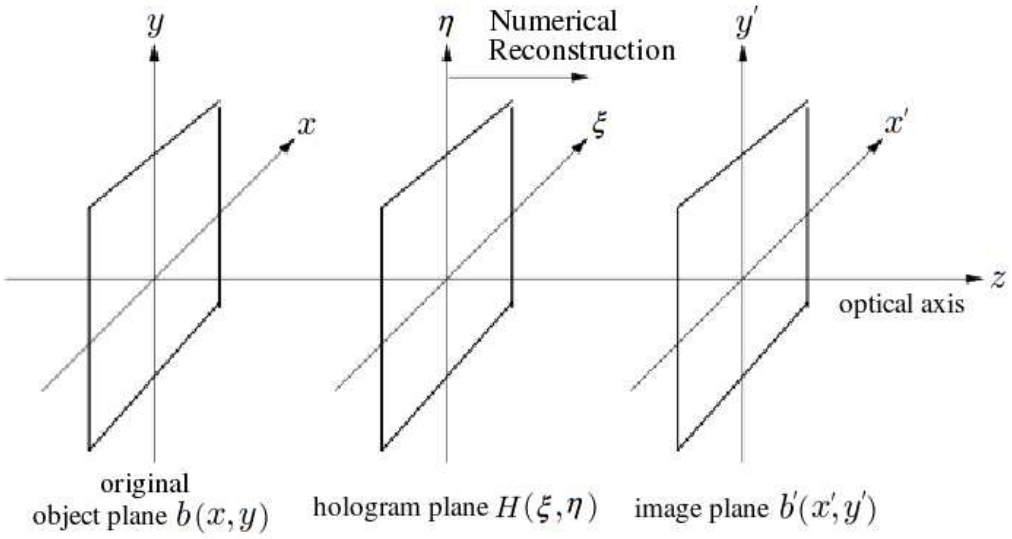

Figure II.12: Geometry and coordinates for representing numerical reconstruction.

During reconstruction, the hologram acts like an aperture that diffracts the reconstruction wave, and the propagation of the wavefield $H(\xi, \eta)R'(\xi, \eta)$ from the hologram plane to a plane of observation is numerically simulated. $H(\xi, \eta)$ is the transmittance distribution in the hologram — recorded as a grey level distribution in the camera sensor — and $R'(\xi, \eta)$ is the distribution of the reconstruction wavefront in the plane of the hologram.

Notice that, from this point on, the fact that in practice the reconstruction wave is not necessarily an exact replica of the reference wave R used in the recording step is taken into consideration, and to imply this, reconstruction wave is represented by R'. Furthermore, neither reference nor reconstruction waves are necessarily collimated, so that R' is represented in the most generic form as a spherical wave, whose distribution in the hologram plane can be expressed as:

$$R'(\xi,\eta) = \exp\left\{-j\frac{k}{2z_{R'}}\left(\xi^2+\eta^2\right)\right\}, \tag{II.4.1}$$

for a wave centered in the optical axis. $z_{R'}$ is the distance from the reconstruction wave source to the plane where it is being represented, in this case the (ξ,η) plane. Details on sign conventions and different choices of numerical representation of the reconstruction wave in the holographic reconstruction process are presented in Appendix A.

A detailed derivation of the mathematical formulae of diffraction theory is given by [Goodman, 1968]. Basically, if $b'(x',y')$ is the reconstructed wavefront in a given plane of observation, then the Rayleigh-Sommerfeld diffraction integral can be written as

$$b'(x',y') = \frac{1}{j\lambda}\iint H(\xi,\eta)R'(\xi,\eta)\frac{e^{jk\gamma}}{\gamma}\cos\Omega\, d\xi d\eta, \tag{II.4.2}$$

where the integration is carried out over the hologram surface and

$$\gamma = \sqrt{z^2+\left(x'-\xi\right)^2+\left(y'-\eta\right)^2} \tag{II.4.3}$$

is the distance from a given point in the hologram plane to a point of observation. $\cos\Omega$ is an *obliquity factor* normally set to one because of the small angles involved.

The *Fresnel approximation* can be used in equation (II.4.3) by applying a binomial expansion [Goodman, 1968] of the square root, leading to

$$\gamma \approx z\left[1+\frac{1}{2}\left(\frac{x'-\xi}{z}\right)^2+\frac{1}{2}\left(\frac{y'-\eta}{z}\right)^2\right]. \tag{II.4.4}$$

A sufficient condition for this approximation to be sustained is that the distance z satisfies

$$z^3 \gg \frac{\pi}{4\lambda}\left[\left(x'-\xi\right)^2+\left(y'-\eta\right)^2\right]_{max}^{2}. \tag{II.4.5}$$

Since this is an overly stringent condition, even shorter distances produce accurate results. The exponent is the most critical factor in equation (II.4.2), and keeping only the first term of the expansion in the denominator produces only very small errors. Thus, the propagation integral (II.4.2) becomes

$$b'(x',y') = \frac{e^{jkz}}{j\lambda z}\iint H(\xi,\eta)R'(\xi,\eta)e^{j\frac{k}{2z}\left[\left(x'-\xi\right)^2+\left(y'-\eta\right)^2\right]}\, d\xi d\eta. \tag{II.4.6}$$

Equations (II.4.2) and (II.4.6) represent a complex wavefield with intensity and phase distributions I and ψ given by

$$I(x',y') = b'(x',y')b'^{*}(x',y'), \;\; \psi = \arctan\frac{\Im\{b'(x',y')\}}{\Re\{b'(x',y')\}}, \tag{II.4.7}$$

where $\Im\{b'\}$ and $\Re\{b'\}$ denote the imaginary and real parts of b', respectively.

There are two ways of implementing equation (II.4.6) in a computer: the *Fresnel* and the *convolution* methods. Both approaches convert the diffraction integral into one or more *Fourier Transforms*, which make numerical implementation easier by the use of *Fast Fourier Transform* (FFT) algorithms.

Here, the *convolution approach* is used. In this case, the reconstructed field in the paraxial approximation can be written in the form of a convolution, that is, equation (II.4.6) is represented as

$$b'(x',y') = e^{jkz}\iint H(\xi,\eta)R'(\xi,\eta)h_z(x'-\xi,y'-\eta)\,d\xi d\eta, \tag{II.4.8}$$

with the convolution kernel being

$$h_z(x',y') = \frac{1}{j\lambda z}\exp\left(j\pi\frac{x'^2+y'^2}{\lambda z}\right). \tag{II.4.9}$$

Thus, the field can be represented more briefly by

$$b'(x',y') = e^{jkz}H.R' \otimes h_z, \tag{II.4.10}$$

where $\otimes$ denotes the convolution operation.

The *convolution theorem* states that the Fourier transform of the convolution of $H.R'$ with h_z is the product of the individual transforms $F\{H.R'\}$ and $F\{h_z\}$. Thus, the wavefield can be found as the inverse transform

$$b'(x',y') = e^{jkz}F^{-1}\{F\{H.R'\}F\{h_z\}\}. \tag{II.4.11}$$

An analytical solution for the Fourier transform of the convolution kernel h_z is given by

$$F\{h_z(x',y')\} = H_z(f_x,f_y) = e^{-j\pi\lambda z({f_x}^2+{f_y}^2)}, \tag{II.4.12}$$

where f_x and f_y are the spatial frequencies of the two-dimensional function. So, finally, the field is expressed as

$$b'(x',y') = e^{jkz}F^{-1}\{F\{H.R'\}H_z\}. \tag{II.4.13}$$

It can be shown that the use of two Fourier transforms — one for taking the transform of the hologram (multiplied by the reconstruction wave), and another for taking the inverse transform — leads to a cancellation of the

scale factor between the input and output fields to make the pixel size of the reconstructed image equal to that of the sampled hologram (i.e., $\Delta\xi = \Delta x'$ and $\Delta\eta = \Delta y'$), in a way that the actual sizes of input hologram and reconstructed images are the same.

Thus, this method — which uses the diffraction integral with the Fresnel approximation and the convolution representation — requires two Fourier transforms, but has the advantage of keeping constant the length scales of the reconstructed images for all distances satisfying the near-field approximation.

Discretization The holograms, in the case of digital holography, are discrete sets of numbers $H(K\Delta\xi, L\Delta\eta)$ — K and L being integer counters — taken on a rectangular $M \times N$ matrix with steps $\Delta\xi$ and $\Delta\eta$ along the coordinates (naturally, this matrix corresponds to the CCD sensor, M and N are the number of pixels in the horizontal direction ξ and vertical direction η, respectively, and $\Delta\xi$, $\Delta\eta$ are the horizontal and vertical dimensions of a pixel).

Therefore, a numerical implementation of equation (II.4.13) must be the equivalent two-dimensional discrete Fourier transform ([Kreis *et al*, 1997]). Spatial frequencies in the discrete implementation are $f_x = \frac{K}{M(\Delta\xi)}$ and $f_y = \frac{L}{N(\Delta\eta)}$.

A more detailed description of the manner in which equations and wave representations were discretized for software implementation is given in Appendix B.

Requirements and restrictions Since digital holography is based on digital sampling of the interference field between reference and object waves, the finite size and resolution of the detector elements can impose limitations on the application of the method.

The sampling theorem According to the Whittaker-Shannon sampling theorem ([Goodman, 1968]), a minimum of two sample points are needed per fringe period to assure an exact recovery of the original function. So, the spatial periods (i_x, i_y) of the fringe pattern that can be resolved by the CCD are given by

$$i_x \geq 2(\Delta\xi), \;\; i_y \geq 2(\Delta\eta), \tag{II.4.14}$$

where $\Delta\xi$ and $\Delta\eta$ are dimensions of the pixel element as defined before.

The minimum fringe spacing i_{min} encountered in the interference pattern is dictated by the maximum angle between rays from the object and reference sources, θ_{max}, through the following interference relation:

$$i_{min} = \frac{\lambda}{2\sin(\frac{\theta_{max}}{2})}, \tag{II.4.15}$$

By combining equations (II.4.14) and (II.4.15), and assuming $\sin\theta \approx \theta$, an important relationship describing the limitations on the angular extent of the setup is found to be

$$\theta < \frac{\lambda}{2\Delta}, \tag{II.4.16}$$

in which Δ is the larger lateral dimension of the pixel element in case the pixel is not square.

This constraint can be severe for off-axis holography, in which for a pixel size of around $\Delta = 7\ \mu$m and laser wavelength of 532 nm the maximum allowed angle is $\theta_{max} = 2.2^o$. For in-line holograms the restriction still exists, but it is much less severe, relating only to the lateral extent D of the object and its distance to the sensor, according to figure II.13. In this case, equation (II.4.16) leads to

$$L_{min} = \frac{D}{\theta_{max}} = \frac{2\Delta D}{\lambda}. \tag{II.4.17}$$

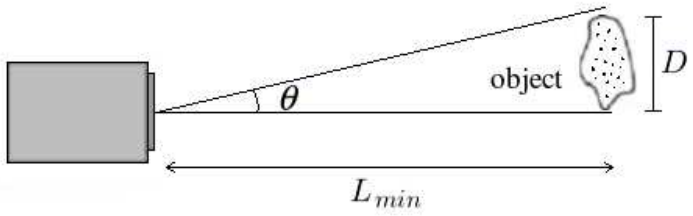

Figure II.13: Limitation in the angular extent for the in-line configuration.

Angular aperture and the axial resolution problem As in any imaging system, the finite aperture of the hologram limits the resolution of a reconstructed image and extends the depth over which this image remains nearly in focus.

For a point source in a diffraction-limited system, around 80% of the energy stays in the so-called *Airy spot*[1] when the image is defocused by δ,

$$\delta = \lambda/2\Omega^2, \tag{II.4.18}$$

[1]The diffraction pattern resulting from a uniformly-illuminated circular aperture, such as a lens, has a bright region in the center, known as the *Airy disk* or *Airy spot*, which together with the series of concentric bright rings around it is called the *Airy pattern*.

where Ω is the effective angular aperture (half-angle) of the imaging system and λ is the wavelength of light. Hence, the depth of focus of the point source is 2δ. For a finite-size particle, the depth of focus is much larger.

So, small apertures in a holographic system will lead to a particle image with an elongated shape, as shown in figure II.14, and consequently to a poor axial resolution δ_z.

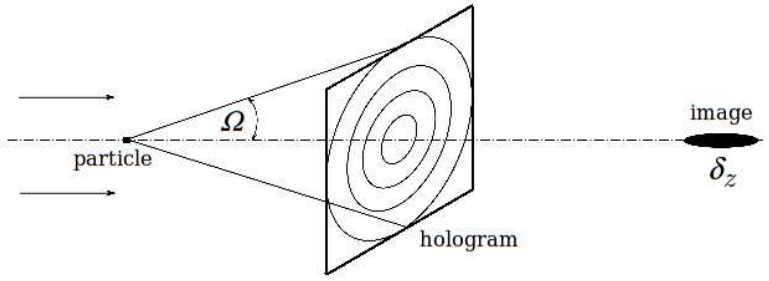

Figure II.14: Reconstruction of a small particle with axial resolution δ_z.

When forward scattering is used in the holographic setup, the particle image is mainly formed by the narrow central Mie-scattering lobe that has a half angular aperture of $\Omega = \lambda/d$, where d is the particle diameter. This aperture is usually much smaller than the aperture determined by the hologram size, and hence particle images formed by forward scattering as in the in-line Gabor configuration have a remarkably large depth of focus.

When side scattering is used, there is no dominant scattering lobe, and the angular aperture of the setup depends mainly on the effective hologram size and recording distance. Because of that, side scattering holograms usually have larger angular aperture and smaller depth of focus, which is a good advantage.

II.5 Digital Holographic Microscopy

In a digital holographic microscopy (*DHM*) configuration, high magnification ratios can be obtained by inserting an imaging system — usually a microscope objective lens — that magnifies the size of the object. However, the object is not imaged directly on the sensor array. The image plane may lie in a plane behind or in front of the sensor (hologram) plane.

Refocusing by a digital holographic microscope is based on obtaining, through numerical reconstruction, the magnified complex optical field at any plane along the propagation of the object beam. It has been explored in different holography-based research works recently, mostly in an attempt to overcome the resolution limitations associated with digital holography.

Many studies successfully demonstrated the ability of digital holographic microscopy to resolve microscopic objects with high spatial resolution. To mention a few examples, the work of [Dubois *et al*, 1999] applies *DHM* for three-dimensional imaging of different microscopic objects, namely a small ruler, 40 μm diameter glass spheres, and biological samples, in a transmission microscope configuration with a partially coherent source to alleviate the problem of coherent noise. In a subsequent work ([Dubois *et al*, 2006]), the authors apply the same principle to further investigate a three-dimensional particle flow and successfully measure particle size.

[Cuche *et al*, 1999] used the technique on a small test target and argued that in holographic microscopy, the resolution with which the magnified image of the object is reconstructed can be equal to the diffraction limit of the objective.

In [Sheng *et al*, 2006], the authors combine in-line digital holography with a microscope objective to circumvent the obstacles of limited resolution associated with digital in-line configurations. They measure particle (ranging in diameter from 0.75 to 3 μm) fields with depths from $1-10$ mm as a means of demonstrating and quantifying the efficacy of *DHM* to largely extend the depth of field of a microscope, and provide detailed data on the spatial resolution in all directions. The presented data confirms that *DHM* maintains the lateral resolution of a microscope while substantially reducing the so-called depth-of-focus problem associated with in-line holography, enabling reconstruction of the 3D coordinates of a dense cloud of particles in a liquid suspension. They also point out that for their configuration, the image plane contains a magnified hologram with a phase correction that becomes unity when the magnification is sufficiently large, so that other than the magnification itself, no other complex effects need to be estimated. Based on the results, they claim that the typical elongation of the particle images in the depth direction still exists, but is at least one order of magnitude smaller than that of a lensless in-line hologram. The problem decreases with increasing magnification (magnifications go from 10 to 40), with particle image elongations ranging between 10 and 2 particle diameters (see figure II.15). However, the authors point out that the magnification of the hologram has to be set with care, because with increasing magnification, the field of view decreases. High-frequency real fringes are the result of interference between diffracted and undisturbed reference waves, and are thus a function of the origin of the diffracted light (depth); the low-frequency amplitude modulation — which is like an imaginary "envelope" around the high-frequency "carrier" function — holds particle shape information (it is the diffraction pattern of an aperture).

A reduced field of view due to increasing magnification limits the extent of the envelope being recorded, which would result in a smoothed boundary during reconstruction.

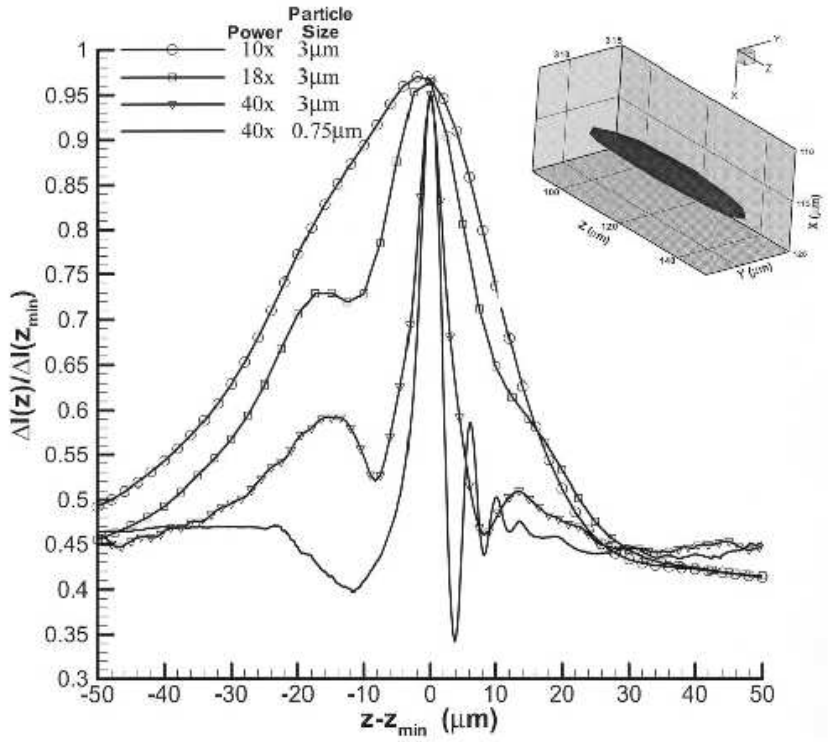

Figure II.15: [Sheng *et al*, 2006]: Ensemble-averaged intensity distribution along the depth direction. The insert is an isointensity surface plot of a typical reconstructed particle at 75% of its peak intensity.

II.6 Holographic PIV

For the purpose of obtaining 3D velocity fields, holography has to be used within the context of the particle image velocimetry technique. In this case, instead of having pairs of 2D particle images to correlate as in classical *PIV*, one has pairs of two-dimensional holographic images, which in turn generate 3D particle fields after reconstruction. The holograms are taken in pairs with a known time interval Δt between them, just like in classical *PIV*. Each pair of holograms can generate an instantaneous 3D-3C velocity field. It is clear that the object is, in this case, the cloud of particles in the measurement volume within the flow illuminated by the laser beam. The *object beam* is then the combination of the light scattered by each particle individually.

Throughout the previous sections, different concepts in holography were introduced. Off-axis and in-line configurations were presented, both "conven-

tional" and digital holography were described, and the use of holographic microscopy was mentioned.

Specifically with the purpose of obtaining three-dimensional particle and velocity fields, many researchers have been using different holographic configurations for a long time. Initially, the studies were performed using conventional holography. The holographic film — which has a very high spatial resolution even compared to modern CCD sensors — had to be chemically developed after recording, and the reconstruction process had to be carefully carried out in the laboratory under appropriate conditions. Finally, a camera would mechanically scan through the physical reconstructed volume, plane-by-plane, to register a series of images comprising the volume.

Important developments in holographic *PIV* and also an improvement in the knowledge on characteristics of the holographic particle image formation process ([Meng *et al*, 1993], [Chan *et al*, 1996], [Pu and Meng, 2003], [Pu and Meng, 2004]) were achieved in this manner, with both in-line and off-axis configurations, before digital holography was viable for that kind of goal. For this reason, it is important to mention a few of the pre-digital holographic *PIV* research works and the progress achieved by them in terms of overcoming restrictions and coming up with ideas for distinct optical configurations and applications.

In the work of [Barnhart *et al*, 1994], a holographic *PIV* system was employed to measure turbulent velocity fields with a spatial resolution high enough to resolve fine scales of the flow, in a measurement volume large enough that the spatial and velocity dynamic ranges were around 100 : 1. An off-axis system with dual reference beam — to allow for separate reconstruction of the frames — was implemented to achieve smaller depth of focus in the particle images, and image aberrations due to optical components were corrected through the use of phase-conjugate reconstruction (when the conjugate reference beam is used, the image propagates back through the original imaging system, such that the original phase front is recovered and the aberration is removed).

A new configuration based on in-line recording and off-axis viewing of the reconstructed fields was developed in [Meng and Hussain, 1995]. The authors observed that prior approaches (e.g., off-axis holography) to overcome the limitations of in-line holography for particle fields — namely, intrinsic speckle noise and poor depth resolution — involved an increased complexity of the optical system. Hence, they used a single laser beam to record an in-line hologram, which was then viewed off-axis during reconstruction (the camera used to scan the particle images in the volume diffracted by the developed

holographic plate is positioned with an angle relative to the optical axis of the system). Measurements were made of the three-dimensional flow of a vortex ring, and the authors showed that both signal-to-noise ratio and depth resolution are higher than conventional in-line holography by one order of magnitude and comparable with off-axis holography.

The use of in-line holographic *PIV* to measure turbulent flows was also studied in [Scherer and Bernal, 1997], where the system was implemented in a 2 ft $\times$ 2 ft water channel to measure the velocity field in a turbulent free-surface jet. A study of different combinations of system parameters was carried out in order to outline a design procedure for selecting particle diameter and concentration based on facility size and geometry, in a way to optimize resolution and dynamic range of the measurements. The criteria were based in noise limitations and resolution requirements that had been identified for in-line holographic recording. The authors achieved a 1 mm spatial resolution, and the field of view was approximately 100 mm.

A "hybrid" holographic system attempting to combine advantages of both in-line and off-axis holography was developed in [Zhang *et al*, 1997] and tested in a turbulent flow in a square duct. The principle was to employ a forward scattering arrangement with blockage of the *dc* component by means of a high-pass filter, and use a separate reference with an angle. This allowed an increase in the energy of the subject beam without over-exposing the holographic film, since most of the energy (*dc* component) was blocked by the filter. "Optical inversion" similar to the conjugate reconstruction in [Barnhart *et al*, 1994] was also used to remove aberrations caused by the relay lenses. Such system was able to provide higher signal-to-noise ratio and lower depth-of-focus, larger dynamic ranges in the measurements, and eliminate speckle noise associated with in-line holography, while keeping its high forward scattering efficiency. The measurement volume in the square duct was $57 \times 57 \times 50$ mm^3. Two mutually perpendicular hybrid systems were mounted, and mass conservation was used for checking results. Deviation from the equation decreased rapidly with increasing size of the control volume used for interrogation in velocity calculations, and a deviation level of less than 10% could be achieved.

A side scattering off-axis configuration was used for pipe flow measurements in [Chan and Li, 1998], in which phase-conjugate for aberration correction was also used. Resulting streamwise velocity error was estimated to be around 5%. A similar arrangement, off-axis with side scattering, was also employed in the work of [Pu and Meng, 2000], with dual reference beams for the double-exposure hologram, so that the holographic images could later be re-

constructed alternately in time. The system was tested in jet and wake flows, and processing and centroid-fitting algorithms were presented for automated particle detection. Figure II.16, extracted from this work, exemplifies the kind of results the authors obtained and that conventional holographic *PIV* can provide.

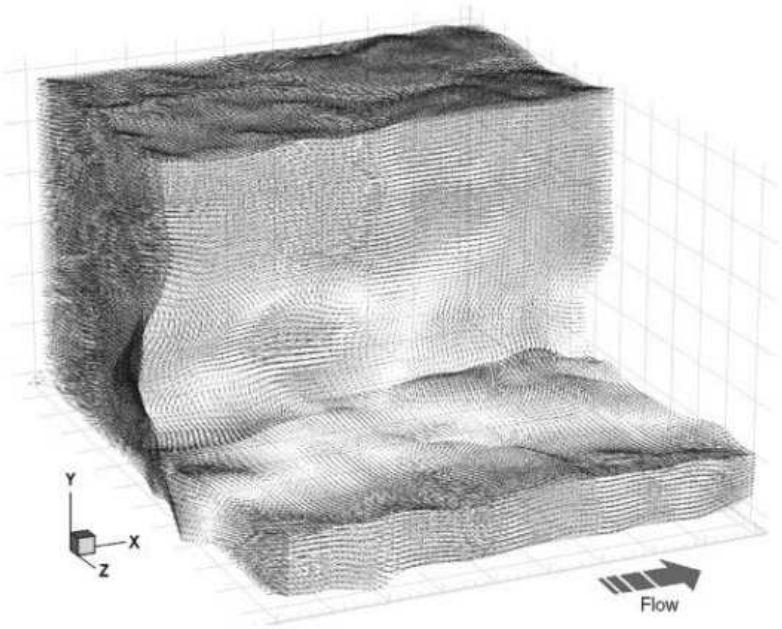

Figure II.16: Example extracted from [Pu and Meng, 2000]: An instantaneous 3D velocity field obtained from the tab wake obtained by *HPIV*. The measurement volume is $44 \times 56 \times 32$ mm. Approximately 400.000 3D vectors have been gaussian-interpolated from about 80.000 paired vectors originally extracted. Mean velocity of the vectors has been subtracted and part of the measurement volume is cut out to show flow structures. For clarity, only surface vectors are shown.

A more specific flow situation — the flow within the cylinder of a four-valve internal combustion engine — was studied with an off-axis configuration in [Konrath *et al*, 2002], where complex-conjugate reconstruction was again used to cancel out image aberrations in the setup.

Spatially and temporally resolved flow measurements became tangible by the time four-dimensional dynamic flow measurements were reported in [Pu and Meng, 2005]. The system was based on the previously reported *HPIV* off-axis setup with 90^o scattering ([Pu and Meng, 2000]), and some design optimizations were made, which incorporated some new insights on holographic particle imaging characteristics. They argued, for example, that the negative effect of intrinsic Mie scattering aberration ([Pu and Meng, 2003]) is minimal in a 90^o configuration, and also that waves scattered by smaller particles more closely resemble spherical waves. Since particle position uncertainty sets the

primary limit in the accuracy and dynamic range of *HPIV* measurements, a detailed analysis of imaging characteristics of the particles was presented, as well as advanced data processing algorithms for the scanned particle volume. With the aid of distributed parallel computing, dynamic measurements of instantaneous 3D, three-component velocity fields in a highly three-dimensional vortical flow were achieved.

The works mentioned above are some among the many examples that constitute the evolution in the utilization of different holographic configurations within the context of particle image velocimetry prior to the possibility of using digital holography with the same purpose. Once the resolution of CCD cameras enabled their use for recording digital particle holograms and extracting velocity fields from the numerically reconstructed volumes, the interest in holographic *PIV* was renewed ([Meng *et al*, 2004]), and new possibilities in data processing could be explored (for example, in the work of [Pan and Meng, 2003]), specially due to the fact that reconstruction is performed numerically, making both intensity and phase data readily available for automated analyses. Full high-resolution measurements in volumetric regions are being proved possible (e.g., [Sheng *et al*, 2008]), and depending on the experimental facilities and goals, there is room for further development.

In the next chapter, a preliminary experimental facility for testing digital in-line holograms will be presented. This setup and holograms taken from it will serve the purpose of demonstrating some of the theoretical aspects presented here.

Then, in the subsequent chapter, the side scattering configuration employed for wind tunnel measurements will be described.

III
In-line Holographic Setup for Initial Tests

This chapter presents the description of the first optical setup implemented in the context of the thesis. It is the in-line forward scattering (Gabor) setup mentioned in chapter II, and the main purpose of this preliminary setup was to begin exploring digital holographic image acquisition. No actual flow field to be measured existed in this first test setup, but it provided both ruler and particle spray images which were useful for testing and implementing initial software developments. Additionally, presenting some images from an in-line setup can be useful for illustrating some of the concepts introduced in the previous chapter.

III.1 Description of the Setup

Figure III.1 shows a scheme of the straightforward optical setup for recording in-line holograms. As the name implies, in such a setup all the optical components are lying in the same axis.

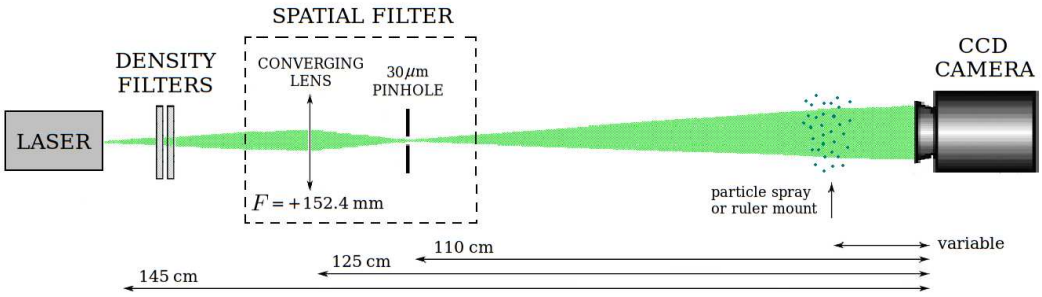

Figure III.1: In-line Gabor configuration mounted for preliminary tests.

The wavelength of the Nd:YAG laser used is $\lambda = 532$ nm, and the CCD camera sensor has 1280×1024 square pixels with lateral dimension $\Delta = 6.7$ μm. The beam was not collimated, and therefore was a diverging beam. It illuminated the object and served as reference beam simultaneously (the reason why this is possible and characterizes in-line holography was already mentioned

in chapter II — the object being a "cloud" of very small particles in air, the undiffracted portion of the light is practically undisturbed and can serve as reference).

Tests were made with thermal water spray particles with average diameter around 100 μm, estimated later from reconstruction results and calibration. These particles were sprayed through a rectangular slit, in order to bound the extension of the particle volume along the optical axis (depth) direction. Beside the spray images, some calibration images of a small ruler were registered, and for that the slit was removed and the ruler was placed on top of a support in different positions in front of the sensor.

In this configuration, light diffracted by the particles forms the object beam, while the reference beam consists of the undiffracted portion of light. The coherence length requirement in this case is practically non-existant; in general coherence must be enough to guarantee interference over all path length differences encountered, but in this case they are due only to the very small differences in spreading angles of the light scattered by the particles (or another object) and the reference wave. Without this very minimum coherence, interference would not take place and one would not be able to register the holographic information in the first place.

The energy level required to register a good quality hologram here is not very high either. Something that has to be considered regarding energy level is the fact that the CCD sensor is directly exposed to the incoming light and can be damaged permanently from overexposure. Reducing laser energy directly brings up some beam instability, so the laser built-in attenuator was used, and density filters were chosen as a means of further lowering the energy. This kind of filter absorbs a part of the energy, transmitting a beam that is attenuated by a certain ratio dependent on the filter density, without back reflections or scattering. The transmitted energy ratio T relates to the optical density of the filter by $T = 10^{-D}$, where D is the density. In this setup, two filters with 0.3 and 1.5 densities were used, resulting in a transmission ratio of $10^{-0.3}.10^{-1.5} = 1.58\%$ and a strongly attenuated beam that nevertheless provided very good quality holograms.

It can also be noted in figure III.1 that a spatial filter was inserted in the setup after the filters. Laser beams pick up intensity variations from scattering by optical defects or particles in the air, resulting in high frequency spatial noise on top of the ideal pattern. Spatial filters provide a good way to remove most of these random fluctuations from the intensity profile of the laser beam, which is always important in imaging applications, specially in coherent ones such as holography. The concept of spatial filtering is quite simple Fourier optics: an

incoming beam — which when collimated or weakly divergent behaves as if generated by a distant point source — is focused by a lens of focal length F. According to diffraction theory presented in chapter II, the image formed at the focal plane is the optical power spectrum, a "map" of the spatial frequencies present in the beam. High frequency noise will appear in an annulus centered on the optical axis, while centered right at the axis will be something close to the ideal gaussian profile. A pinhole is then put in the focal plane and blocks most of the noise. The spatial filter components used in the experiment are shown in figure III.2, as well as illustrations of a typical incoming beam profile and the image in the focal plane of the lens. The focal length of the positive lens used in the setup was $F = 152.4$ mm and the pinhole had a 30 μm diameter. If the pinhole is correctly positioned at the focal plane, a projection of the outcoming beam will clearly show the Airy pattern.

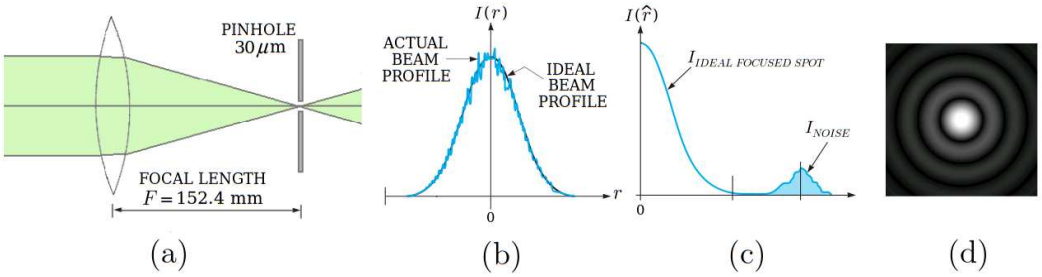

Figure III.2: Spatial filtering: (a) spatial filter components used in the present in-line experiment; (b) profile of a typical incoming beam; (c) image in the focal plane of a lens for the profile on the left; (d)*Airy pattern*: projection of the output "clean" beam when pinhole is inserted; the central spot is the *Airy disk*, with gaussian intensity profile.

Ideally, since we are dealing with coherent imaging, it is better for the optical setup to comprise as few components as possible, in order to avoid adding unnecessary interfering noise and optical aberrations. Particularly, a choice was made here not to collimate the laser beam, as the diverging beam (whose source is the spatial filter pinhole) can be faithfully represented in the numerical implementation, leading to an equally accurate reconstruction.

Another point worth mentioning about the preparation for hologram acquisition is the importance of properly cleaning the optical devices and the sensor glass cover, with the goal of reducing noise in the holographic image, since every dust in the path of the beam from the laser to the CCD will diffract light and have its interference pattern registered in the image, adding up to unwanted noise.

III.2 Results: calibration ruler and particles

Like in any other *PIV*-related experimental technique, a calibration procedure is usually recommended in order to relate image space — in this case the numerically reconstructed planes — with real space dimensions. For the in-line setup, a calibration object such as a transparent ruler with small marks can be placed, preferably at a few different z positions from the sensor, and holograms of it registered.

After numerical reconstruction at the best focal plane, the focused image serves as physical calibration for that plane. Figure III.3 shows a hologram of a small ruler and its reconstruction in the z position corresponding to the best refocusing. The reconstruction at $z \approx 11$ cm matches well the measured physical position of the ruler in relation to the sensor, although this measurement has a minor uncertainty due to the fact that the sensor lies inside the body of the camera. The ruler — which is a glass plate with 100 lines marked within a 5 mm length — was mounted on top of two connected small supporting stages with verniers, and could be positioned at different distances from the sensor. Holograms from these different positions of the ruler were also taken and reconstructed, but are not shown here.

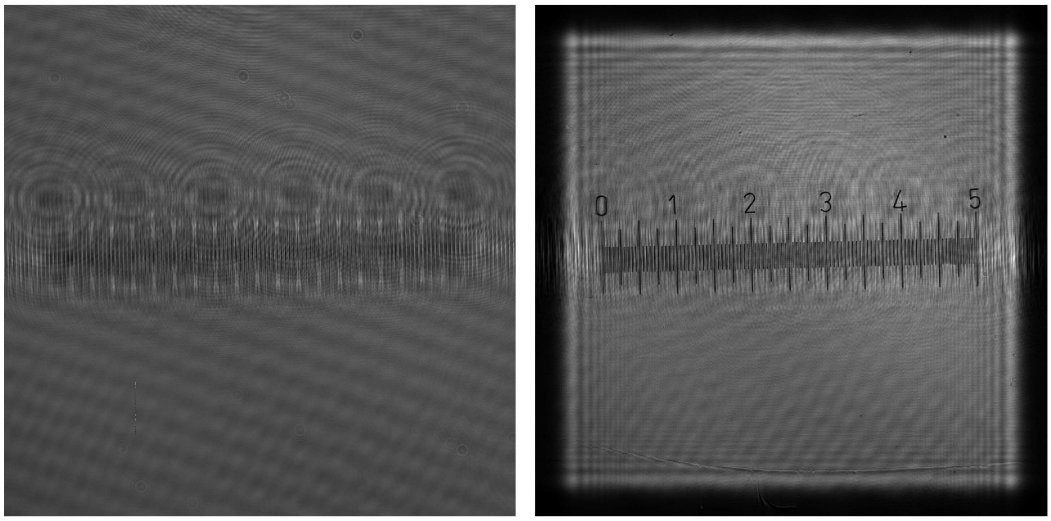

Figure III.3: Calibration ruler: hologram (left) and reconstruction in best refocusing plane (right).

In this kind of setup, and with no use of magnification lenses, the depth position recovered from reconstruction is expected to be the same as the distance from the object — in this case the ruler — to the CCD plane (see z_0 in figure II.10 from chapter II) for any depth position of the object, unless the reference beam source is not correctly represented in the numerical reconstruction. As for lateral dimensions, again one can only expect

a magnification slightly different from 1 : 1 if the non-collimated reference beam and its diverging nature are not being modelled precisely in the numerical implementation ([Goodman, 1968], [Palero *et al*, 2007]).

By modelling the reference wave as a spherical wave with known source position (the source in this case is the pinhole used in the spatial filter and its distance to the CCD plane is measured and known *a priori* with only a small uncertainty), the holographic imaging system should have 1 : 1 magnification, that is, numerical reconstruction at the refocusing plane should provide an image of the object at its original position and with no lateral magnifications, and in this case calibration should be simple and straightfoward (mostly for verification purposes), or even unnecessary. However, if source distance is for some reason hard to be evaluated and chances are reconstruction wave is not correctly represented, either calibration in different planes in the region of interest or calibration in one plane and subsequent analysis of the holographic equations presented in Appendix A (to recover the correct source position) takes care of the problem.

Measurements of number of pixels along the length of the ruler were taken from the reconstructed images, and multiplying the number of pixels by the pixel size resulted in a length that was indeed slightly different (around 5%) from the real physical corresponding dimension, which can indicate a small error in the numerical representation of the reconstruction source. In any case, according to the considerations above, the calibration itself would take care of establishing the correct relation from virtual to physical object space in the reconstructed particle volume, and that is precisely its goal.

Both calibration and spray holograms provided an input for the initial development and testing of our own software, *HPIVlml*. All the results presented here correspond to reconstruction obtained with *HPIVlml* software. Figure III.4 shows a hologram of a cloud of particles and the corresponding reconstruction at one z plane, where several of the particles appear in focus or *quasi*-focus, while others either have gone through focusing and have their wavefronts already defocusing again or have not yet reached focus. It is also interesting to observe in the particle images that are in or very close to focus the noticeable "halo", that is, the out-of-focus twin image which appears as a fading light circle around the particle image. They are, as expected for in-line holograms and mentioned in chapter II, centered on the same axis.

Figure III.5 also shows a hologram of spray particle images — only now cropped around only two particles and enlarged for visualization — and reconstructions at two different planes corresponding to their estimated focus

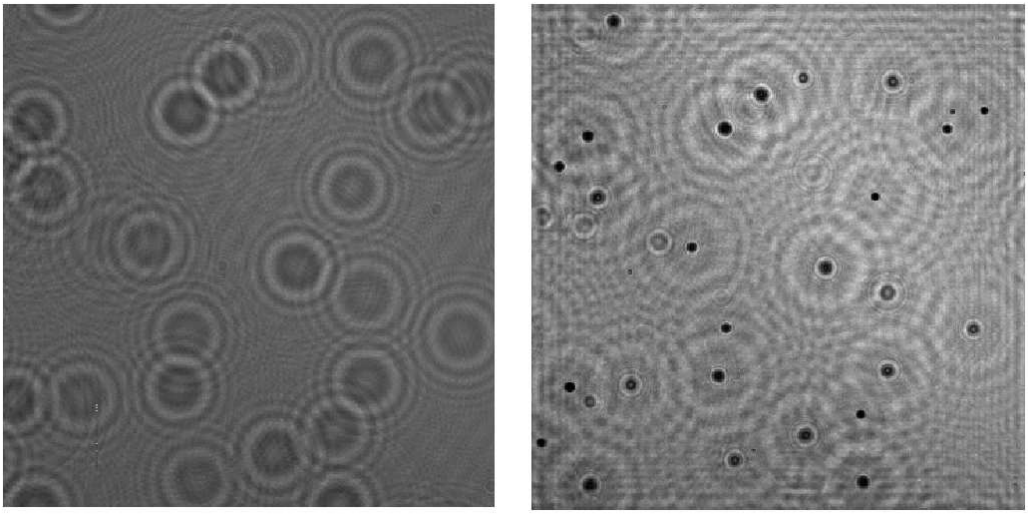

Figure III.4: Hologram (left) and reconstruction of a cloud of particles at $z = 11.5$ cm (right).

positions.

Figure III.6 presents the intensity iso-contour of a single particle, corresponding to 75% of its peak intensity, and serves as a good illustration of the previously mentioned depth-of-focus issue, as it noticeably shows that the particle image has a significant elongation in depth.

Post-processing techniques were then explored in the volume constituted by the adjacent, closely-spaced reconstructed planes, with the main goal of finding the optimal algorithm of focal plane particle detection for the in-line case. Most recent research works use estimations based on the centroid of the particle 3D image obtained from connecting 2D image sections after intensity thresholding, but other criteria can be used.

Figure III.7 shows the spatial gradient field of a given reconstructed intensity plane, the same from figure III.4. The edges become sharper when the focal plane of the particles is approached, and this is more easily identified through a quantification of such spatial gradient image, providing another criterion.

Figures III.8 and III.9 show normalized intensity and gradient color images of the plane-by-plane depth evolution of a single particle, providing a good visualization of the behavior of the refocusing process.

In figure III.10, a series of adjacent reconstructed planes for the same particle is presented, but only around the region of focus, with smaller spacing between planes. At the top row, small images framed around the particle

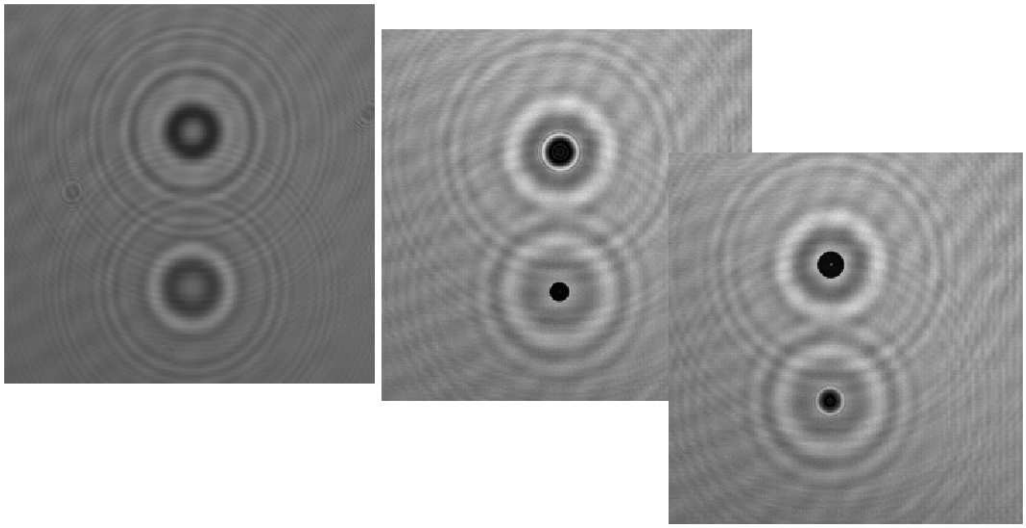

Figure III.5: Hologram (left) and numerical refocusing of two spray particles, one at $z = 11.5$ cm (middle) and the other at $z = 11.8$ cm (right).

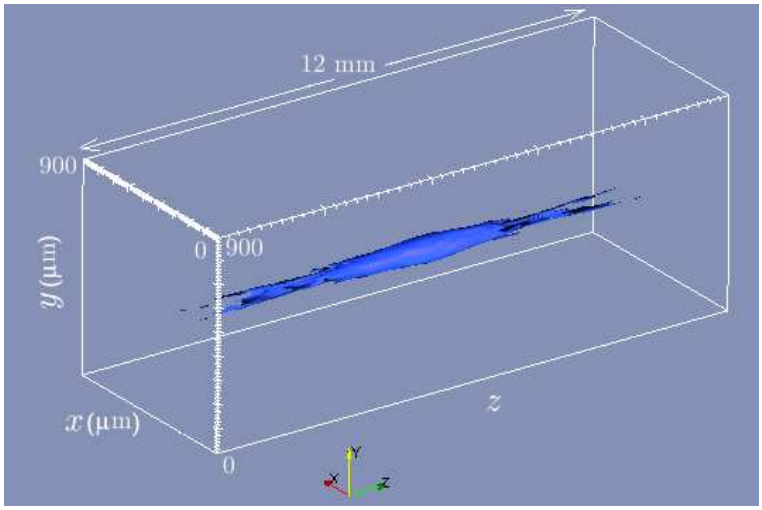

Figure III.6: Iso-contour of a single particle at 75% of the maximum intensity: the elongation in depth is noticeable.

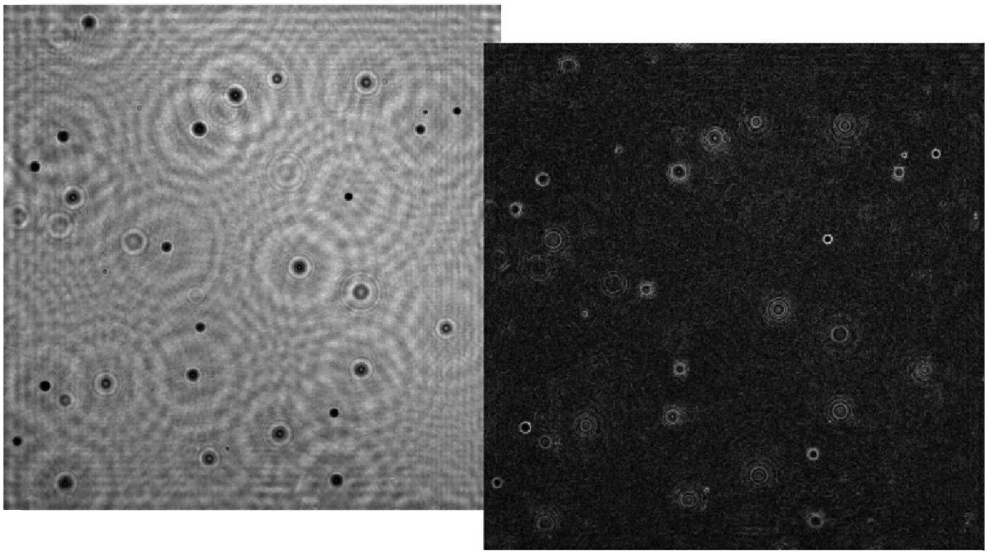

Figure III.7: Reconstructed intensity image (left) and corresponding spatial gradient distribution (right) at $z = 11.5$ cm.

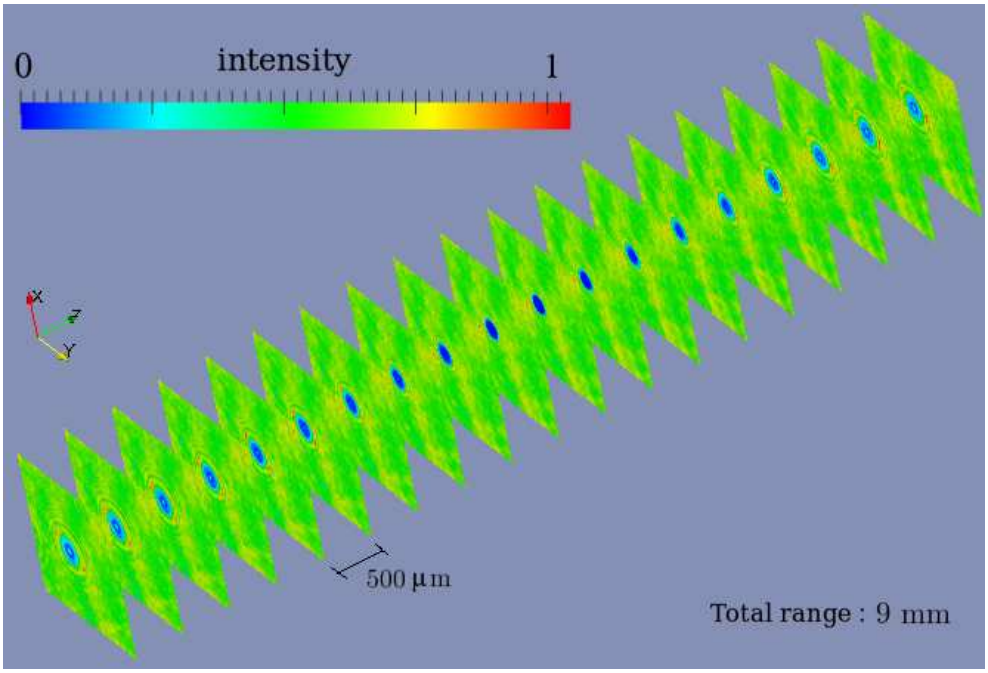

Figure III.8: Depth evolution for a single particle: normalized intensity color contours.

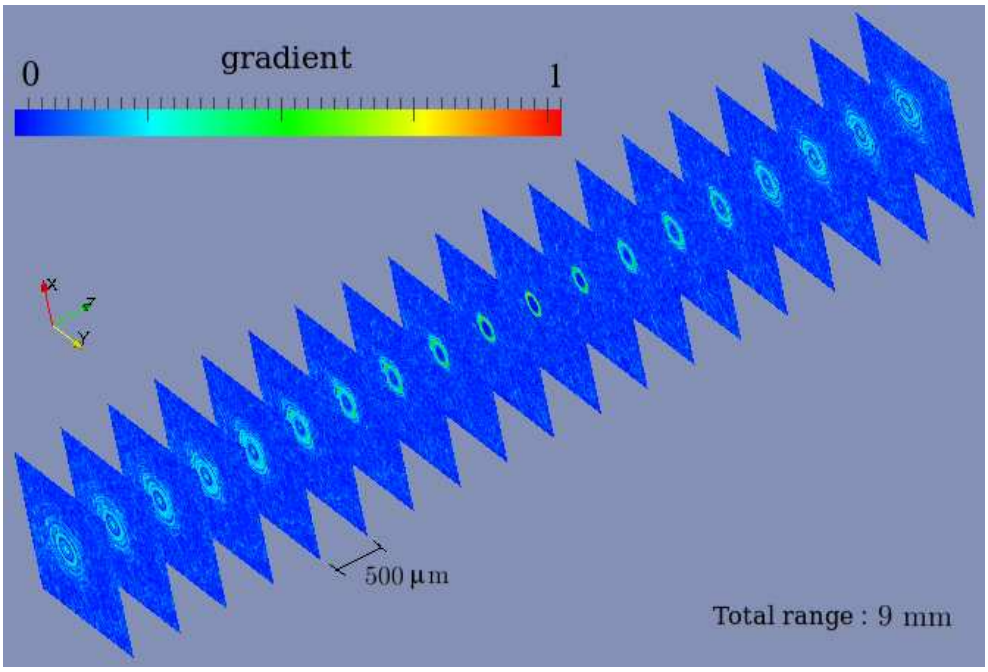

Figure III.9: Depth evolution for a single particle: normalized gradient color contours.

taken from intensity images, and at the bottom row, the corresponding ones taken from intensity gradient images. Based on the criterion of maximizing the average intensity of the cropped gradient image around the particle, the position corresponding to the center of figure III.10 was chosen as the best focus, but the axial resolution problem can also be observed here, from the fact that several images around it have pretty much the same sharpness. Plots of this gradient criterion as a function of depth reconstruction position showed that particle position estimation was inside an uncertainty region extending in depth on average around 700 μm, or 7 times the mean particle diameter (diameter being measured in the plane corresponding to the middle of this region).

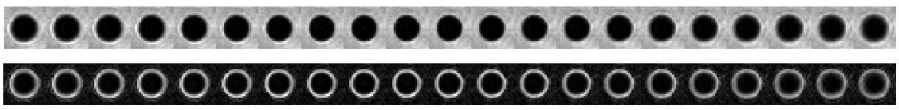

Figure III.10: Depth evolution for a single particle. Top: intensity field; Bottom: gradient field. z spacing between planes is 50 μm.

Another option for estimating focus depth position would be to minimize the intensity fluctuation in the region around the particle images. In the work of [Palero *et al*, 2007], that is done for micro-droplet images by calculating the fluctuation as the standard deviation of the intensity.

In [Pan and Meng, 2003], an improvement in particle axial location for

forward scattering systems with planar reference is proposed by means of exploring the complex amplitude information in the reconstructed volume, which is uniquely available in digital holography. A complex particle "signature"is introduced, and this serves as a criterion for both particle validation (verifying that a high intensity region separated in the thresholding step is indeed a particle, differentiating it from speckle noise) and focus position extraction. The authors deduced that the imaginary portion of the complex reconstructed wave tends to zero as an isolated particle comes into focus. But because of the presence of other particles in a dense particle field, the imaginary part $\Im(U)$ does not go to zero. So, they examined the variance of $\Im(U)$ for a particle P_j,

$$\sigma_U{}^2 = \sigma_{r_j}{}^2 + \sigma_{\Omega_j}{}^2, \tag{III.2.1}$$

where σ^2 represents the variance of the imaginary part of the complex amplitude. The index r_j represents the contribution of the real image wave (as opposed to the virtual image wavefront) for that specific particle, and Ω_j represents all the other contributions (the virtual image wave of that particle plus the "noise" from all the other particles). The variance is defined in a transverse plane for all pixels that belong to the image of particle P_j in that plane. Scanning through a series of adjacent planes around the focus position, and plotting imaginary variance against z creates a curve with a dipping shape with its minimum at the particle in-focus position. The absence of this dipping characteristic would indicate that the region being analyzed does not contain a particle. In the present test case, based on the reconstruction results and calibaration from the ruler, the estimation of the average spray particle size was about 100 μm, and differentiating particle from noise in the reconstructed planes was not a problem.

A microscope objective was also used for magnifying the holographic pattern to be recorded. Accordingly, a magnified object is reconstructed, as shown in figure III.11 with a hologram of the calibration ruler and its reconstruction at the best focus. Reconstructed image comprised 1.25 mm, corresponding to a magnification of 5.5. Use of the objective can enable improvements in lateral and axial resolution of the particle field images. This calibration procedure accounts for correction to real coordinates.

In the more complicated setup implemented in the wind tunnel, which will be described in the next chapter, a miscroscope objective is used to magnify the object field generated by the particles present in a small measurement volume within the tunnel. This is why a microscope objective was employed here as a first test. However, as will be seen, the objective in the tunnel con-

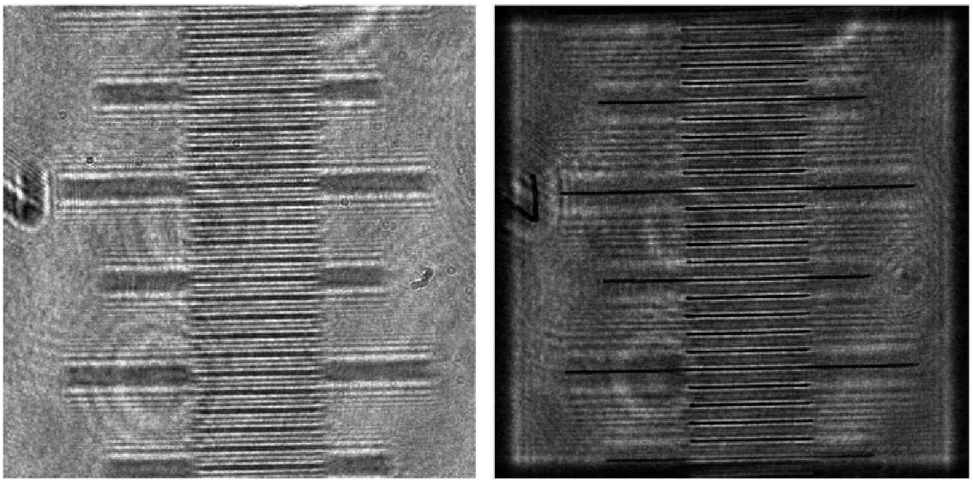

Figure III.11: Using an objective lens for magnification. Hologram (left) and reconstructed image (right).

figuration is used to magnify the object field alone, and not the hologram, which constitutes an important distinction in relation to previous configurations found in the literature.

Final considerations One of the major drawbacks of this configuration, which was previously mentioned in chapter II, is the so called "depth of focus" problem, that is, the size of the reconstructed particle image along the optical axis is several times its real size, elongating it to the spatial resolution δ_z along the depth direction and thus making determination of the refocusing position more difficult and less accurate. What is found is an ellipsoidal form whose peak intensity is a z range rather than a unique z position. Although this focusing problem is indeed quite relevant and prevents the application of the technique in a high particle concentration, the setup requires minimum optical equipment and laser coherence length. All of these considerations could be observed in this preliminary experiment.

IV
Specific Setup for Wind Tunnel Measurements

With the main goal of performing boundary layer velocity and wall shear stress measurements in the large wind tunnel facility of LML, a holographic *PIV* setup in a particular configuration was mounted, tested and implemented. Details of this configuration will be explained next. A microscope objective lens was introduced to magnify the object wave coming from the particularly small measurement volume (~ 1.5 mm^3), which increases recording resolution of the interference patterns and improves accuracy in particle location.

First, a brief section describing the LML wind tunnel and its characteristics and settings during the time of this thesis experiments is presented. Then, in the subsequent section, the optical setup implemented in the side-scattering holographic configuration is described, along with explanations concerning some preliminary side tests and adjustments. Finally, in section IV.3, the calibration procedure is thoroughly delineated, with all the equations involved.

IV.1 The Wind Tunnel Facility

The holographic setup developed in the context of this thesis was initially tested and employed with the aim of making velocity measurements in the LML wind tunnel facility. Thus, a short description of the tunnel is presented here, preceding the description of the actual holographic setup in the next section.

The tunnel's main characteristics and dimensions are depicted in figure IV.1. The overall length is about 20 m, with the last 5 m providing optical access from all sides, which allows flexibility for different experiments and optical arrangements. The cross-section is 1×2 m^2, and the free stream velocity ranges from 1 to 10 m/s, regulated with $\pm 0.5\%$. The tunnel can be operated in closed loop with temperature control or open to the outside.

The boundary layer (the abbreviation BL might be used sometimes, from now on) that develops on the lower wall is tripped at the entrance of

the tunnel by a grid laid on the floor, and a large boundary layer thickness can be achieved, which allows for very good spatial resolution to be obtained in velocity measurements. For a more detailed description of the facility, see [Carlier and Stanilas, 2005], in which the authors reported *PIV* measurements in this boundary layer.

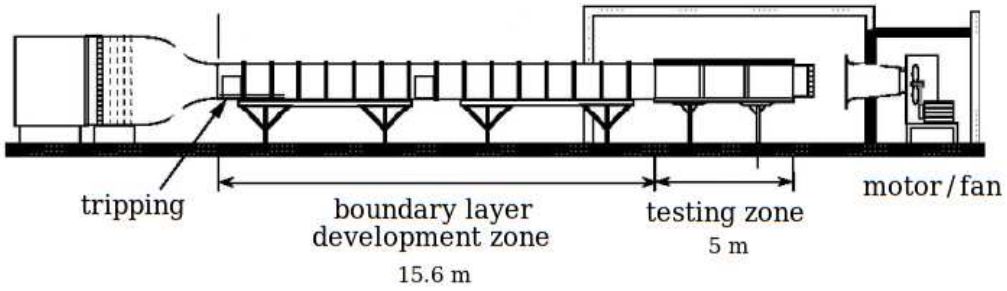

Figure IV.1: Turbulent boundary layer wind tunnel at LML.

During the period when the holographic *PIV* experiments described in this thesis were being performed, the tunnel configuration was modified for subsequent experiments carried out by other researchers in the laboratory ([Cuvier *et al*, 2011]), involving the study of adverse pressure gradient flow, separation, and flow control. These experiments aimed at characterizing the flow over a two-dimensional ramp, and developing an adjustable model that could allow modification of the turbulent boundary layer state before separation. Because of the large thickness δ provided by the tunnel configuration, detailed analyses of the influence of the BL state on flow control parameters and effectiveness could be performed. In the context of this flow control project, visualization tools were used to characterize the separation, wall taps were placed to evaluate pressure distribution on the ramp, and velocity measurements were performed using a single hot-wire (with uncertainty in the mean velocity estimated around $\pm 1\%$). Average wall shear stress was evaluated for the different configurations. In fact, some velocity and wall shear stress measurements from this work can serve as a comparison for the holographic *PIV* experiments, although hot-wire measurement points are not available for $y^+ < 5$.

The *bump* model was mounted in the wind tunnel lower wall, and its design is schematically shown in figure IV.2. The model is divided into four parts. The first is a smooth converging section with a contraction ratio of 0.75, aimed at enabling the generation of an adverse pressure gradient downstream, and also allows suction through a porous slot. The second section is an articulated flat plate used to tune the pressure gradient, and could be rotated from 2 to -4 degrees around its leading edge (for negative values of α

adverse pressure gradient conditions occur). The third part is an articulated *flap* designed to control separation when it exists, and by decreasing β the adverse pressure gradient is increased. Lastly, the fourth part is a flexible plate that provides a smooth connection between the flap and the tunnel floor.

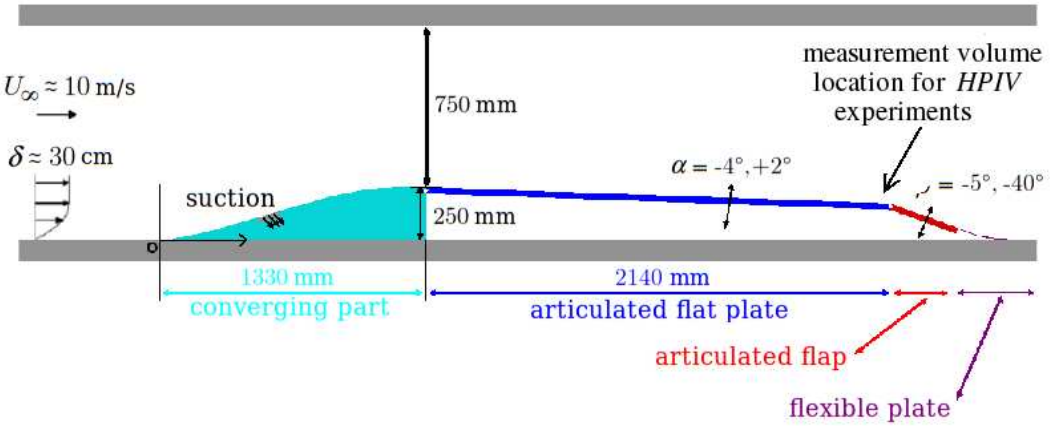

Figure IV.2: Schematic view of the tunnel configuration during the period of the holographic experiments of this thesis. A *bump* model was mounted for a different project ([Cuvier *et al*, 2011]).

Figure IV.3: Photo of the measurement section. The bump model mounted for turbulent boundary layer control can be observed.

Figure IV.3 shows a photo taken at the measurement section of the wind tunnel, where the bump configuration can be seen. Due to logistic reasons, the experiments from this thesis had to be carried out during a period when the bump model was mounted, and the configuration set to $\alpha = -2^o$ and $\beta = -22^o$. These were the parameters used for the hot-wire measurements in the flow control experiments.

Now that the wind tunnel facility was described in the configuration it was set to during the holographic measurements, the holographic setup itself can be described next.

IV.2 The Side Scattering Holographic Setup

In a large facility such as a wind tunnel, where seeding particles are spread all over the flow, the in-line Gabor configuration tested in chapter III cannot be used. This is so because the beam would have to pass through the whole lateral or vertical dimension of the tunnel and, consequently, through a large volume of particles. Since the basic hypothesis in the Gabor configuration is that the beam passes nearly undisturbed and can also serve as the reference beam, it is not feasible to use this configuration in a large seeded facility. Thus, a different optical setup has to be implemented. The solution found is shown schematically in figure IV.4. In this representation, the flow direction is normal to the figure, towards the viewer.

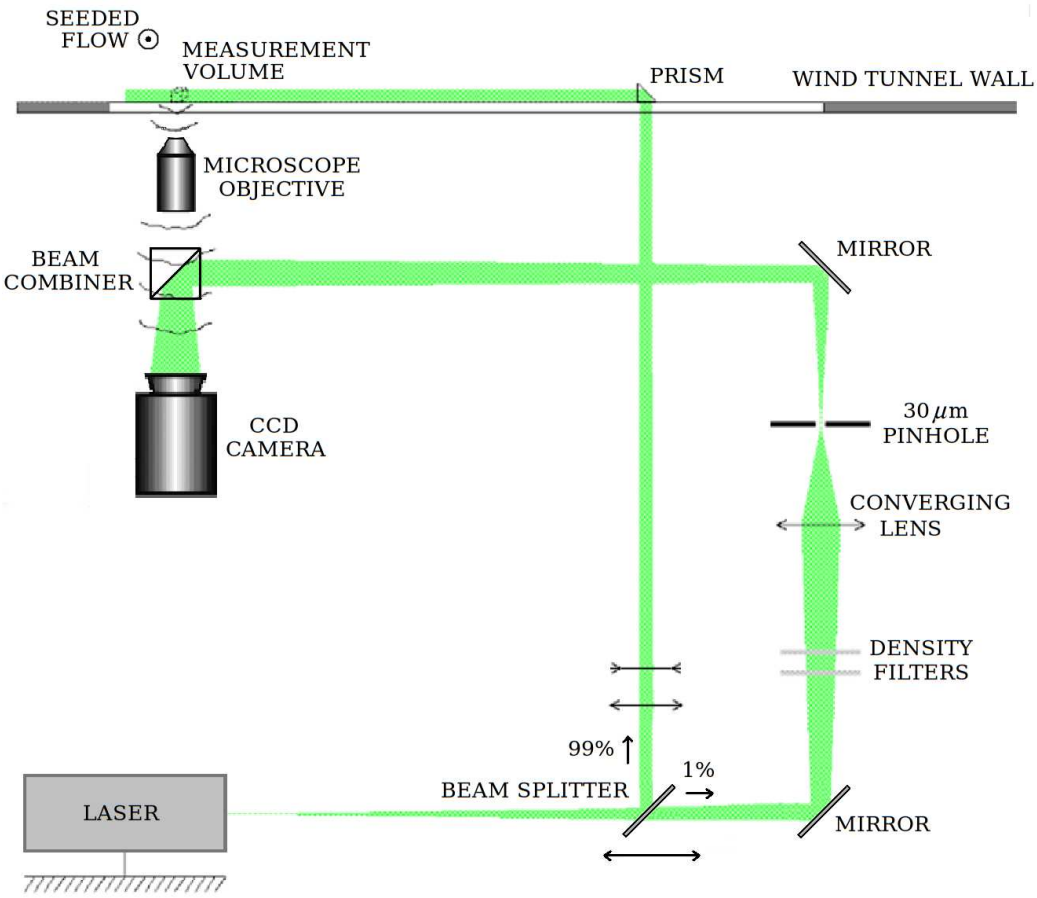

Figure IV.4: Optical configuration: in-line side scattering setup for the wind tunnel. A microscope objective lens is introduced to magnify the object beam.

In this setup, two separate beams are used for illumination and reference. The light beam coming from the laser encounters a special 99/1 energy ratio beam splitter (high-energy plate beam splitter to be used at 45^o angle) that separates the beam in two, at a right angle to each other. It is positioned so that the reflected part ($\sim 99\%$) is directed upwards and the transmitted beam ($\sim 1\%$) goes on in the horizontal path.

The lower-energy transmitted beam, which will provide the reference, hits a mirror placed at 45^o and is directed upwards, passing through further attenuation by a set of neutral density filters (three filters with different optical densities were available — 0.3, 1.0 and 1.5 — and depending on the need of the object/reference energy balance tuning, a different combination could be mounted) and through the spatial filter described in the last chapter. The beam then hits another mirror and is directed horizontally to a cube beam combiner placed carefully at a known distance above the camera and centered on its axis.

Meanwhile, going back to the other arm, the beam that leaves the first beam splitter going up carrying most of the energy (99%) serves as object illumination. The reason for using 99% of the original laser energy is that the particles will be illuminated and then scatter at 90^o, which is much weaker than foward scattering. The beam hits orthogonally a small prism positioned inside the tunnel (mounted inside an aerodinamically-shaped piece which is not shown in figure IV.4) and goes on to illuminate a measurement volume of around 1.5 mm^3 located in the tunnel spanwise mid-section.

Also, in the upward path of this object arm, there is the possibility of using long focal converging or diverging lenses in order to finely control, if necessary, the beam diameter and consequently the size of the measurement volume.

In this way, particles close to the wall in the region of interest are illuminated and scatter light at 90^o. The scattered light constitutes the object wave, and goes through a microscope objective lens with nominal magnification of 10 times and focal distance $f = 20$ mm. The *magnified object wave* is then transmitted through the beam combiner and combined on-axis (the exact same axis of the objective lens and the camera) with the reference wave coming from the other arm.

Finally, reference and magnified object waves interfere and this interference pattern — the hologram — is registered on a camera CCD sensor with 1376×1040 square pixels with size $\Delta = 6.45$ μm.

Such an optical setup takes advantage of the speckle noise reduction provided by the side-scattering and the lower resolution requirement provided by the in-line recording (see "The sampling theorem" in section II.4, chapter II) — smaller angles between interfering beams generate larger fringes that can be better resolved for the same sensor resolution. Also, this configuration provides a better control of the measurement volume position and dimensions, as well as a "clean" reference beam that can be adjusted separately for optimization of the object-to-reference intensity ratio.

The weaker side scattering can be partially compensated by this possibility of adjusting the intensity ratio, which can drastically improve the constrast of the holograms. Ideally, a 1 : 1 ratio should be used to provide optimal fringe contrast[1]. In the setup shown in figure IV.4, the set of density filters can also be modified to achieve optimal conditions. The long-distance lenses available for use at different positions in the vertical object arm, and aimed primarily at controlling measurement volume size, also affect the energy density in the beam that illuminates the measurement volume. All these components and their interchangeability provide the necessary flexibility for fine-tuning and optimization of the imaging system as a whole.

The optical components were all mounted on structural aluminium profiles with the aid of appropriated optical supports, as shown in the schematic drawing of figure IV.5. In figure IV.6 the left and right-most structural profiles are represented in more detail.

On the left, the vertical profile supporting the microscope objective lens, the beam combiner and the camera is represented. All the components were leveled and correctly fixed with the aid of a quality level meter, and then they were centered on the vertical axis that passes through the camera sensor center. The camera — component that "dictated" the centering axis — was mounted on top of a translation stage allowing vertical movement. To do all the alignment, the laser beam itself was also used, and a back-reflection verification procedure was performed. The objective lens was fixed in a simple centering optical mount on top of a translation stage in the vertical direction, and could be moved in all directions, both to center the lens correctly and move it up or downwards depending on parameters that will be discussed later, related to details of the imaging system. The beam combiner was fixed in a special

[1]In practice this may not be so, due to CCD linearity issues. In digital cameras employing charge-coupled device (CCD) sensors, the fundamental function of the CCD is to convert photons carrying image information into an electronic signal. After digitization, the signal output should ideally be linearly proportional to the amount of light incident on the sensor. Although these sensors respond in a linear manner over a wide dynamic range, depending on the average intensity, a non-linear response can be observed.

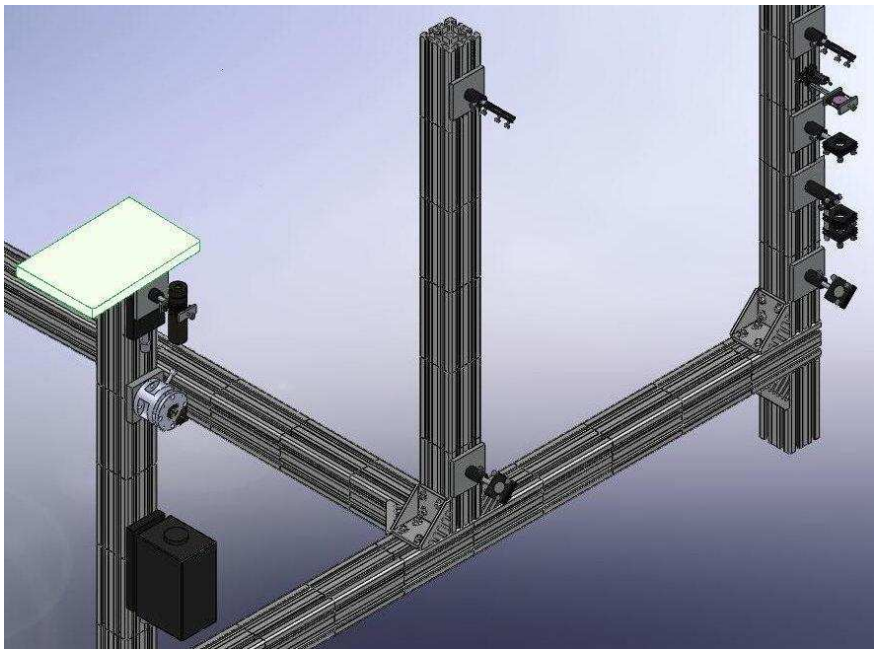

Figure IV.5: Optical setup structure with glass plate simulating tunnel wall for tests on the side. After alignment procedures and different tests, the plate was removed and the structure brought to its position below the wind tunnel for realignment, holographic calibration procedure and flow-on hologram recording.

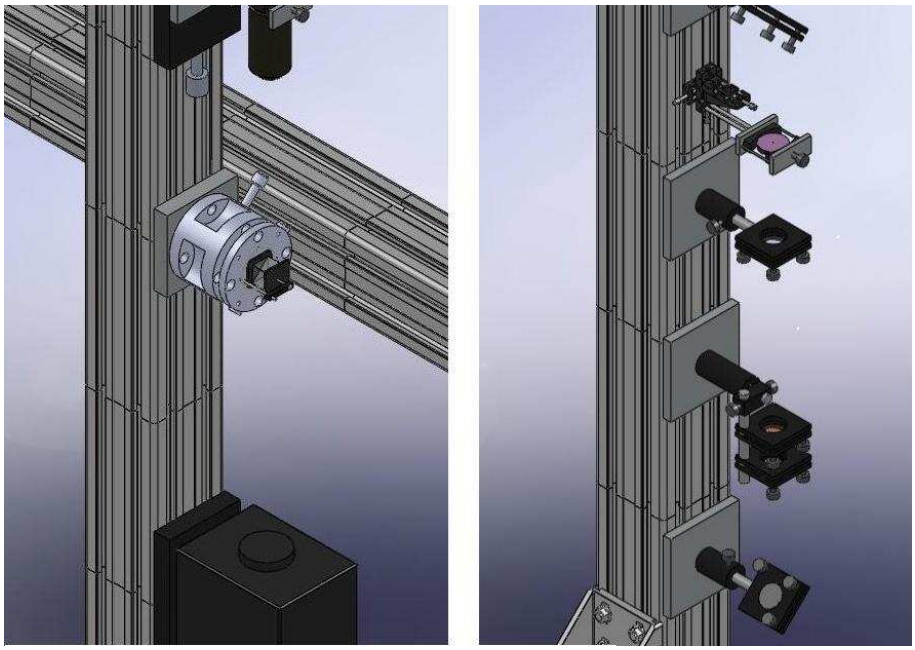

Figure IV.6: Detail of two of the vertical structural profiles in the optical setup.

3D mount, with precise angle adjustment for leveling and with flexibility for positioning and centering.

On the right side of figure IV.6, the detail of the components through which the reference beam passes before being directed towards recombination with the object wave is shown. Bottom up, the components represented are a mirror, the mounts for density filters, the converging lens and the pinhole that constitute the spatial filter, and the mirror that turns the reference path at 90^o towards the beam combiner. In order to be able to place the pinhole at the height corresponding to the focal plane of the lens (152.4 mm) and correctly center it so that it was aligned with the axis of the beam, an ensemble of three small translation stages was used, which allowed precise positioning.

Side tests With the optical setup base structure shown in figures IV.5 and IV.6 positioned away from the wind tunnel (for more space and ease of access), side test procedures were performed in order to make preliminary arrangement choices, try different possibilities in terms of components positioning and insertion of extra devices if necessary, accurately align optical components on the axis of the beams paths, choose the best calibration procedure, and so on. For that, a glass plate was placed on top of the left vertical profile, simulating the tunnel wall, as seen in figure IV.5. On top of this plate, either particles (water spray, a small Laskin nozzle that generated aerosol particles, and a plastic cube with particles inside are examples of what was employed for different tests) or candidates for calibration objects were placed.

In this configuration, laser coherence is extremely important, and the coherence length of the laser has to be at least as large as the path difference between object and reference beams, since they are expected to interfere after recombination. Because of that, coherence length tests were performed to evaluate laser functioning in unseeded and seeded modes, as a part of these side experiments as well. A scheme of the setup for coherence length measurement is shown in figure IV.7. Because of the difficulty in achieving any discernible interference fringes in the images even with magnification, it was concluded that the coherence length of the laser without any seeding was even smaller than previously expected, and that seeding the laser was indeed necessary.

The laser used in the experiments described in this chapter was a customized one with four 300 mJ cavities, and an injection seeder. In the seeded mode that had to be activated, the output of a small *seed* laser is directed into the main laser cavity to stabilize its output. Most seed lasers are stable, single-frequency lasers, which encourage the larger laser to lase in

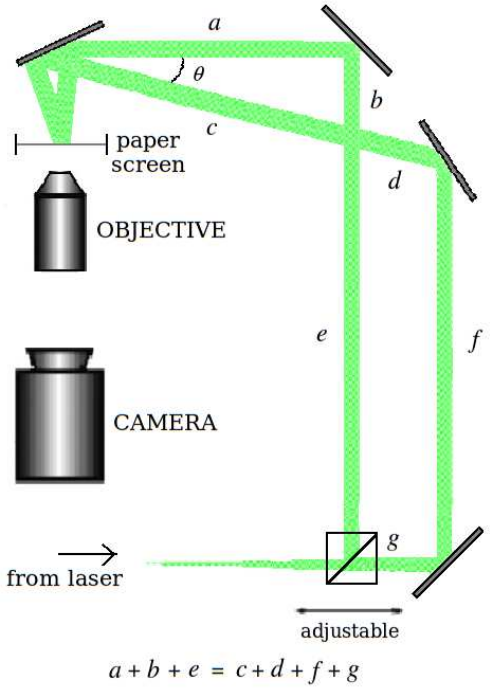

Figure IV.7: Setup for coherence length measurements.

a single longitudinal mode and improve laser coherence by a great amount. For this experiment, it was estimated that the seeded output coherence length was about 2 m, which was enough to provide conditions for the wind tunnel holograms to be successfully recorded.

Final Adjustments Following the side tests mentioned above, the optical setup from figure IV.5 was moved to its final position below the wind tunnel, and some final adjustments were made before calibration and measurement procedures. Some photos of the setup in measurement position are shown in figures IV.8, IV.9, and IV.10.

Before starting to acquire holograms, of course, a new series of verifications and alignment processes had to take place. As the final goal was to make three-dimensional PIV/PTV measurements employing this setup, two laser outputs had to be used. The two outputs pulse successively, but with a delay Δt, chosen by the user as the best time between frames for PIV measurements. Figure IV.11 shows the manner in which both beDigital holography for micro-droplet diagnosticsam outputs were combined and aligned for the wind tunnel measurements, since this detail was not represented in figure IV.4.

Laser outputs 1 and 2 were carefully directed to the same axis through a series of adjustments. Each one is supposed to pulse at different times, but they should have their paths exactly coincident, so that both hit the optical components at the same central locations and follow as precisely as possible

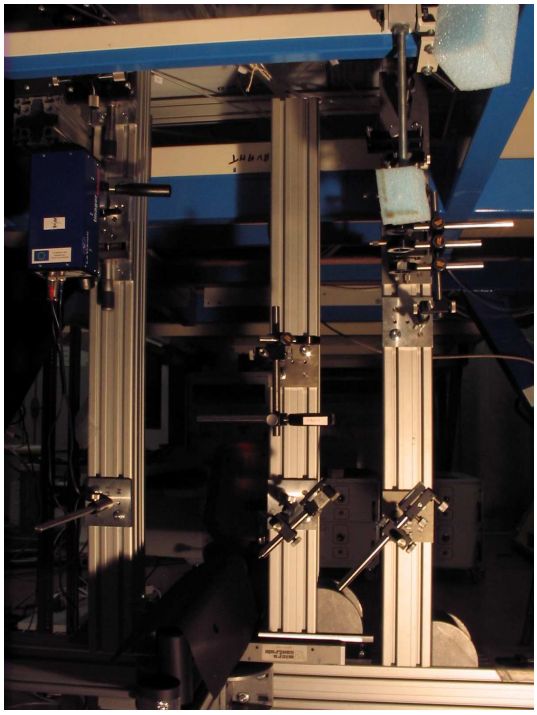

Figure IV.8: Photograph of the optical setup placed below the measurement station of the LML wind tunnel. Beam combiner and microscope objective cannot be seen properly because they are "hidden" behind a part of the tunnel structure.

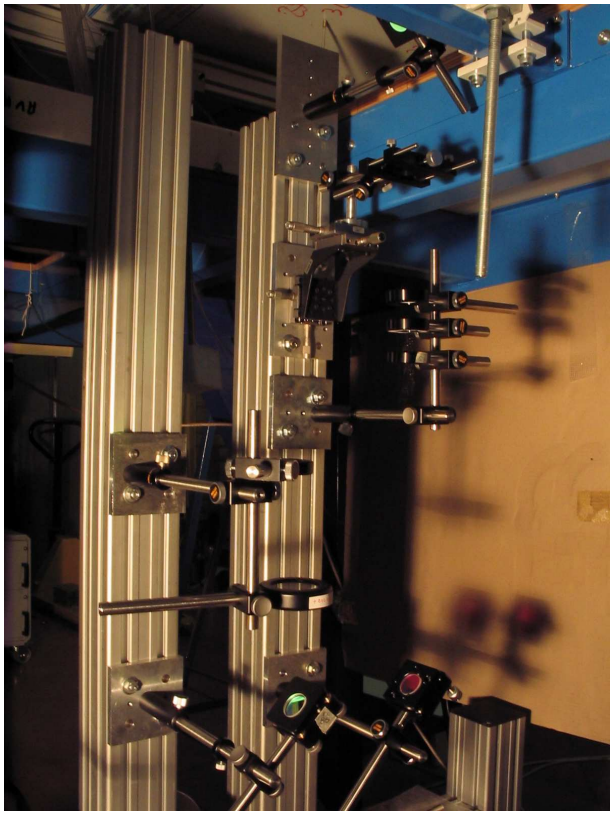

Figure IV.9: Details of the optical setup. Right side arm comprises mirrors, density filters, and spatial filter.

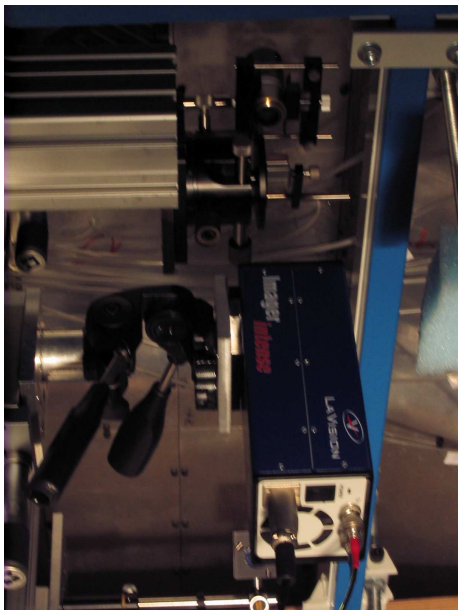

Figure IV.10: Detail of objective, beam combiner and camera positioning. All these components were mounted in stages that provided freedom for precise alignment.

the same paths through the mirrors, splitters, filters and pinhole, therefore illuminating the object in the same way and providing equivalent reference illumination for *PIV* frames 1 and 2. This is extremely important, because holograms should have the same quality so that later retrieval of particles in the reconstructed volumes from frames 1 and 2 can be equivalent and equally successful.

An efficient way to provide equal alignment for both beams at first was to check if they were both passing through the spatial filter pinhole and forming an Airy pattern with optimal and symmetrical fringe contrast afterwards. Also, by blocking the object beam, the camera images being displayed live by the computer could show the quality and characteristics of the reference wavefront image at the CCD plane for each frame individually.

There were two $\lambda/2$ plates placed next to the laser outputs, one for each beam, and by moving the 360^o pins on their supports, it was possible to tune the energies for each frame by looking to the image in the computer screen. That provided an additional way of finely compensating possible energy level differences between beams 1 and 2. Mirror and plate beam splitter (which allowed beam 1 to "pass" and beam 2 to be directed orthogonally) could be finely tuned as well, for correcting the directioning with angle adjustment. The laser and the re-directing optical components can also be seen in the photo of figure IV.12. Additionally, divergence tests for each beam were performed separately with the aid of special marker papers.

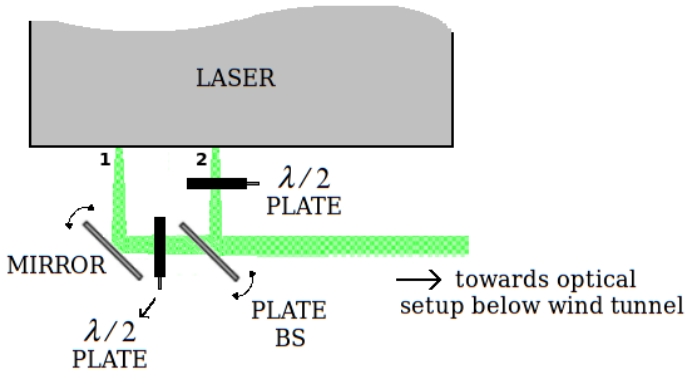

Figure IV.11: Optical components employed in the laser output re-direction for the experiments.

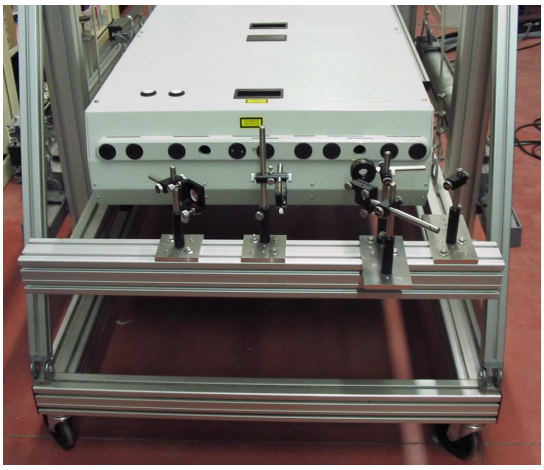

Figure IV.12: Photo of the laser and re-directing optical components.

IV.3 Calibration procedure

In the proposed configuration, specially since a strong magnification lens is being used, a proper calibration is of utmost importance. It is this calibration that will allow the particle images detected in the reconstructed volume to be correctly traced back to their respective original positions within the measurement volume located in the wind tunnel.

The light scattered from the particles inside the tunnel is magnified by the set of lens within the microscope objective, and this effect can be modeled by a single lens equation as will be presented in this section.

Every plane on the *object side* of the objective is imaged on the *image side*, past the objective, at varying distances. Also, each of these image planes has a different magnification, that is, magnification changes significantly along the optical axis.

This magnified wavefront then goes through another process that is the

holographic imaging (which in fact could result in an extra depth variation of transversal magnification as well, but here since it will be attempted to represent the reconstruction wave as a proper replica of the diverging reference wave in numerical reconstruction, a 1 : 1 magnification in the holographic imaging process will be assumed). Different planes at different distances in front of the CCD sensor will be reconstructed numerically at different reconstruction distances on the other side of the sensor. And each of those reconstruction planes needs to be properly related to the real-volume dimensions of the corresponding plane in the measurement volume, as this relation will also vary with depth reconstruction direction. This is shown schematically in figure IV.13, in which dimensions are not exact, for understanding purposes only.

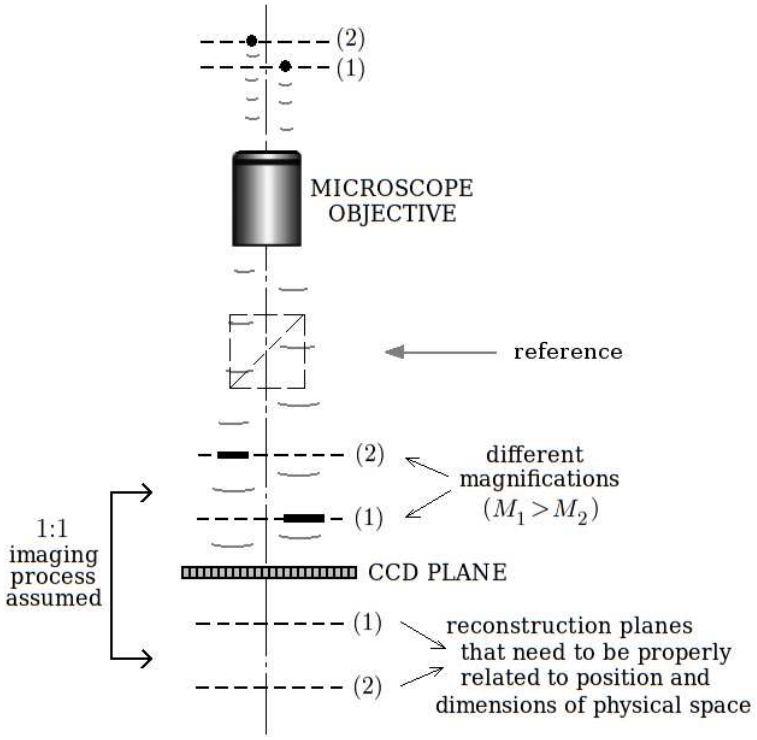

Figure IV.13: Scheme of imaging planes for a volume with two particles.

For this experimental setup, proper calibration imposed a bit of a challenge. As part of the side tests mentioned before, different objects and illumination schemes were used in attempts to record good quality calibration holograms that could be reconstructed without problems. In every case, different effects prevented interference from taking place, and reconstruction from the registered holograms was not satisfactory. The final decision was to use a very small pinhole as calibration object.

After positioning the whole structure under the wind tunnel and making

all the necessary realignments, the final calibration procedure was then performed. The slightly modified setup for this procedure is represented in figure IV.14.

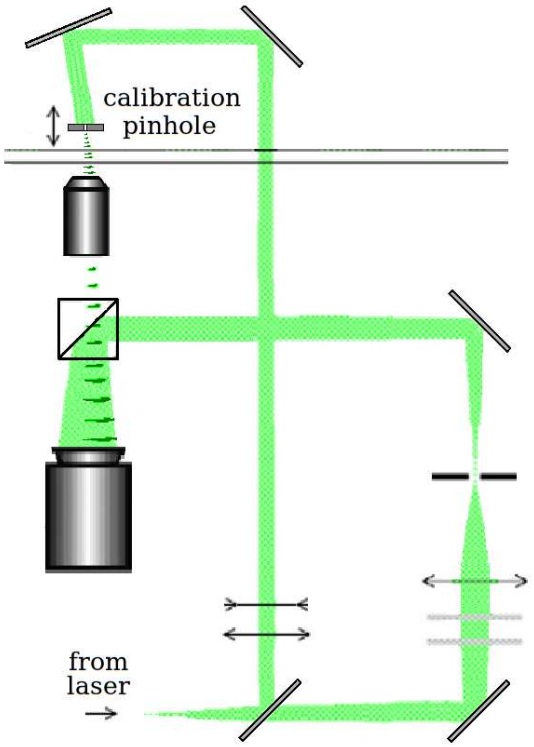

Figure IV.14: Scheme of the setup for final calibration procedure.

Once all the alignments had been made, calibration holograms of the pinhole were taken as in figure IV.14. Two pinholes were used, with 5 μm and 20 μm diameters, and holograms of them were registered in a range of positions. They were moved in the tunnel wall-normal direction with a special micro-vernier mount. Positions ranged from about 0.3 mm to 1.3 mm from the tunnel wall, with 0.1 mm steps. Although the 0.1 mm steps could be made with good accuracy, precise estimation of the absolute distance from the pinhole to the wall was not possible, because of the way it was mounted on the support and the very small dimensions involved. As will become clear, knowledge of the steps between different wall-normal pinhole positions was sufficient for proper calibration equationing.

The tunnel glass wall is 15 mm thick, optically equivalent to about 10 mm if a refractive index of 1.5 is assumed for the glass. The top edge of the objective lens was positioned at 12 mm from the bottom of the glass wall, and the estimated CCD sensor plane was approximately at a 260 mm distance from the bottom wall. These distances are reported here to give an idea of

the relative positioning of the optical components in the setup, but are not actually used in the formal calibration equationing.

The path from the reference beam source (the spatial filter pinhole) to the CCD sensor was estimated to be $|Z_R| = 77.5$ cm, and this information was later used as input in the reconstruction software for correct reconstruction wave representation — reminding that a $1:1$ holographic imaging process is assumed and this is true only if $|Z_{R'}| = |Z_R|$. Uncertainty in this measurement of Z_R was estimated to be ± 2 cm. Of course, optical axes of reference wave and modeled reconstruction wave should also coincide (they should be equally centered), and this assumption will be made as well.

All of the registered calibration holograms were then reconstructed with the *HPIVlml* software and their best refocusing depth positions evaluated by a proper algorithm, through a process similar to the one which will be described in the next chapter for particle holograms, although the position-finding algorithms are different. Figure IV.15 shows reconstructions in four different planes towards refocusing, chosen for illustration. The double images that can be observed in reconstruction planes are due to the fact that the pinhole was illuminated with an angle during recording of the calibration holograms. Another typical pinhole image, with higher zoom, is shown in IV.16, and non-symmetrical fringes can be noticed even when pinhole is focused.

The positions of the inner lenses of the objective are not known exactly, and the calibration procedure aims at establishing the correct, final equations for relating reconstructed volume with real volume physical dimensions, as a function of depth position. This involves the lens equation and the holographic reconstruction equations (simplified by the $1:1$ holographic imaging assumption) as well.

The final calibration equations — later implemented in the software for calculating the *real volume* positions of the particles retrieved by reconstruction — thus depend on d_i and d_o, parameters that describe the positions of the inner lenses of the objective. The pinhole holograms and their recovered in-focus reconstruction positions served to evaluate these parameters through calculations that will be described next.

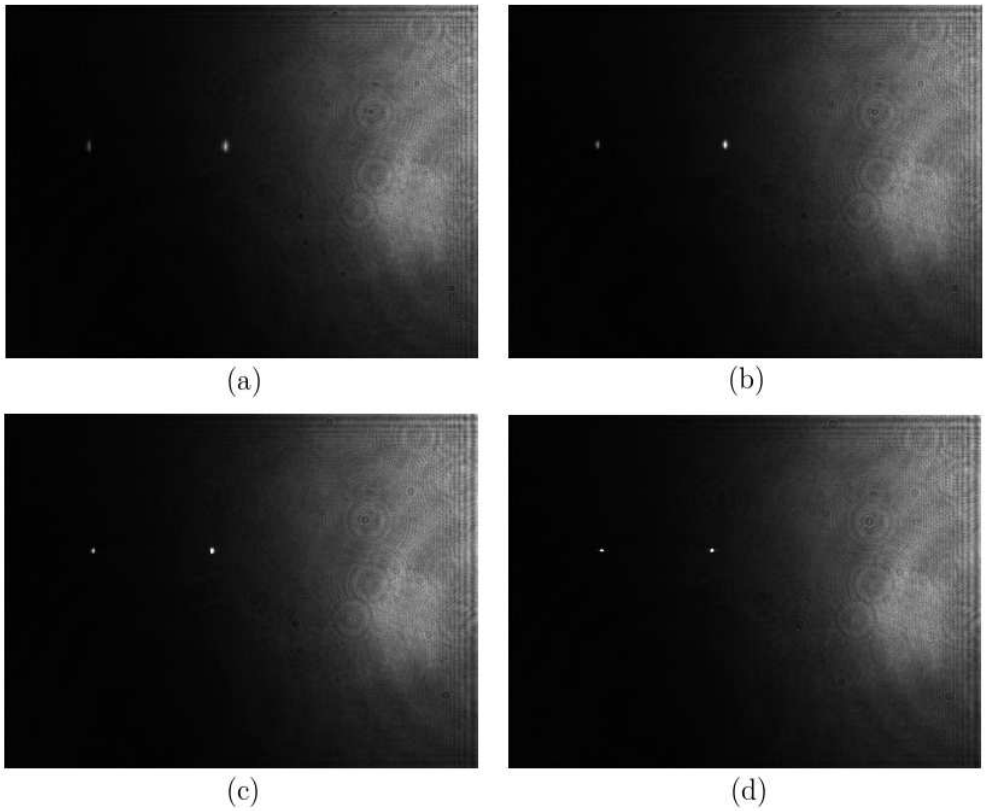

Figure IV.15: Reconstruction of a pinhole calibration hologram in four different planes. From (a) to (d), pinhole source image is refocusing.

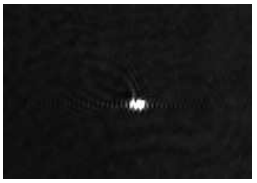

Figure IV.16: Enlarged image of a refocused calibration pinhole image.

Imaging calculations Figure IV.17 shows the simplified imaging system representation for the microscope objective (focal distance $f = 20$ mm), and based on that, the lens equations are:

$$\frac{1}{P_i} - \frac{1}{P_o} = \frac{1}{f}, \tag{IV.3.1}$$

$$\frac{x_i}{x_o} = \frac{y_i}{y_o} = \frac{P_i}{P_o} = M_t < 0, \tag{IV.3.2}$$

where M_t is the transversal $(x - y)$ magnification.

Figure IV.18 shows more details concerning the distances and parameters used in the imaging equations. Before recording the pinhole holograms, a

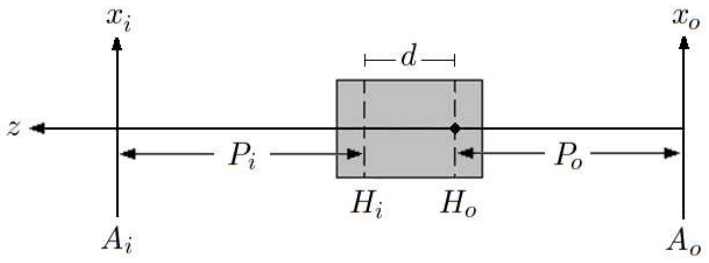

Figure IV.17: Model for the microscope objective, composed of two inner lenses but modeled as a single thin lens. $P_o = \overline{H_o A_o} < 0$, $P_i = \overline{H_i A_i} > 0$, $f > 0$, $\overline{H_o H_i} = d$. Here, index "o" denotes "object" and "i", "image".

focused image of a small ruler placed on the tunnel wall (with its marked side facing down so that the marks were exacltly in the wall plane) was registered, and will be useful later on. After that, both camera and objective were moved downwards by $\varepsilon = 0.2$ mm with a precise translation stage. According to that, plane A_o in figure IV.18 is the plane that would be in focus on the CCD sensor, for the represented positioning configuration.

The imaging system as a whole is therefore characterized by a combination of two optical systems: the lens imaging system and the holographic imaging system. With respect to the lens reference frame z, the lens system brings a given particle or point source p in plane A_{op} from (x_{op}, y_{op}, P_{op}) to (x_{ip}, y_{ip}, P_{ip}) in plane A_{ip} (i.e., from space $\S_I$ to space $\S_{II}$). The image formed in plane A_{ip} has a magnification M_{t_p} characteristic of the particle's depth plane within the tunnel. The holographic imaging system — which can be regarded as a lens, or more specifically, as a diffraction grating (see chapter II) — then takes it from (x_{ip}, y_{ip}, Z_{ip}) to $(x'_{ip}, y'_{ip}, Z'_{ip})$, i.e., from space $\S_{II}$ to $\S_{III}$, with respect to the hologram reference frame Z. In other words, after a hologram of the magnified particle signal is registered, numerical refocusing is achieved in the hologram reconstruction space $\S_{III}$, at a certain center position $(x'_{ip}, y'_{ip}, Z'_{ip})$. Clearly, space $\S_{II}$ is where all the interference takes place, because it is where the reference wave is recombined during the recording step.

As mentioned before, d_i and d_o are parameters that refer to the positions of the inner lenses within the microscope objective, taking as reference the plane A_o that would be in focus for that distance from the objective to the CCD depicted in figure IV.18. So, for that specific distance, the plane indicated — delimited by d_o — would be in focus, because the whole ensemble (objective + camera) was moved down by ε after focusing on a small ruler in the top-side wall plane.

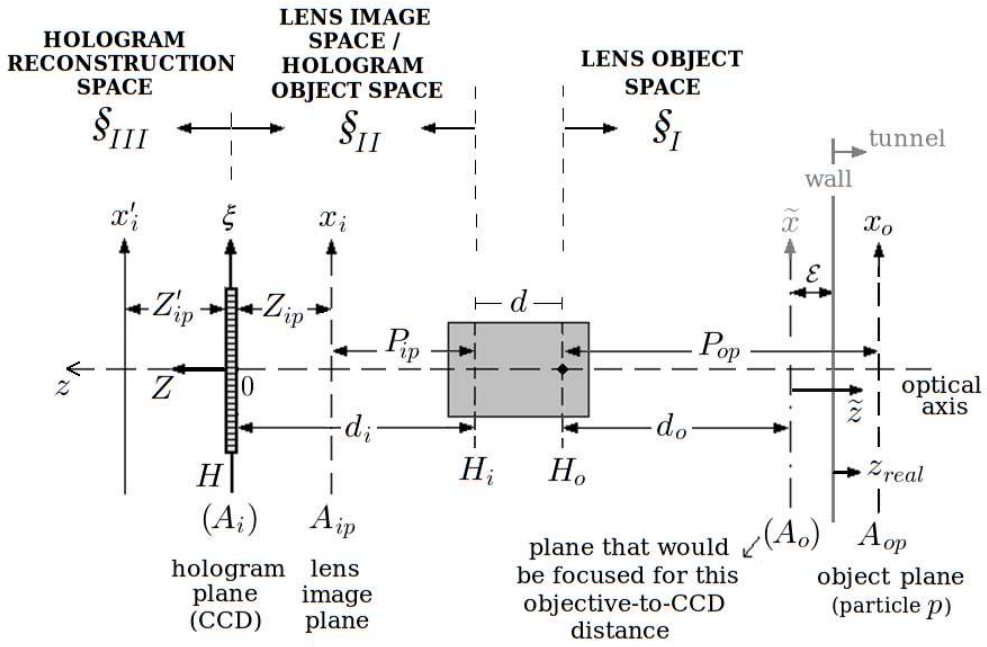

Figure IV.18: Model for whole-system imaging equationing, given a particle or point source p in plane A_{op} inside the tunnel. z is the main coordinate for the lens equation. Z and $\tilde{z}$ are local coordinates with origin on the CCD (hologram) plane, and in reference plane A_o, respectively. In the lens equation reference frame z, $\overline{H_iH} = d_i > 0$ and $\overline{H_oA_o} = d_o < 0$. In the hologram frame Z, the distance from the magnified image of particle p (plane A_{ip}) to the hologram is $Z_{ip} < 0$, and the distance from the hologram to the refocused reconstructed plane of that magnified particle image is $Z'_{ip} > 0$.

In the hologram reference frame Z, $Z_{ip} < 0$ and

$$Z_{ip} = P_{ip} - d_i, \tag{IV.3.3}$$

where P_{ip} and d_i are positive values, because they are expressed in terms of the **lens reference plane**.

As for the holographic reconstruction (see [Goodman, 1968]), **in the hologram reference plane**,

$$\begin{aligned} \frac{1}{Z'_{ip}} &= \frac{1}{Z_{R'}} \pm \frac{1}{Z_R} \mp \frac{1}{Z_{ip}} \\ \frac{x'_{ip}}{Z'_{ip}} &= \mp\frac{x_{ip}}{Z_{ip}} \pm \frac{X_R}{Z_R} + \frac{X_{R'}}{Z_{R'}} \\ \frac{y'_{ip}}{Z'_{ip}} &= \mp\frac{y_{ip}}{Z_{ip}} \pm \frac{Y_R}{Z_R} + \frac{Y_{R'}}{Z_{R'}}, \end{aligned} \tag{IV.3.4}$$

where Z_R and $Z_{R'}$, again, are the distances to the hologram plane of the reference source and the modeled reconstruction source, respectively. (X_R, Y_R)

and $(X_{R'}, Y_{R'})$ are the transversal shifts from the optical axis of reference and reconstruction waves, if they are not centered. Equations (IV.3.4) provide the fundamental relations that allow us to predict the locations of images of point sources created by the holographic process, i.e., the reconstructed images. Depending on the geometry and on reconstruction wave representation, it is possible for one image to be real and the other virtual, or for both to be real or both virtual.

In the wall reference plane, $\tilde{z}_p > 0$ and

$$\tilde{x}_p = x_{op}, \;\; \tilde{y}_p = y_{op}, \;\; \tilde{z}_p = d_o - P_{op}, \tag{IV.3.5}$$

where P_{op} and d_o are negative values as mentioned earlier, because they are expressed in terms of **the lens reference frame**.

For a given particle within the measurement volume, here identified by the index 1, the goal is to calculate its particular real position within the volume, $(x_{o_1} = \tilde{x}_1, y_{o_1} = \tilde{y}_1, \tilde{z}_1)$, from its reconstruction position $(x'_{i_1}, y'_{i_1}, Z'_{i_1})$. With index of generic particle/point source p being replaced by index 1 of the given particle, the set of equations (IV.3.4) becomes

$$\begin{aligned}
\frac{1}{Z'_{i_1}} &= \frac{1}{Z_{R'}} \pm \frac{1}{Z_R} \mp \frac{1}{Z_{i_1}} \\
\frac{x'_{i_1}}{Z'_{i_1}} &= \mp \frac{x_{i_1}}{Z_{i_1}} \pm \frac{X_R}{Z_R} + \frac{X_{R'}}{Z_{R'}} \\
\frac{y'_{i_1}}{Z'_{i_1}} &= \mp \frac{y_{i_1}}{Z_{i_1}} \pm \frac{Y_R}{Z_R} + \frac{Y_{R'}}{Z_{R'}},
\end{aligned} \tag{IV.3.6}$$

and from eqs. (IV.3.3), **hologram reference frame**,

$$Z_{i_1} = P_{i_1} - d_i. \tag{IV.3.7}$$

From lens equations (IV.3.1) and (IV.3.2), in the **lens reference frame**,

$$\begin{aligned}
\frac{1}{P_{o_1}} &= \frac{1}{P_{i_1}} - \frac{1}{f} \\
x_{o_1} &= x_{i_1} \frac{P_{o_1}}{P_{i_1}} \\
y_{o_1} &= y_{i_1} \frac{P_{o_1}}{P_{i_1}}.
\end{aligned} \tag{IV.3.8}$$

Also, from eqs. (IV.3.5), **wall reference frame**,

$$\tilde{x}_1 = x_{o_1}, \;\; \tilde{y}_1 = y_{o_1}, \;\; \tilde{z}_1 = d_o - P_{o_1}. \tag{IV.3.9}$$

Now a hypothesis is made that reference wave was centered in the optical axis during recording — since everything was carefully aligned and centered in the holographic recording system. In fact, before recording, reference wave R was centered in the camera axis with the aid of a millimetric paper target placed symmetrically on top of the camera cover lid.

With the reconstruction step being performed numerically, the location of the reconstruction wave source can be chosen arbitrarily. The obvious choice implemented in the software was for it to be also centered on the optical axis, so that $X_R = Y_R = X_{R'} = Y_{R'} = 0$.

See Appendix A for a detailed discussion about the relevant issue of reconstruction wave representation and its effect on the holographic imaging system $\S_{II} \mapsto \S_{III}$. Here, without getting to details, it suffices to know that, with the chosen representation, R' is a converging wave with source on the left side of the hologram plane in figure IV.18. This was chosen in order to have the reconstructed object field in the positive Z axis (also left side of the hologram plane in figure IV.18), with $1:1$ transversal magnification and $|Z'_{ip}| = |Z_{ip}|$ for any particle p. All this means that, in the hologram frame Z, $Z_R < 0$ (a physical fact from the recording arrangement); and in numerical reconstruction it is assumed that $Z_{R'} > 0$ and $|Z_R| = |Z_{R'}|$.

Then, from eq. (IV.3.6),

$$\begin{aligned} Z'_{i_1} &= \frac{1}{\frac{1}{Z_{R'}} + \frac{1}{Z_R} - \frac{1}{Z_{i_1}}} = -Z_{i_1} \\ x'_{i_1} &= -\frac{Z'_{i_1}}{Z_{i_1}} x_{i_1} = x_{i_1} \\ y'_{i_1} &= -\frac{Z'_{i_1}}{Z_{i_1}} y_{i_1} = y_{i_1}, \end{aligned} \tag{IV.3.10}$$

where the upper signs from eq. (IV.3.6) were used, in order to choose — between the two images (virtual and real) — the one with $1:1$ transversal magnification and $|Z'_{ip}| = |Z_{ip}|$ (again, refer to Appendix A).

From eqs. (IV.3.7) and (IV.3.10),

$$\begin{aligned} x'_{i_1} &= x_{i_1} \\ y'_{i_1} &= y_{i_1} \\ Z'_{i_1} &= d_i - P_{i_1}. \end{aligned} \tag{IV.3.11}$$

Applying equation (IV.3.8),

$$P_{o_1} = \frac{P_{i_1} f}{f - P_{i_1}}, \tag{IV.3.12}$$

and from eq. (IV.3.9)

$$\tilde{z}_1 = d_o - \frac{P_{i_1} f}{f - P_{i_1}}. \tag{IV.3.13}$$

Finally, combining with eq. (IV.3.11),

$$\tilde{z}_1 = d_o - \frac{f(d_i - Z'_{i_1})}{f - (d_i - Z'_{i_1})}, \tag{IV.3.14}$$

so that the difference $\Delta\tilde{z}$ between the real positions of two particles or point sources in the measurement volume is

$$\Delta\tilde{z} = (\tilde{z}_2 - \tilde{z}_1) = \frac{f(d_i - Z'_{i_1})}{f - (d_i - Z'_{i_1})} - \frac{f(d_i - Z'_{i_2})}{f - (d_i - Z'_{i_2})}. \tag{IV.3.15}$$

Notice that, if $\tilde{z}_2 > \tilde{z}_1$ in the wall reference frame, then $Z'_{i_2} > Z'_{i_1}$ in the hologram frame (see figures IV.13 and IV.18). After some algebraic manipulations, d_i can be found to be

$$d_i = f + \frac{A + \sqrt{\Delta}}{2}, \tag{IV.3.16}$$

where $\Delta = A^2 - 4B$, $A = (Z'_{i_1} + Z'_{i_2})$, and B is given by

$$B = Z'_{i_1} Z'_{i_2} - \frac{f^2(Z'_{i_2} - Z'_{i_1})}{\tilde{z}_2 - \tilde{z}_1}. \tag{IV.3.17}$$

The calculation procedure for obtaining d_i and d_o can thus be summarized as follows:

1. Pinhole holograms from each position within the tunnel were separately reconstructed and their reconstructed in-focus depth positions Z'_{i_p} were found, through an intensity-maximizing algorithm with parabolic fitting between planes.

2. A worksheet was created in which different lines corresponded to different pinhole holograms (or different wall-normal pinhole positions in the tunnel). Parameters A, B and Δ were calculated for each one based on the difference from the previous one — because equations described above deal with differences between positions, $\Delta\tilde{z}_p$, and respective reconstruction position differences, $\Delta Z'_{i_p}$, instead of absolute positions.

3. d_i was estimated by averaging all the calculated values from the available pairs.

4. d_o was calculated from d_i and the known objective focal distance f through the lens equation $d_o = \left(\frac{1}{d_i} - \frac{1}{f}\right)^{-1}$.

From this procedure, the values found for d_i and d_o were, respectively, 223.01 mm and −21.97 mm.

With that, the final calibration equations to be implemented in the software for translating reconstructed particle volume into real physical space are:

$$\tilde{z}_p(Z'_{i_p}) = d_o - \frac{f(d_i - Z'_{i_p})}{f - (d_i - Z'_{i_p})}, \tag{IV.3.18}$$

for relating the depth position (index p, as before, refers to each specific reconstruction plane for different particles p), and

$$M_{t_p}(Z'_{i_p}) = \frac{f - d_i + Z'_{i_p}}{f}, \tag{IV.3.19}$$

for evaluating lateral magnifications, and thus calculating transversal grids in coordinates (x_{real}, y_{real}) correctly, for every reconstruction depth plane.

The last thing remaining in order to achieve the correct real-volume depth position $z_{real\,p}$ is to take into account the shift ε:

$$z_{real\,p} = \tilde{z}_p - \varepsilon. \tag{IV.3.20}$$

In the recording of these calibration holograms, the pinhole was positioned in 11 different positions $(\tilde{z}_0, \tilde{z}_1, ..., \tilde{z}_{10})$, from initially closer to the wall — although not at the wall — to successively away from the wall, corresponding to 10 vertical 0.1 mm shifts with the vernier mount ($\Delta\tilde{z}_{10/9} = \tilde{z}_{10} - \tilde{z}_9, ..., \Delta\tilde{z}_{1/0} = \tilde{z}_1 - \tilde{z}_0$)). With that, 10 different values d_i were calculated and then averaged, as explained above.

Estimation of the reconstructed positions $Z'_{i_0}, Z'_{i_1}, ..., Z'_{i_{10}}$ by the algorithm implemented in the software had a low uncertainty. Planes were reconstructed along space $\S_{III}$ with 50 μm regular steps (reminding that any depth difference in reconstruction space is much more elongated than in real space, meaning a shift like 50 μm in $\S_{III}$ corresponds to a much smaller shift in real space, by at least one order of magnitude, depending on the depth). Best focal plane of a reconstructed pinhole image could be distinguished from its immediate neighbors even by visual inspection. With the parabolic-fitting maxima search algorithm, the refocusing positions Z'_{i_p} were chosen with estimated uncertainty of ±15 μm, by analysis of maximum-intensity plots against Z for a small region around the pinhole image center. Thus, it can be said that the average estimated uncertainty for the different $\Delta Z'_{i_p}$'s was no more than ±30 μm.

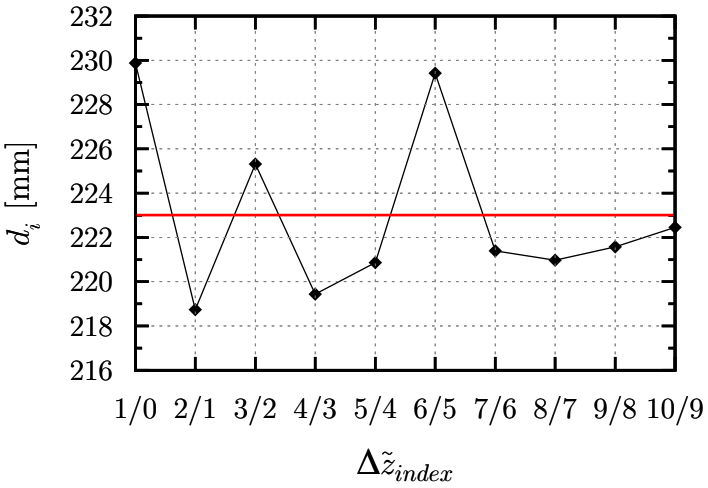

Figure IV.19: Plot of d_i values for the different calibration pinhole shifts $\Delta\tilde{z} = 0.1$ mm within the wind tunnel. Red line corresponds to the average value (223.01 mm).

Both the uncertainties in the $\Delta Z'_{i_p}$'s and in making the shifts $\Delta\tilde{z}_p$'s with the vernier contribute to uncertainty in estimation of d_i, but because the 10 values were averaged in the end, the overall uncertainty was small. Figure IV.19 shows plots of the spreading of d_i values for the 10 different pinhole shifts. The standard deviation was $\sigma_i = 3.90$ mm for d_i, and this was reflected in d_o through the lens equation, leading to a standard deviation of $\sigma_o = 0.037$ mm.

The standard error of the mean, $SE_{d_i} = \sigma_i/\sqrt{N_r}$ (where N_r is the number of individual repetitions in the estimation of d_i, which in this case is 10), is the final estimated error in the evaluation of d_i, so that $d_i = d_{i_{avg}} \pm SE_{d_i}$. In the present case, $SE_{d_i} = 1.233$ mm and $SE_{d_o} = 0.012$ mm, meaning that the final estimated percentual uncertainties in the evaluation of the lens parameters d_i and d_o through the calibration process described above are $\pm 0.55\%$ and $\pm 0.05\%$, respectively.

An analysis of the final estimated uncertainties in the real-volume mapping is presented in Appendix C.

It is worth emphasizing here a particular characteristic of the final calibrated reconstructed volumes: due to the variation of lateral (transversal) magnification with depth, when translated to real coordinates, the volumes become trapezoidal, as in figure IV.20.

For these final calibrated volumes, at the wall — because original planes are imaged through process $\S_I \mapsto \S_{II}$ with higher magnification than planes successively above — lateral grids comprise less actual physical space ("less

millimeters", per say) than on the top of the volume. Lateral magnification ranges from approximately 9.5 at the wall plane to 5.5 at 1.5 mm away from the wall.

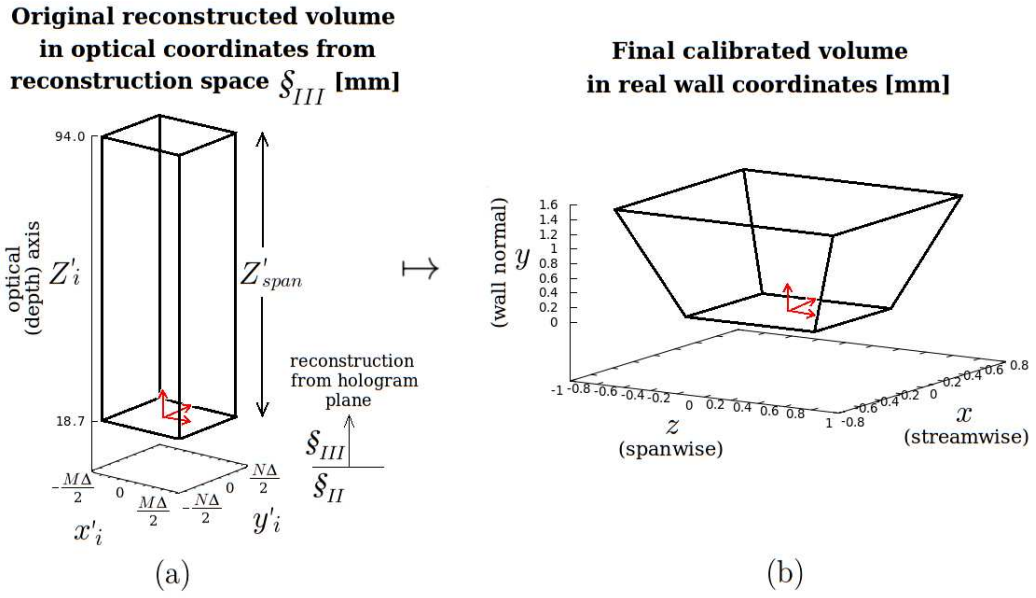

Figure IV.20: Geometry transformation between: (a) volume in holographic reconstruction coordinates (x'_i, y'_i, Z'_i) and (b) final calibrated volume in real coordinates, already switched to boundary layer usual axes (see table IV.1). The reconstruction depth range $Z'_{span} \approx [18.7 \leftrightarrow 94.0]$ mm was used later in numerical reconstruction of particle fields so that the final volume span in real coordinates was $[0 \leftrightarrow 1.5]$ mm in the wall-normal direction, according to eq. (IV.3.18). Because volume (a) is quite elongated, the Z'_i axis is not in scale.

It is important to mention that the coordinate nomenclature choice used in this section for the optical imaging system (x and y being the lateral directions and z being the depth, optical axis direction) is based on the fact that it is the most common choice in holography-related literature, and thus it sounds more familiar. Later, when final coordinates from both frames are stored and the particle tracking code is implemented for velocity calculation, coordinates are transformed to the usual boundary layer (BL) wall coordinates. The conversion is shown in table IV.1 and, as long as this is clear, there should not be any conflicts. The coordinate system change is emphasized in figure IV.20, where the original reconstructed volume is shown in the hologram reconstruction space $\S_{III}$ coordinates, and the final calibrated volume is shown in the usual wall-bounded flow coordinates. These are the two extrema of the "mapping process", from numerically reconstructed volume in $\S_{III}$ to wind tunnel measurement volume in BL coordinates.

Table IV.1: Conversion of optical equationing coordinates to boundary layer usual coordinates.

***Optical* coordinates**			***BL* coordinates**	
	Reconstruction space $\S_{III}$	**Calibrated wind-tunnel space**		
(lateral)	x'_i	x_{real}	(spanwise)	z
(lateral)	y'_i	y_{real}	(streamwise)	x
(depth axis)	Z'_i	z_{real}	(wall-normal)	y

Additional Remarks Two additional considerations are important, regarding the calibration process described above. They are discussed here, now that the process is already delineated and understood.

The first one is related to the presence of a small (2^o) angle in the tunnel wall measurement station during the experiments (see section IV.1 in the beginning of the present chapter). Figure IV.21 shows a sketch of the geometry very close to the wall, with an exaggerated angle representation for visualization purposes.

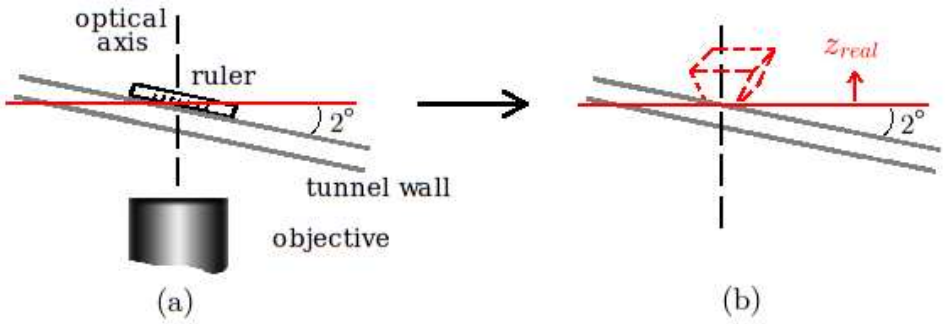

Figure IV.21: Out-of-proportion sketch illustrating the effect of the small wall angle.

As already mentioned in the beggining of the calibration process description, a small ruler (smaller spacing = 50 μm) was placed on top of the tunnel wall with marks facing down, and its magnified image was focused on the CCD sensor. After that, camera-objective ensemble was moved down by ε, being positioned as in figure IV.18, so that the plane that would be in focus in the new position would be A_o. However, in figure IV.18, the wall angle was not depicted.

So, it is useful to clarify here that, when focusing the ruler image, care was taken so that the sharpness of the ruler marks was at its best in the very

center of the image, that is, corresponding to an object plane represented by the red line in figure IV.21 (a). But it should also be emphasized that — since the angle was very small — the sharpness difference from the center to the edges of the ruler image was subtle.

In the end, after eqs.(IV.3.18) and (IV.3.20) are applied, what happens is that the origin of the z_{real} coordinate is as illustrated in IV.21 (b), where the position and geometry of the final volume are also shown, not to scale. Towards one border of the volume, a very small region that is actually within the wall will be reconstructed, and towards the other border, the bottom of the volume will be slightly above the wall, by the same amount (which is no more than 25 μm in the extremes of the volume). In any case, since wall coordinates are correctly retrieved by calibration equations, this is not a problem.

Additionaly, any velocity vector resulting from the particle tracking code described in the next chapter will be corrected in the end, having its components realigned with the flow direction. But, again, the differences are very small because the angle is very small.

The other important consideration is about the possible uncertainty in the estimated measurement of Z_R, the reference source distance. The value was carefully measured before recording the calibration holograms and, as mentioned earlier, it was estimated as $Z_R = 77.5$ cm. Hence, this value was used for $Z_{R'}$ as well, so that $|Z_{R'}| = |Z_R|$ in order to fulfill the $1:1$ holographic imaging assumption. Then d_i and d_o were calculated as described above.

After that, an analysis was carried out to evaluate the sensitivity of the *mapping-to-real-volume* process to the choice of $Z_{R'}$. The whole process described before to calculate d_i and d_o was applied for different values of $Z_{R'}$, revolving around the original estimated value. This was done even for values very distant from the measured value, to see the behavior. Then, with the resulting values for each case, the Z'_{span} previously calculated — which is the correct reconstruction span in $\S_{III}$ to scan the measurement volume from $z_{real} = 0$ to 1.5 mm supposing $Z_{R'} = 77.5$ cm is correct — was mapped to the real volume space. This is shown in figure IV.22, with values of $Z_{R'}$ ranging from 72.5 to 82.5 cm.

It can be noted that, if the value of $Z_{R'}$ — which ideally would have to be exactly the same as Z_R, the physical source distance from the reference wave to the CCD sensor during recording — varies by one or a few centimeters, the effect on the mapping process is not negligible, specially away from the wall, at the top of the measurement volume. At $z_{real} \approx 1.5$ mm, a 10 cm variation on $Z_{R'}$ yields a 0.146 mm uncertainty in the mapping to z_{real} coordinates. An

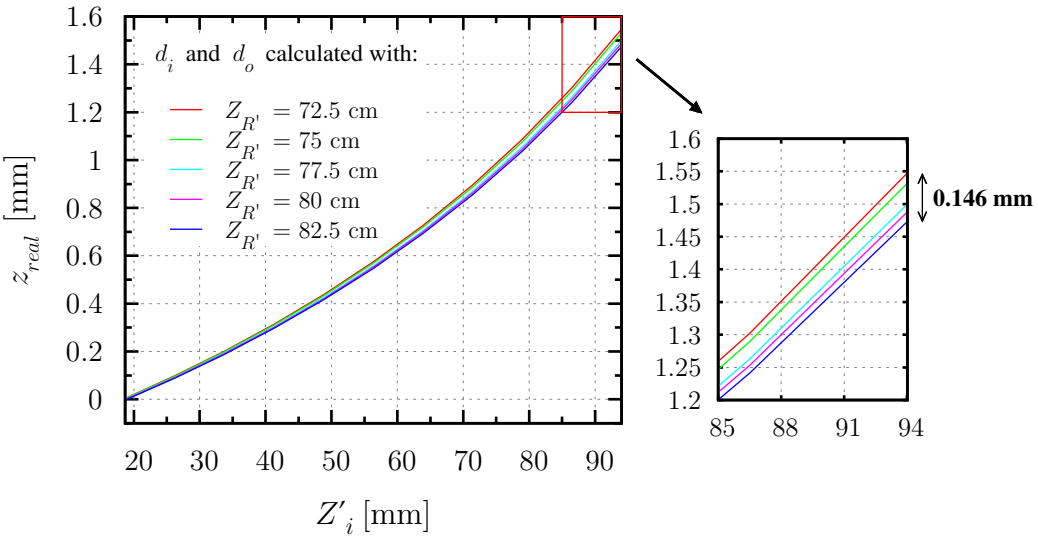

Figure IV.22: Real-volume spans resulting from calculating d_i and d_o using the calibration process with different values of $Z_{R'}$. The non-linear mapping relation from $\S_{III}$ to real space can be observed.

analogous uncertainty occurs for the transversal magnifications as well.

For this reason, the ruler image was used as a means of further verifying if $Z_R = 77.5$ cm was correct. Several measurements were taken of the spacings between the ruler marks in different positions within the center region of the focused image (even with the small wall angle, values varied very little for different random measurements). Knowing the camera pixel size and the fact that the smallest ruler spacing is 50 μm, the magnification M_{ruler} was calculated for the different measurements and averaged. This resulted in $M_{ruler} = 10.13$ (absolute value). After that, for each case (each $Z_{R'}$ tested in this analysis), an absolute magnification $|M_{test}| = |d_i/d_o|$ was calculated. These values are plotted in figure IV.23 against $Z_{R'}$ values from the test cases. The value corresponding to the intersection with $M_{ruler} = 10.13$ (red line), 76.8 cm, was chosen as the best estimation of the reference source distance Z_R. From then on, values of d_i and d_o taken from $Z_{R'} = 76.8$ cm were defined as the correct values to calibrate the particle volumes through eqs. (IV.3.18) and (IV.3.20). The span Z'_{span} in space $\S_{III}$ was also corrected and slightly modified.

As expected, the corrected value is very close to the original measured value $Z_R = 77.5$ cm, and so are the new values of d_i and d_o (222.7 mm and $-21,97$ mm, respectively). Hence, this test was in fact more of a verification, eliminating the doubt as to whether or not a more significant source of error had been introduced. After all, the measurement of Z_R during recording was

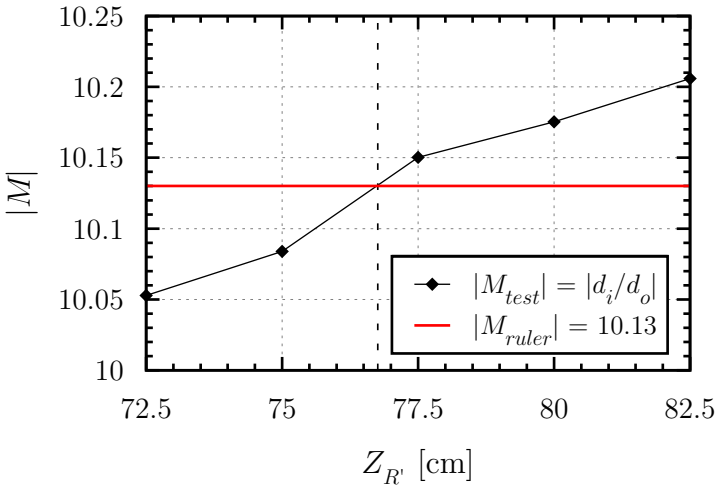

Figure IV.23: Verification of reference source distance value through a comparison with the ruler image magnification.

rendered slightly difficult due to the optical re-directionings and different components in the setup.

Finally, at this point, the optical setup has been thoroughly described. Calibration procedure and its uncertainties are also fully described, as well as the shape of the final volumes retrieved when equations (IV.3.18), (IV.3.19) and (IV.3.20) are applied. The next step is a presentation of the particle holograms taken in the final wind tunnel acquisitions, along with their characteristics and reconstructions. This is done in the next chapter, in which all the algorithms implemented in *HPIVlml* for image processing of the reconstructed volumes, particle validation, and particle coordinate location are also commented in detail.

V
Wind Tunnel Results: Particle Holograms, Reconstructed Particle Fields and Tracking Algorithm

In this chapter, the particle holograms taken in wind tunnel flow conditions are finally presented. The corresponding reconstructed volumes, image-processing procedures, and algorithms for particle detection, validation and location are also presented. Lastly, the particle tracking algorithm implementation is described and results are discussed. It is important to mention that, unless it is clearly stated otherwise, the *optical* coordinates are still the ones used here for the moment (see table IV.1).

V.1 Acquisition of the Holograms

Once the calibration procedure described in the last chapter was over, particle holograms could finally be acquired. Calibration pinhole mount and mirrors were removed from inside the tunnel (see figure IV.14), and a small prism was carefully placed on top of the tunnel wall at the correct position (see figure IV.4). In the optical setup itself, nothing should be moved from the configuration used in the preceding calibration procedure, except in the object arm, where small adjustments in the lenses and filters should be made to optimize the object illumination and adjust the prism position.

The whole arrangement of the configuration used to acquire particle holograms is already described in chapter IV, and illustrated in figure IV.4. Again, the only important mention here is that nothing should be changed in the reference arm of the setup, and neither in the positioning of the microscope objective, in order to maintain the same reference characteristics and imaging conditions used in the recording of the calibration pinhole holograms.

The wind tunnel was set to operating conditions, and a smoke generator was used to seed the whole flow inside it, with particle sizes of less than 1 μm. Tests were performed with live images on the computer screen to check for

the quality of the holograms, specially with respect to the object/reference intensity ratio and fringe contrast. For that, according to descriptions in chapter IV, a cardboard was used to block either reference or object beams and some images were saved and compared. Optimization was attempted by playing with filters and lenses in the object arm, and also by adjusting the laser energy. A typical particle hologram is presented in figure V.1.

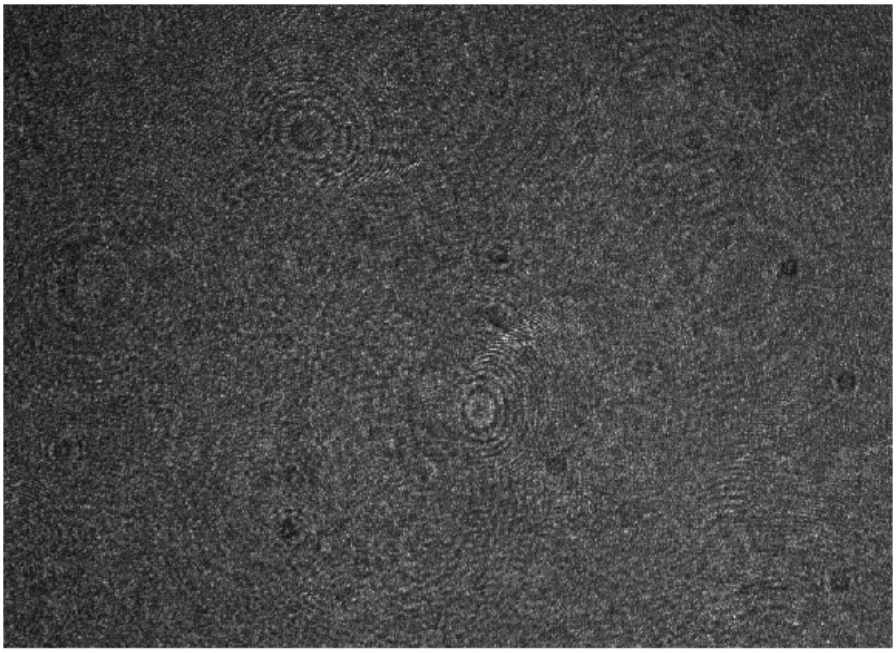

Figure V.1: Example of a typical particle hologram taken from wind tunnel experiments.

There are some noticeable particle fringe patterns, as well as some expected noise arising from the superposition of different particle signals, and signals from some unavoidable dust present on optical components along the reference beam path such as the beam combiner and the CCD glass cover. The patterns with the darker centers, for example, are patterns from dust particles, probably on the CCD cover.

Batches with 500 pairs of holograms were acquired, for wind tunnel velocities $U_\infty = 5$ m/s and $U_\infty = 10$ m/s, in a streamwise station corresponding to one of the stations used for hot wire measurements in the work of [Cuvier *et al*, 2011], located at approximately 0.1 m upstream of the articulated flap, according to the brief tunnel configuration description presented in section IV.1.

V.2 Particle Volume Reconstruction

The particle holograms acquired and saved during the experimental procedure were then reconstructed using the *HPIVlml* software, according to eq.(II.4.6) shown in the theoretical description of section II.4. As explained in that section, the convolution approach was used, and thus field reconstruction was implemented in the software through eq.(II.4.13). Some details on the discrete implementation of the reconstruction equation can be found in Appendix B. Numerical reconstruction of particle holograms could be done on the *LML* computer server, for batch processing.

In chapter IV, figure IV.20 illustrates the shapes of a reconstructed volume in $\S_{III}$ and in final wall coordinates retrieved through the calibration equations. Z'_{span} is the depth range in space $\S_{III}$ to be numerically reconstructed in order to find particles that would be within the 1.5 mm height wall volume depicted in IV.20 (b).

Hence, in order to obtain in the end a calibrated particle volume spanning from $0 \leftrightarrow 1.5$ mm in wall coordinates, the correct $Z'_{span} = Z'_{i_0} \leftrightarrow Z'_{i_f}$ was used as software input to limit the reconstruction range, Z'_{i_0} and Z'_{i_f} being the distances from the hologram plane to the initial and final reconstructed planes, respectively. The values used here for particle volume reconstructions were $Z'_{i_0} = 18$ mm and $Z'_{i_f} = 93$ mm, allowing a margin in the extremes of the previously calculated Z'_{span}. This margin is meant to allow future analysis of the focusing behavior of particles that can possibly be very close to the wall ($z_{real} \sim 0$ mm), or very close to the top of our volume of interest ($z_{real} \sim 1.5$ mm).

Another fundamental input for reconstruction is Z'_{step}, which is the distance between adjacent reconstructed planes, and establishes the depth resolution in $\S_{III}$. For the holograms from this experiment, $Z'_{step} = 0.1$ mm was chosen, but a more refined analysis is introduced later for particle focus detection procedures.

Other inputs in the reconstruction module of the software are the laser wavelength, $\lambda = 532$ nm, camera pixel size $\Delta = 6.45$ μm (the camera used for hologram recording has square pixels, thus $\Delta\xi = \Delta\eta = \Delta$), and the reconstruction source distance, set to $Z_{R'} = +76.8$ cm.

Figure V.2 (a) shows a random reconstructed plane around the middle of Z'_{span}. A few particle images can be seen in their close-to-focus range, either coming in or out of focus, and there is one particle image that — by visual

inspection — appears to be focused (inside the red circle). Figure V.2 (b) shows the depth evolution of cropped images around this very same particle in successive reconstruction planes around the estimated focus position, with finer 50 μm steps between them.

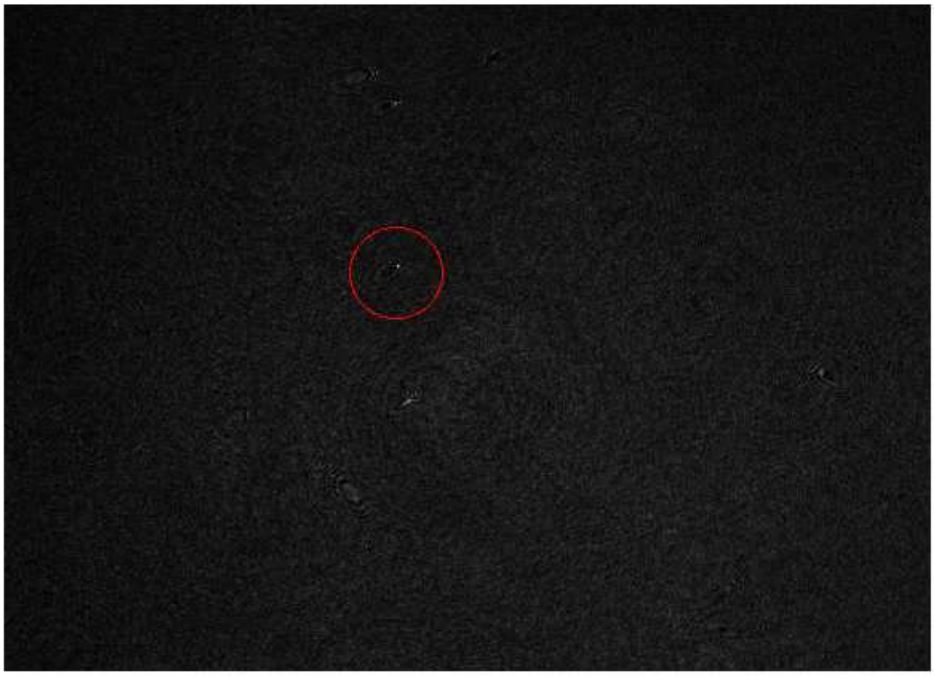

(a)

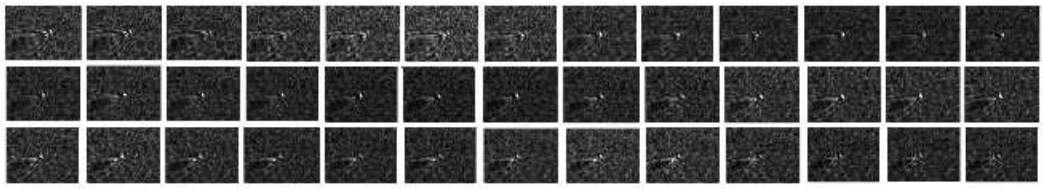

(b)

Figure V.2: (a) Reconstructed plane in a given depth position within Z'_{span}. Particle enclosed by the red circle is around its focus position. (b) Depth series of cropped images around that single particle, with 50 μm spacings between them.

After numerical reconstruction, the resulting field $b'_P(x'_i, y'_i)$ comprises both real and imaginary field data, available for all planes P along the scanned volume. Because all of this information can be useful later for determination of particles refocusing positions, the whole dataset was stored, retaining complex information as well. Four types of data were separately stored:

- ***Intensity*:** The intensity distribution $I_P(x'_i, y'_i)$ in each depth plane, defined as the reconstructed field multiplied by its conjugate;

- ***Gradient*:** For every depth plane, the $x - y$ spatial gradient image of the corresponding intensity data was computed[1];
- ***Real*:** The real part of the reconstructed field, $\Re(b')$, evaluated in each plane;
- ***Imaginary*:** The imaginary part of the reconstructed field, $\Im(b')$, evaluated in each plane.

Those quantities are defined in section II.4, and by combining real and imaginary data through eq.(II.4.7) the phase distribution is obtained.

The data was organized according to the structure depicted in figure V.3. A C++ library called *NetCDF*[2] — which manages and stores large scientific data structures — was used, and also provided support for a user interface to access reconstructed volume data in its different forms (see figure V.4).

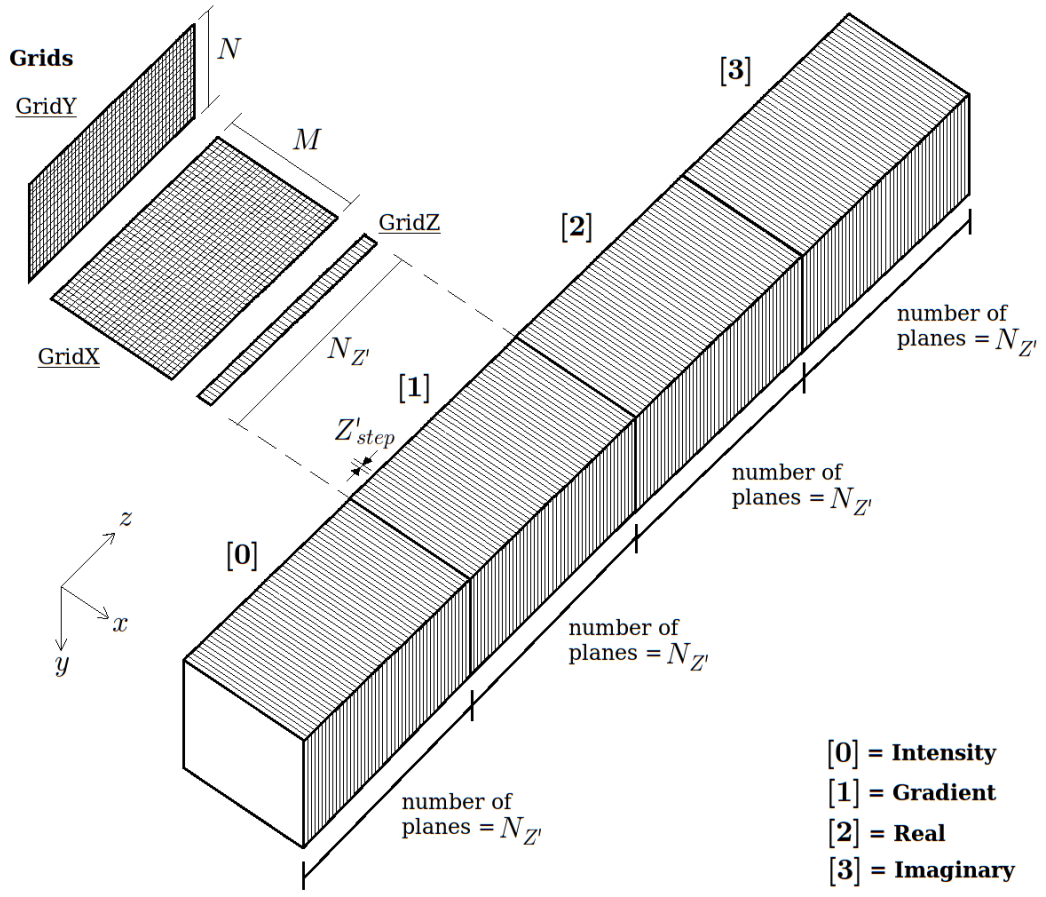

Figure V.3: Data storage structure for the reconstructed volume.

[1]Calculated through the x-y simple centered finite differences.
[2]http://www.unidata.ucar.edu/software/netcdf/

Figure V.4: Visualization interface for NetCDF files generated from the holograms. Different options are available, such as choice of tha data variable or grid variable to be presented, linear and non-linear color scales, zoom, movie-type visualization along depth, etc.

Volume structures comprising $N_{Z'} = \left[[(Z'_{i_f} - Z'_{i_0})/Z'_{step}] + 1\right]$ planes are stored in four different "channels" ($[0], [1], [2], [3]$), corresponding to intensity, gradient, real and imaginary data, respectively, such that plane $P_k[0]$, for example, is the intensity distribution in plane P_k, $k = 0 : (N_{Z'} - 1)$. M and N are the number of elements in the the x and y directions, respectively (corresponding to the number of pixels in the camera for each direction).

Grids are stored in separate structures. The lateral x and y grids are two-dimensional, extending in depth and thus having $M \times N_{Z'}$ and $N \times N_{Z'}$ elements, respectively. The depth grid has $N_{Z'}$ elements. The unlimited dimension for this *NetCDF* data structure is the depth of the volume, meaning Z'_{span} could be extended arbitrarily, and $N_{Z'}$ could be as large as desired, limited only by storage capacity restrictions.

Initially, non-calibrated grids are generated. Depth grid has values $\{Z'_{i_0}, (Z'_{i_0} + Z'_{step}), ..., (Z'_{i_f} - Z'_{step}), Z'_{i_f}\}$, while lateral grids values are indexed, varying from $-\frac{M-1}{2}$ to $\frac{M-1}{2}$ and $-\frac{N-1}{2}$ to $\frac{N-1}{2}$. These non-calibrated grids correspond to a representation of the reconstructed volume as depicted in figure IV.20(a).

Then, a calibrated grid is generated from the non-calibrated one by properly applying equations (IV.3.18) to (IV.3.20), presented in chapter IV. For the depth grid this is straightforward. For the lateral grids, indexed values

are multiplied by the pixel size Δ and divided by the magnification calculated from eq.(IV.3.19) for the corresponding depth. In this way, the final calibrated grids correspond to a representation of the reconstructed volume as depicted in figure IV.20(b), with coordinates $(x_{real}, y_{real}, z_{real})$.

V.3 Particle Detection, Validation and Focusing Criteria

At this point, reconstructed volumes are properly stored in a compact format, which allows data visualization, manipulation and reading. Volume data is organized by type, and separate grid structures are available in both indexed and final coordinates $(x_{real}, y_{real}, z_{real})$.

The next step is to scan the volume for detection of particle signals. In a preliminary analysis, in which *particle candidates* are chosen, the following steps are executed by the corresponding module of *HPIVlml*:

- Data and grid are loaded from the stored reconstructed volume structure depicted in figure V.3;
- for every loaded plane P_k, a blurred version of the intensity image is subtracted from the original image, i.e., ${P^*}_k[0] = P_k[0] - P_{k_{blur}}[0]$. Smoothing filter parameters are carefully chosen to provide elimination of border effects and reduction of low-frequency spatial variations;
- Pre-processed intensity data from all planes is compiled in a single 3D image, and a histogram analysis of this volumetric image is performed for detection of bright spots. In the normalized histogram, very bright pixels associated with possible particle candidates have a low number of occurances, clustered at the right end of the histogram plot.
- A threshold value is properly chosen[3] from the histogram analysis, and is used to binarize the volumetric intensity image. Small clusters of 1-valued pixels are formed where possible particles are located. The rest of the volume is comprised of 0-valued background pixels.
- Groups of points concentrated within a certain radius are analyzed so that only one point is chosen (the one with the brightest intensity in the original non-binary volume) as the location of the particle candidate.

[3]Depending on the different experimental parameters such as particle size, scattering angle, magnification, reference wave nature, among others, the particle images and the background in the reconstructed volume can present somewhat different characteristics. Thus, it is unavoidable to have to "tune" certain software input choices for the particular experiment in question, such as the threshold value in this preliminary selection of particle candidates. Choice of the threshold value is then made after observation of several trial-and-error results.

– A matrix is saved with the indexed coordinates of the particle candidates.

"Tube" Structures In the following step, *tube* structures are created around the positions of the particle candidates. These structures and their storage are similar to the ones used for the whole volumes. They are meant to separate regions around the particle candidates for a more detailed investigation.

Based on a given particle candidate's depth coordinate Z'_c from the preliminary analysis, a new volume structure such as the one in figure V.3 is generated, only this time reconstructed with a finer step $Z'_{finestep}$, from $[Z'_c - (K_t * Z'_{finestep})]$ to $[Z'_c + (K_t * Z'_{finestep})]$. Thus, this volume is centered on Z'_c and has a depth extension which should be sufficient for a thorough depth behavior analysis of the candidate. K_t is a user-input parameter that controls how large this extension is. Indexed and real-coordinate grids are also generated for these fine-step volumes, which are created for all particle candidates.

Next, the volumes are cropped in x and y directions, so that only a smaller region around the particle candidate's center is left. These are denominated "tubes", and their strucuture is depicted in figure V.5.

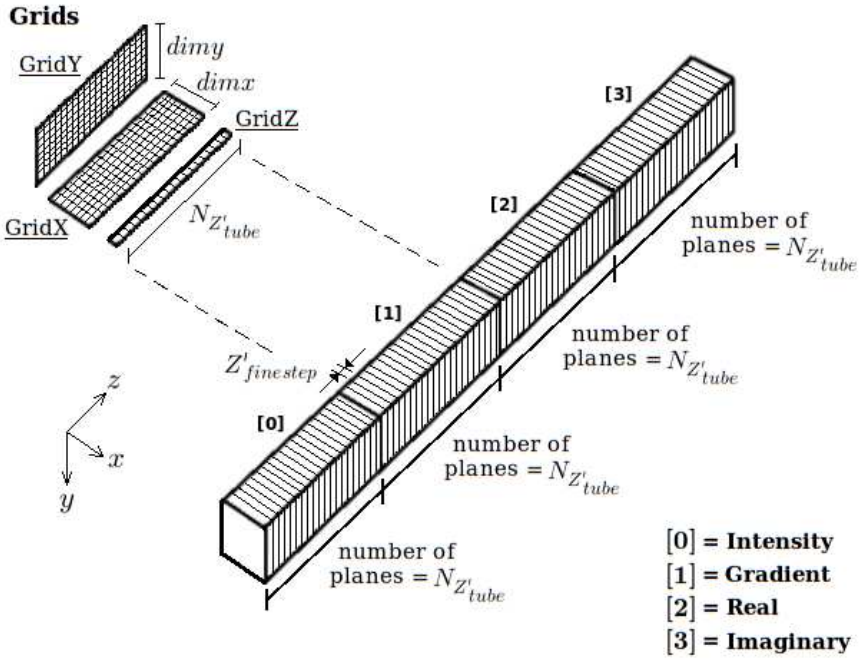

Figure V.5: *Tube* data structure. Plane-by-plane data and grids are created by cropping planes and grids from a volume reconstructed with a finer step $Z'_{finestep}$. The structure is basically the same as for volumes, but the unlimited dimension here is the number of tubes (or the number of particle candidates).

$N_{Z'_{tube}}$ is the number of depth planes resulting from the choice of $Z'_{finestep}$ and K_t, and *dimx* and *dimy* are the number of pixels comprised in the lateral dimensions of the tube, cropped from the corresponding volume as explained above. Those are also user inputs, and should be carefully chosen after a preliminary analysis of the average size of typical particle images, so that no important data concerning the candidate is cut out. Also, particularly for this experiment, because of the depth-varying magnification, particle images present a slight transversal displacement as they evolve in depth. This will be noticed later on when particle tube images are presented. In any case, *dimx* and *dimy* should be large enough that all the information one wishes to analyze is fully comprised within the tube. On the other hand, unnecessarily larger tube sizes can lengthen calculations and make the *NetCDF* files too large. After testing the effect of different sizes in the criteria evaluations that will be presented next, $dimx = dimy = 10$ pixels was chosen here. A reconstruction step $Z'_{finestep} = 50$ μm was used.

Grid structures for the tubes are also stored in both indexed (or, as for the volumes, indexed *gridx* and *gridy*, and *gridz* in $\S_{III}$ depth coordinate) and real-volume coordinates, being generated through cropping of the original fine-step volume grids.

Thus, the tubular structures are small, with size fully determined by user-input choices. They are stored in a single *NetCDF tube* structure, in which the unlimited dimension is the number of tubes.

At this point, there might be tubes that do not correspond to valid particles signals. So, the next step is an investigation of each tube separately, and the application of a *validation* criterion. If a given particle candidate is rejected, its corresponding tube is removed from the *NetCDF* tube structure.

Particle Validation In this part of the software routine, the tubes are analyzed each at a time, in order to determine whether the particle candidates can be considered valid particle signals. An intensity (original grey values) histogram analysis based on the whole tube, that is, the ensemble of all $N_{Z'_{tube}}$ planes, is performed. Figures V.6 to V.8 show three examples of particles candidates and their histograms, computed from tube intensity data of the candidate being analyzed. In these figures, the depth evolution of the particle candidate image is also shown (on the top), each small square corresponding to a plane in the tube, with growing depth from left to right, placed next to each other. Top and bottom rows correspond to intensity and gradient data, respectively. Below the image series, the corresponding intensity histogram

plots are presented.

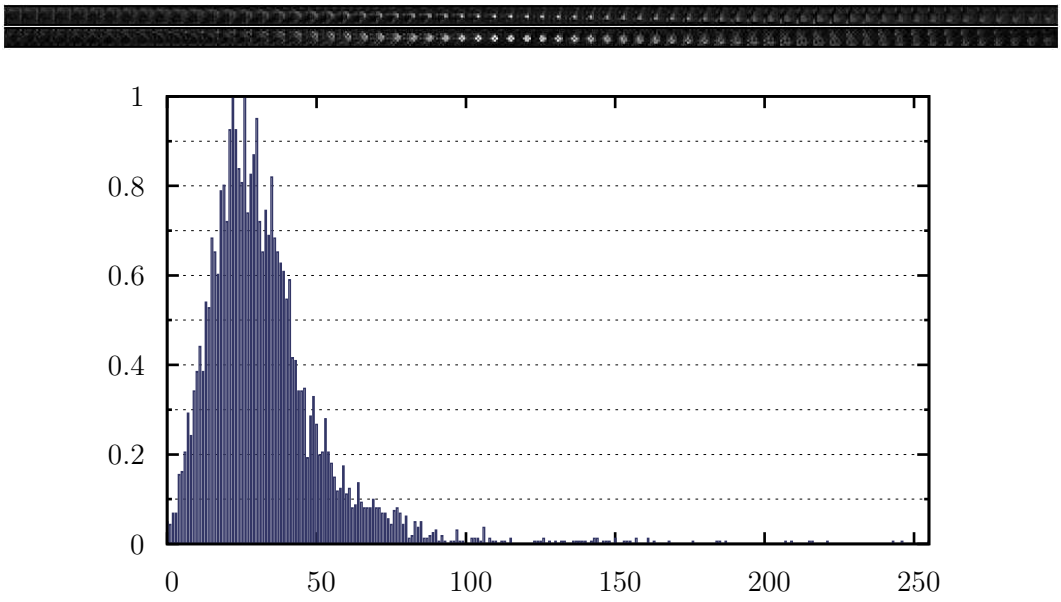

Figure V.6: Top: series of tube-plane images (intensity above and gradient below) of particle candidate A. Bottom: corresponding whole-tube intensity histogram.

In the case of particle A, visual inspection of the tube using the software interface leads to the conclusion that it is a valid particle[4]. The histogram reflects this, having a high decay slope and very low values to the right of the peak. Good particle signals have high contrast with its surroundings, so histograms will show more occurances in the very low values, corresponding to a quite dark background opposing a few very bright pixels pertaining to the particle's focusing region. It can be noticed that particle images are of the order of a pixel, and when contrast is as high as it is for particle A, the spatial gradient image in the focus position has the form of a "cross", with four white pixels and a black one in the middle.

Particle B also looks like a valid particle by visual inspection. Histogram still reflects this, although the peak is not so narrow in comparison to particle candidate A. This is because the background is slightly more noisy and grey.

As a final example, figure V.8 shows particle candidate C. Depth evolution images (in this case shown only for intensity) clearly suggest that it is not a valid particle. The histogram spreads to the right end, with a low decay slope. Even if it is a particle whose image for some reason has not been formed with good contrast, it is cautious to reject it.

[4]At this point, again, some level of hands-on inspection of different volumes and batches from the experiment in question is necessary. Visual observation of particular characteristics of several particle images is made in order to adapt algorithm input values, such as the lower limit value of the decay slope in the normalized tube histograms.

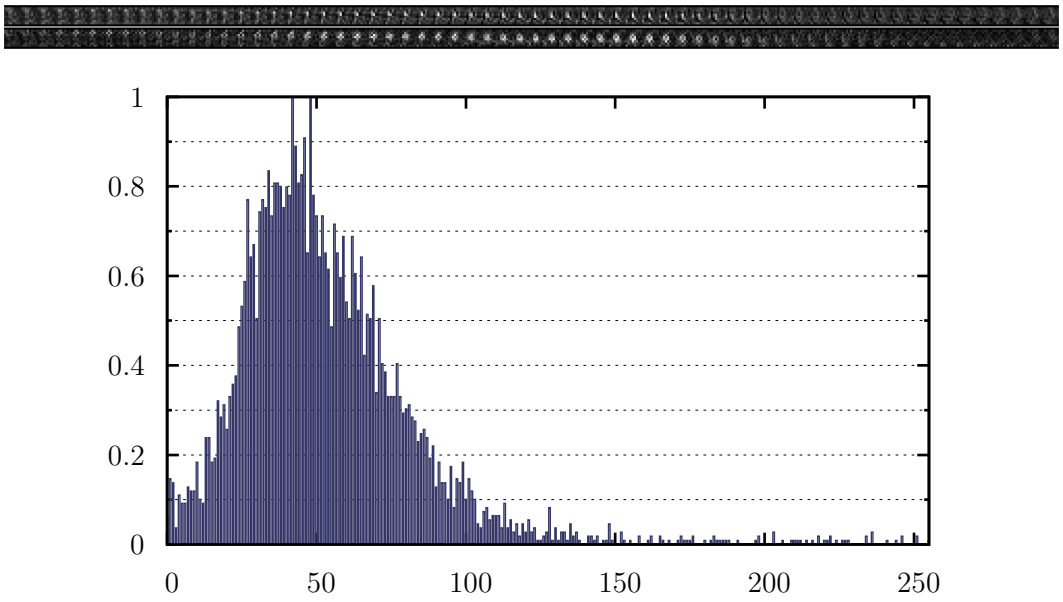

Figure V.7: Top: series of tube-plane images (intensity and gradient) of particle candidate B. Bottom: corresponding whole-tube intensity histogram.

Overall, it can be noticed that in the case of candidates which are indeed particles, usually the space between the very bright right end and the dominant peak in the histogram is filled with a very small number of occurances, which reflects an improved contrast between particle signal and background as a particle approaches its focus position. For different examples of valid particles, though, the peak might shift a bit to the left or to the right, indicating that the overall background can be more black or a bit more greyish. Nevertheless, what is more important as a factor for validation is the decay slope to the right of the curve. Thus, the formal implemented validation algorithm addresses the spreading of the histogram on its right-side, through evaluation of the decay slope. Comparing normalized validation criteria values, candidates are validated or rejected as particles. Tubes corresponding to rejected candidates are removed from the tube data structure.

As for the particle candidates shown here as example, A and B were indeed considered valid by the implemented validation algorithm, whereas candidate C was rejected and removed.

Figures V.9 and V.10 show the tubes corresponding to particles A and B, respectively. In these figures the intensity data is presented, ranging from blue to red in intensity levels. Only a few planes are depicted, the ones towards the extremities of the tube being left out, to facilitate visualization around the center region. In these figures, the difference between signals from particles A and B, both validated, is noticeable. In the case of particle A, the spots with

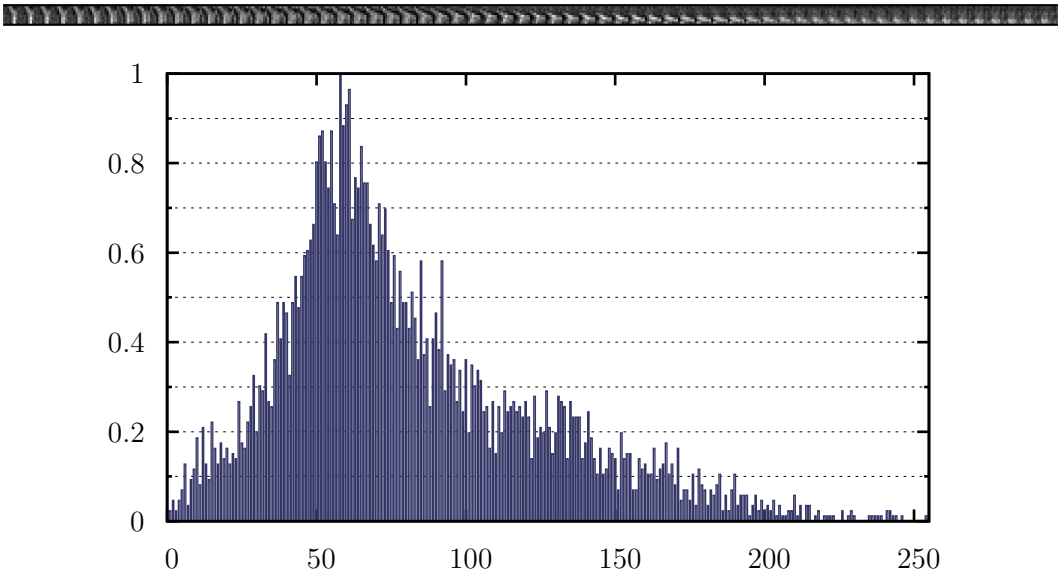

Figure V.8: Top: series of tube-plane images (intensity only) of particle candidate C. Bottom: corresponding whole-tube intensity histogram.

highest values, represented in red, are pretty much concentrated in the very center of the tube, and around them intensity rapidly decays to the lowest blue values. In the case of particle B, red spots appear in a more extended depth range, and the background has more intermediate blue values. Nevertheless, both are valid particles, and present enough depth-evolving characteristics as to establish a proper criterion to formally evaluate their estimated focal position. Steps between reconstructed planes are $Z'_{finestep} = 50$ μm in reconstruction space $\S_{III}$. Table V.1 indicates the corresponding average steps and overall tube lengths in real-volume dimensions for particles A, B and two other hypothetical particles, one very close to the wall and other close to the top of the volume. These values give an idea of the magnitudes of the variations encountered throughout the depth direction in the reconstructed volumes, due to the varying magnification.

Figures V.11 and V.12 present iso-contours of 75% of the maximum intensity for particles A and B, respectively, with the tubes borders outlined, giving an idea of the extension of the *quasi*-focus regions for both particles. In the case of particle B, it can be seen that the contour is actually divided in four parts, pointing to the presence of different intensity peaks, which constitutes a particular behavior.

Criteria for Estimation of Focus Position The idea here is to revisit data from the tubes — now only validated tubes containing particles — and further analyze it, in a more detailed fashion, estipulating a *position-estimation*

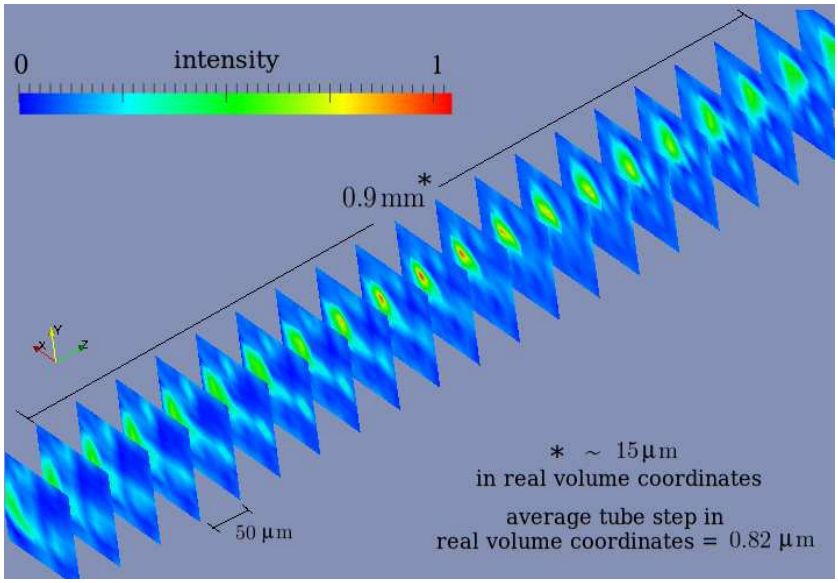

Figure V.9: Tubular structure created around pre-estimated position Z'_{c_A} of validated particle A. This particle has a good signal-to-noise ratio. For visualization purposes, some planes are not depicted here. Intensity values are normalized.

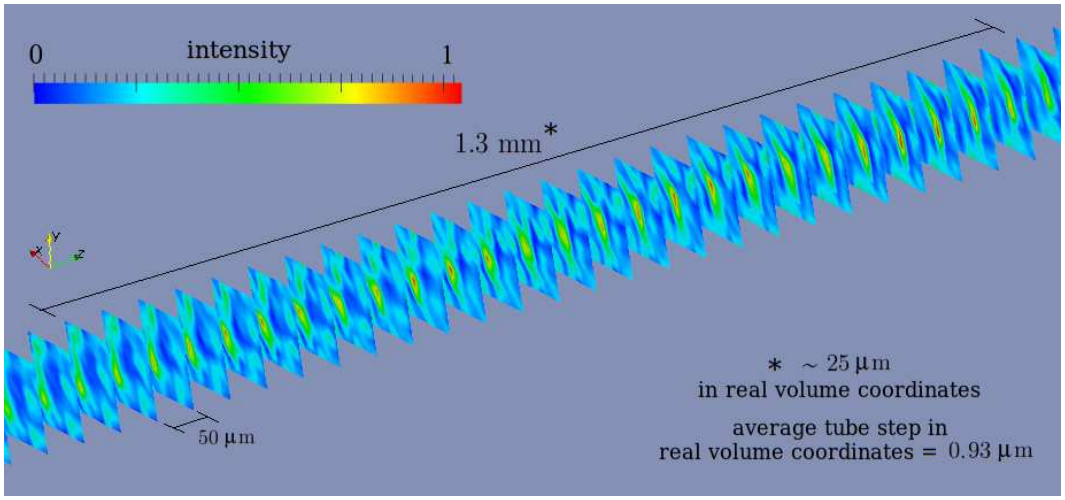

Figure V.10: Tubular structure for particle B. This one has a noisier background and presents more of a challenge for final position estimation. Higher intensity red regions seem to appear in a longer depth extension than in the case of particle A.

Table V.1: Tube steps and overall lengths of four different particle tubes: the ones corresponding to particles A and B, and two others corresponding to hypothetical particles positioned close to the wall and close to the top of the volume.

	Central depth position with respect to the wall [mm]	Total tube length [μm]	Real step $^{(*)}$ at the bottom of the tube [μm]	Real step $^{(*)}$ at the top of the tube [μm]
Particle A	0.40	66	0.80	0.84
Particle B	0.56	74	0.91	0.96
Particle close to wall	0.1	51	0.63	0.66
Particle away from wall	1.4	127	1.56	1.68

criterion, which, in fact, is a combination of different criteria, as explained next.

For each particle tube, plane-by-plane data is investigated, that is, the 2D data images from each of the $N_{Z'_{tube}}$ planes is analyzed, resulting in a value for a given criterion at each corresponding depth position. Then a graph of this criterion as a function of depth can be plotted to aid in the determination of the particle's estimated refocusing position.

Real and imaginary data were analyzed, but did not lead to a quantifiable, discernable depth characteristic behavior (in [deJong and Meng, 2007], however, the authors successfully adapt their complex-based detection algorithm to the case of side-scattering particle fields), so only intensity and gradient data are used here. Two intensity-based and two gradient-based criteria are analyzed for every plane P_k, $k = 0 : (N_{Z'_{tube}} - 1)$:

- **Intensity Maximum***. This is the maximum grey-level value among the ($dimx \times dimy$) pixels in the plane *intensity* image $P_k[0]$, subtracted by the average of the remaining pixel values;
- **Intensity Variance**. Simply the variance of the ($dimx \times dimy$) ensemble of pixel values within $P_k[0]$;
- **Gradient Maximum***. Average of the four highest pixel values in the plane *gradient* image $P_k[1]$;
- **Gradient Variance**. Variance of the ($dimx \times dimy$) ensemble of pixel values within $P_k[1]$.

Intensity and gradient-based criteria plotted against depth direction are shown in figures V.13 and V.14 for particles A and B, respectively. Depth direction is represented with index k, from beginning to end of the

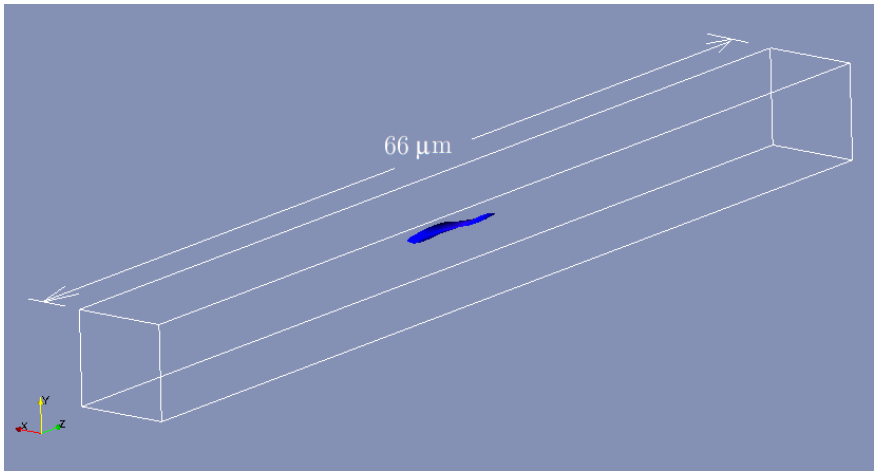

Figure V.11: Particle A: Intensity iso-contour at 75% of the peak intensity.

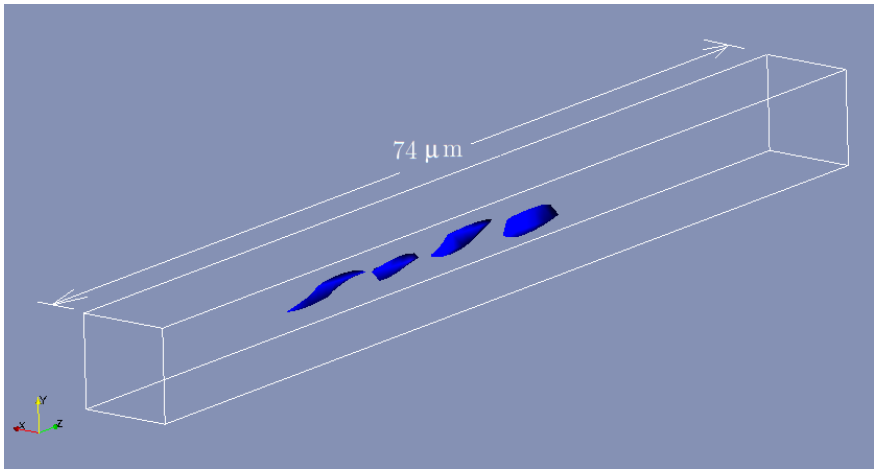

Figure V.12: Particle B: Intensity iso-contour at 75% of the peak intensity.

tube, comprising $N_{Z'_{tube}}$ planes spaced by $Z'_{finestep} = 50$ μm. These 50 μm shifts between tube planes in space $\S_{III}$ correspond to varying shifts in real coordinates within the measurement volume (that is, the tube structure converted to real coordinates changes in shape, and has steps between planes that vary with depth — see table V.1), but within a single tube this variation is very small.

The tube characteristics in these analyses are: $Z'_{finestep} = 50$ μm and $N_{Z'_{tube}} = 79$ planes, leading to a total tube depth of 3.9 mm in $\S_{III}$. As far as resolution in the real space corresponding to these 50 μm steps is concerned, not only it varies within a tube, but also depends on the tube position within the volume. Take, for example, a tube close to the wall, say centered at a position Z'_i in $\S_{III}$ equivalent to $z_{real} = 0.1$ mm in the measurement volume. For such tube, the total length in real coordinates is 51 μm. The step $Z'_{finestep}$

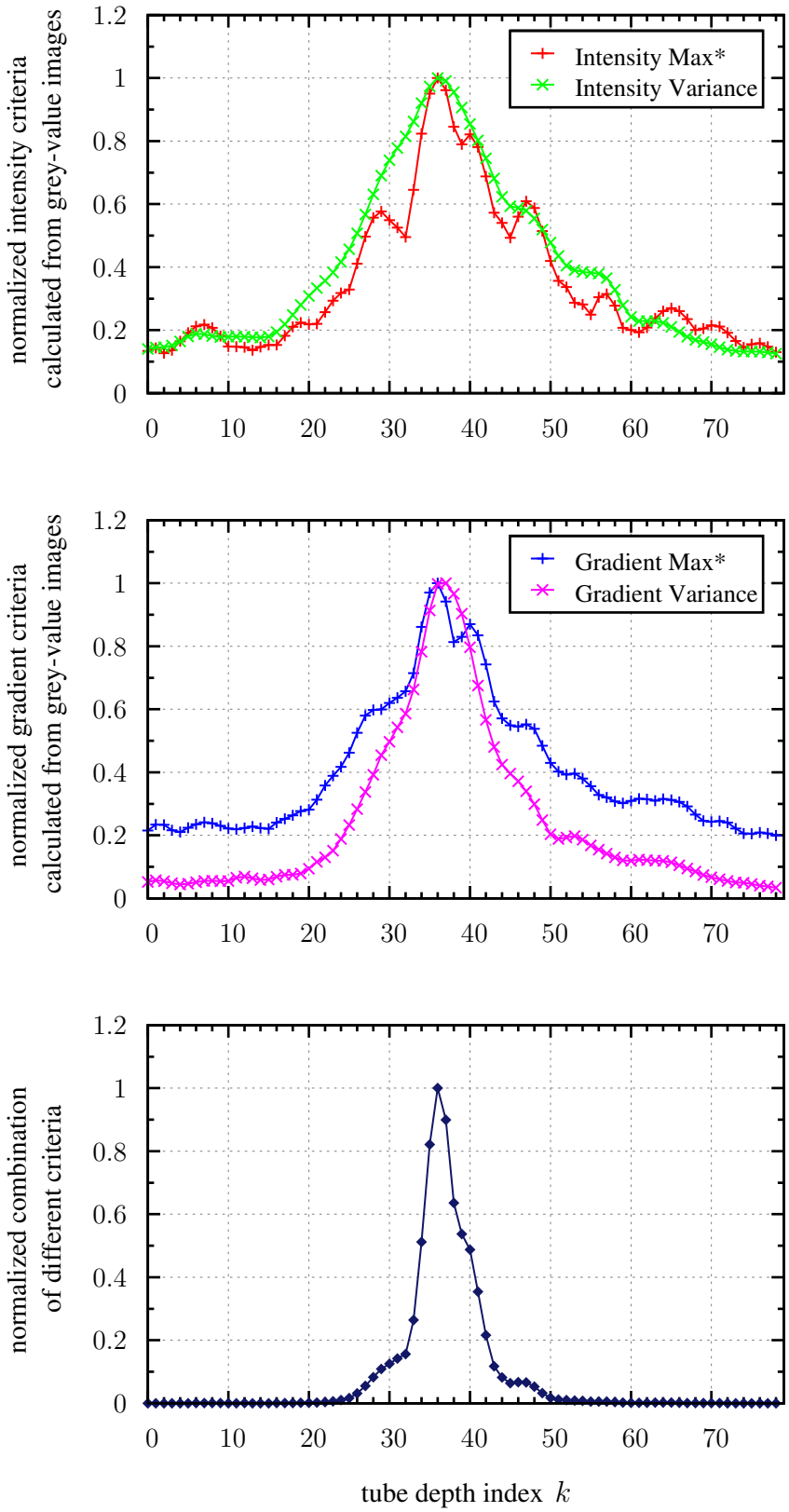

Figure V.13: Plane-by-plane criteria evaluation for particle A. Top: intensity-based criteria; middle: gradient-based criteria; Bottom: combined final criterion for particle focus position evaluation. Steps between planes in reconstruction space is 50 μm.

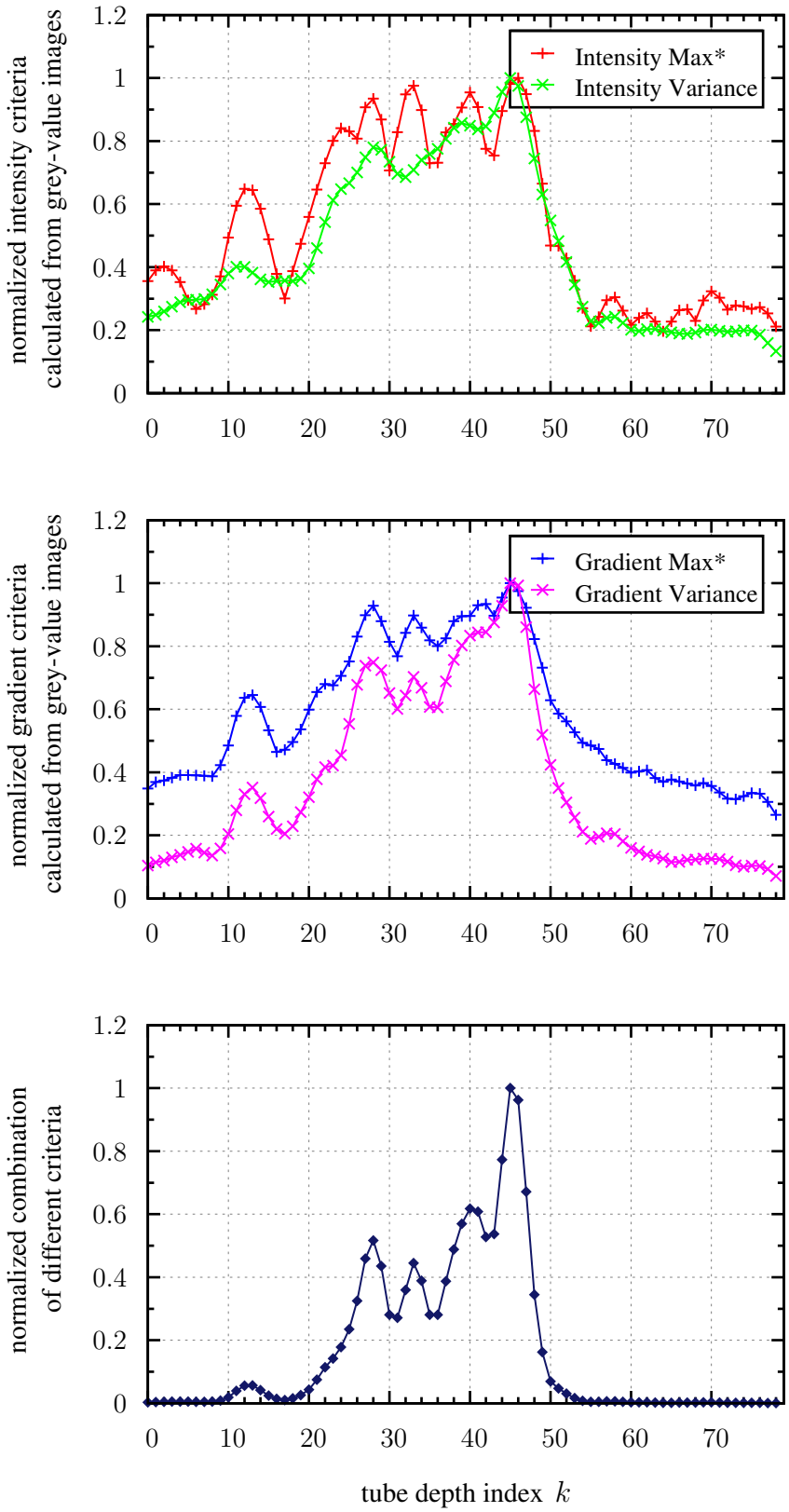

Figure V.14: Plane-by-plane criteria evaluation for particle B. Top: intensity-based criteria; middle: gradient-based criteria; Bottom: combined final criterion for particle focus position evaluation. Steps between planes in reconstruction space is 50 μm.

corresponds to a step of 0.63 μm at the bottom extreme of the tube, and to a step of 0.66 μm at the top extreme of the tube (further from the wall). Considering now a tube centered in $z_{real} = 1.4$ mm in real wall space, its total length in real coordinates is 127 μm. The step $Z'_{finestep}$ corresponds now to a step of 1.56 μm at the bottom extreme of the tube, and to a step of 1.68 μm at the top extreme of the tube. This information is all presented in table V.1.

For each criteria, the values are normalized by the maximum value in the plot. Observation of the criteria presented in the top and middle plots of figures V.13 and V.14 shows that all of them provide valuable information, which can be helpful in the task of improving the estimation of a particle's focus position. On the other hand, specially for particles with weaker signal contrast, using only one of these criteria might not be enough to provide a good estimate of the particle's focus position. Take for example the different individual criteria for particle B, in figure V.14. Values vary more irregularly than in the case of particle A, and have a lower decay rate towards the ends.

Thus, the final criterion is simply the multiplication of the four intensity and gradient-based criteria. It is plotted for particles A and B in the bottom of figures V.13 and V.14, respectively, and generates much more distinct peaks. For particle A, particularly, the final criterion peak is quite distinguishable, and values go to practically zero in a large portion of the tube extent, towards both ends. For particle B, the peak quality can still be observed, characterized by the fact that to a considerable extent from both ends, values go down to close to zero. But it can be seen that the peak is larger and oscillates, consisting of different sub-peaks, the higher one not being centered in the main peak region. Based on those observations, the estimated focus position of the particles was evaluated as follows:

- In the normalized final crtiterion plots, for an imaginary line traced horizontally at value 0.5 in the vertical axis, the first (to the left) and last (to the right) points touched by this line define the approximated "peak region" width;
- Linear interpolation is applied to estimate the index values where the crossings occur;
- The particle center depth position is then estimated as the mid-value between these two values.

As this final algorithm intended to be generalized for all possible particle signal shapes that can be found in a volume, there was not much point in establishing a more refined peak-fitting algorithm that would not be so effective

for particles such as B. For particle B, it is not known in principle what would be the best estimate of the focus position, specially because of the presence of a much stronger asymmetric sub-peak on the right-side of the major peak region.

In the case of particle A, the uncertainty in the choice of the depth position can be estimated to be around ± 125 μm, whereas for particle B, it is estimated to be ± 450 μm in reconstruction space $\S_{III}$, corresponding to much smaller uncertainties in real volume space. After a thorough investigation of all the particles in different volumes taken from the experimental data, it was observed that the maximum focus detection uncertainty in $\S_{III}$ as performed by this algorithm was around the same uncertainty observed for particle B.

Thus, considering a ± 450 μm uncertainty in $\S_{III}$ to be conservative, that would correspond to an uncertainty of ± 2.9 μm for a particle positioned at $z_{real} = 0.1$ mm, and of ± 7.1 μm for a particle positioned at $z_{real} = 1.4$ mm. Note that all these uncertainty estimations are evaluated through application of eq. (IV.3.20) from chapter IV, and do not take into account — for now — the uncertainty in the calibration parameters (see Appendix C).

Hence, after this algorithm is executed for all particle tubes validated in a volume, their indexed depth positions — which now are no longer integers — are evaluated and stored. Then, through linear interpolation, they are used to search for the final calibrated particle positions z_{real_p} in the calibrated depth grid stored in the *NetCDF* data structure.

As for the lateral positions, because particle images can move transversally by small amounts as they evolve in depth, it is important to properly estimate them based on the final chosen depth position. This is done in the following manner:

- Planes P_{k^-} and P_{k^+} surrounding the chosen depth position are evaluated for a maximum-intensity search to estimate $(x_{index}, y_{index})^-$ and $(x_{index}, y_{index})^+$;
- Knowing $(x_{index}, y_{index}, z_{index})^-$ and $(x_{index}, y_{index}, z_{index})^+$, tube grid strcutures $GridX$ and $GridY$ are accessed and linear interpolation is used to evaluate (x_{real}, y_{real}) values.

After the procedures described, the real-coordinate positions $(x_{real}, y_{real}, z_{real})$ within the wind tunnel measurement volume are finally determined. The coordinates of all validated particles are stored in matrices for every reconstructed volume.

An example of a final reconstructed volume is shown in figure V.15. Particle density is not too high, because in a measurement volume so close to the wall, smoke particle concentration may be lower than in the rest of the tunnel. Also, it is difficult to make an accurate estimation of the number of real particles — as opposed to spurious noise — rejected by the validation criterion. Statistics were computed from the experimental batches, and on average, around 65% of the particle candidates were validated in a reconstructed volume, but the percentage of rejected real particles is unkown. For this not so high volume particle density, the use of 3D correlation tools for determination of displacements of groups of particles in sub-volumes is not recommended, and individual particle tracking is better suited.

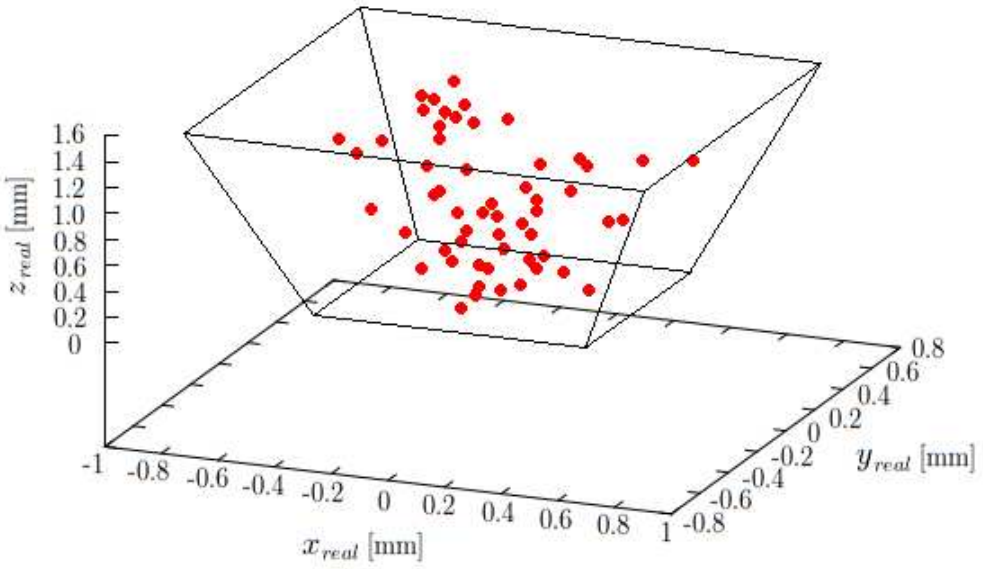

Figure V.15: A typical reconstructed volume in calibrated optical coordinates. For a conversion to usual BL coordinate directions, refer to table IV.1.

V.4 Results: Double Exposure Analysis and Tracking Algorithm

The matrices with $(x_{real}, y_{real}, z_{real})$ coordinate values stored as outputs of the particle detection processes described above can now be used as the input of a proper tracking algorithm, since they were calculated for both laser exposures. First, those coordinates are converted to BL coordinates (see table IV.1) and stored in new matrix structures. Usual BL coordinate nomenclature (x, y, z) — for streamwise, wall-normal and spanwise directions, respectively — is employed from this point on.

However, before proceeding to the application of the particle tracking algorithm in the experimental batches, a double exposure analysis was carried out based on holograms acquired in a special batch. This batch was taken with a very small time between exposures, $\Delta t = 5$ μs, which should result in small or close-to-zero displacements between particle pairs. Hence, in images created by overlapping particle coordinate points from both frames, a verification of whether the task of retrieving particle pairs had been successful or not was performed.

Images were generated by compiling points corresponding to real volume particle positions from three randomly chosen holograms from this batch, which had a slightly lower particle density than the others. Particles in different tunnel spanwise positions were also collapsed in this two-dimensional frame. Figure V.16 shows two examples of such compiled images, with particles taken from random three-hologram ensembles. Red points correspond to particles from exposure 1 and green, from exposure 2. The region depicted corresponds to $y = 0$ to 1 mm.

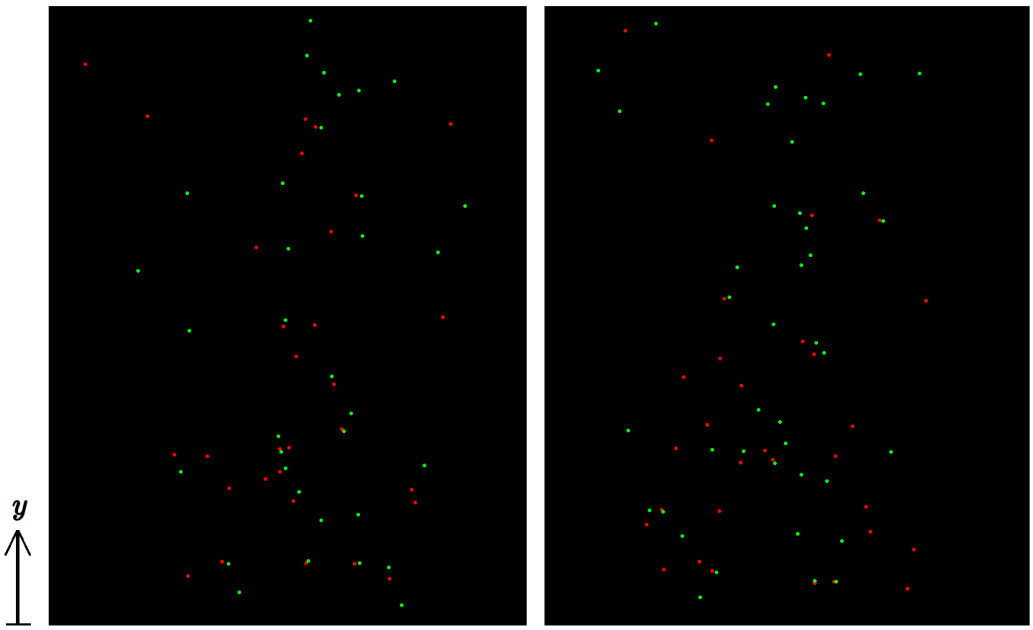

Figure V.16: Two examples of double exposure tests, each comprising particles compiled from three volumes, and also collapsed in the spanwise direction. y is the wall-normal direction, and flow is from left to right. Red particles are from exposure 1 and green particles, from exposure 2. Time between exposures is $\Delta t = 5$ μs.

In both examples shown in figure V.16, some obvious particle pairs can be spotted, but relative to the overall number of particles, they show up in a much smaller number than expected. This can be attributed to a few different

reasons, but most likely to differences in the characteristics of holograms from exposures 1 and 2. Dissimilarities in object-to-reference ratio during recording, for example, can cause holograms to reconstruct somewhat differently, that is, with some particles being detected for exposure 1 and not for exposure 2 or vice-versa. A previous analysis — computed for different batches after the particle validation process — showed that holograms from exposure 2 consistently presented a higher number of detected and validated particles in comparison to holograms from exposure 1.

Also, for the magnifications taking place in this optical setup (from ~ 9.5 in the wall plane to ~ 5.5 at a $1,5$ mm distance from the wall), reconstructed particle images are quite small, of the order of a pixel, and in some cases they can be so small they are undetected. Since detecting or not such a particle can be subtle, this can also be an issue between exposures.

Hence, images from figure V.16 point to the fact that particle retrieval from reconstructed volumes 1 and 2 is not yielding a large number of particle pairs. Software algorithms were implemented in an effective way as to detect, validate and locate particle images from this experiment, and were tested in several particle images from both frames in different batches. For this reason, we believe that the disparities found here (i.e., detecting particles in one frame that are not detected in the other and vice-versa) are due to subtle differences during recording of frames 1 and 2, despite the attempts to optimize and equalize holograms from both frames during the recording process.

For two other batches, with higher Δt, a preliminary cross-correlation analysis based on the same kind of compiled two-dimensional image was attempted, with the goal of providing a rough velocity predictor for tracking algorithm input. However, the same problems were present, since correlation was not successful. Despite these preliminary results, a particle algorithm was implemented and tested.

Particle Tracking A particle tracking algorithm was implemented as a module in *HPIVlml*. It will be briefly described here, and was tested with an experimental batch corresponding to a wind tunnel velocity of 10 m/s and matching experimental conditions of the hot-wire velocity measurements of the work by [Cuvier *et al*, 2011] (see section IV.1). Figure V.17 shows a velocity plot extracted from this work. Light blue points correspond to station 5 in the wind tunnel, the same used for measurement volume location in the holographic *PIV* experiments. Assuming these flow conditions, and using the value of u_τ estimated in this experiment (using a modified log-law), a 1.5 mm

distance from the tunnel wall would correspond to $y^+ = 44$.

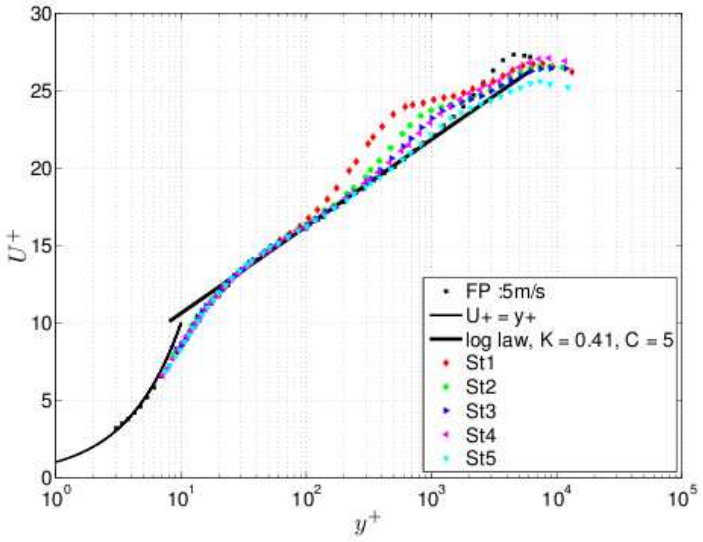

Figure V.17: Mean velocity profiles extracted from [Cuvier *et al*, 2011], $\alpha = -2^o$, $\beta = -22^o$, $U_\infty = 10$ m/s. Boundary layer characteristics evaluated in this experimental work are $\delta = 19$ cm, $\delta^* = 16.4$ mm, $\theta = 13.5$ mm, $Re_\theta = 10100$, $H = 1.21$ and $u_\tau = 0.465$ m/s.

The tracking algorithm implemented for *HPIVlml* consists of the following basic steps, given particle BL coordinates (x, y, z) from volumes 1 and 2 as input:

- Functions based on the mean velocity profiles from [Cuvier *et al*, 2011] are used as mean velocity "predictors";
- Within a loop, for every particle i from volume 1, a spherical search region is delineated to be scanned in volume 2. This search region is based on the mean velocity and fluctuation "predictors" corresponding to the particle's wall-normal position, and is illustrated in figure V.18 for a given particle from volume 1;
- A loop through all particles j in volume 2 searches for particles within the search region of particle i;
- If only one particle j is found to be a suitable pair for particle i, a match is made. Its pair j is removed from the volume 2 storage matrix, coordinates of the particle pair are stored in a pairing matrix, and loop in volume A moves on to the next particle i. If more than one particle j is found within the region in volume 2, no pairing for particle i is assumed for the moment, and loop in volume A moves on to the next particle;

– After all particles in volume 1 were analyzed, another pairing round is attempted, following the same steps. Successive rounds are attempted until no more pairs can be validated.
– Displacements between pairs stored in the final pairing matrix are computed in the three directions, and velocity-components are calculated using Δt, the time difference between exposures in the experiment.

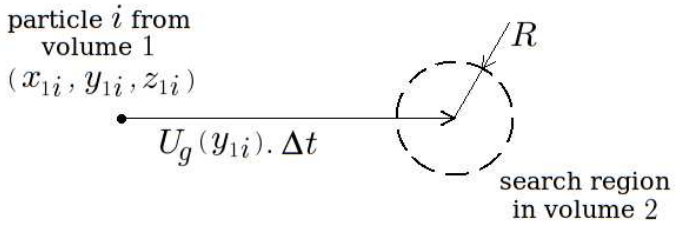

Figure V.18: Search region for particle tracking algorithm. Radius R of the search sphere is $(2u'_{guess}) \cdot \Delta t$, u'_{guess} being the fluctuation velocity guess for that wall-normal position y_{1_i}.

In order to represent mean axial velocity data (which was the primary goal for now, even if in the future it will be attempted to achieve instantaneous fields with good spatial resolution), velocity values extracted from the whole spanwise and streamwise ranges of the measurement volume were collapsed in a scatter plot U *versus* y, such as the one in figure V.19. Unfortunately, probably due to the previously described problem of possible differences in particle detection for exposures 1 and 2, and the difficulty in choosing the optimal Δt for a flow with a strong gradient, the batches that were analyzed did not provide conclusive results. This was not unexpected, given the prior double exposure test results. When slightly different functions were used for the mean velocity guess $U_g(y)$, resulting velocity data appeared to be biased by the change, specially in the near-wall region. Figure V.19 shows an example corresponding to one of the linear functions used as guess. Several different tests were made ranging from fittings of the data from [Cuvier *et al*, 2011] to linear functions with different slopes.

Trials based on the analysis of another experimental batch presented the same kind of problems. But for now, the fact that particles are being successfully reconstructed, with a signal that provides good accuracy in focal position detection and consequently an improved resolution in the tunnel wall measurement volume, is already a very positive result.

Furthermore, there are still a couple of batches to be processed and inspected in order to verify whether the same issues are present. During

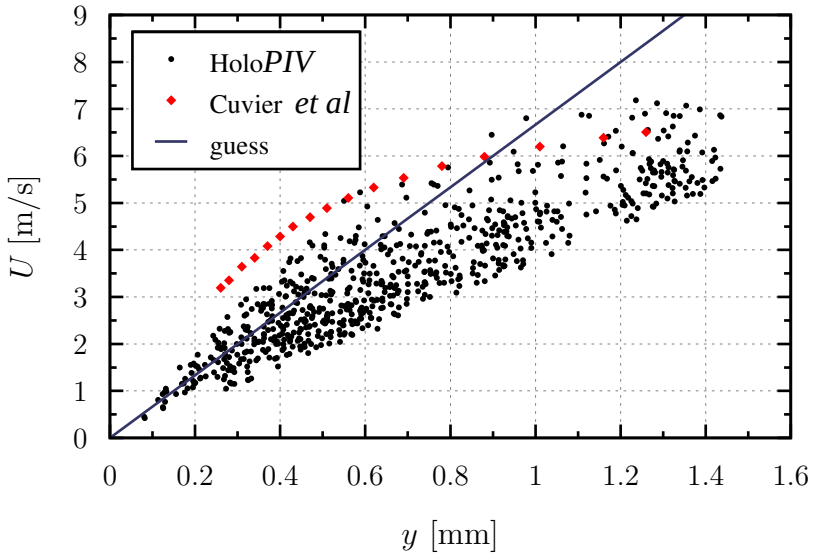

Figure V.19: Example of a velocity evaluation trial with the particle tracking code. Different guesses were tested and an apparent bias seems to occur.

recording, small adjustments were made between hologram acquisition of the different batches, so there is a possibility that the difficulties faced so far are less evident in those batches.

These and other final considerations on the results, problems encountered, adjustments to be made and future steps towards improvement of the system are presented in the next chapter.

VI
Final Considerations

In the previous chapter, as double exposure tests were carried out for a special short Δt hologram acquisition batch, and the particle tracking algorithm was applied to an experimental batch corresponding to $U_\infty = 10$ m/s, we noticed that some issues were preventing velocity data to be retrieved successfully. As a consequence, for the moment, the shear stress evaluation originally intended is not concretized.

Nevertheless, considering that the acquired batches were the outcome of the first experimental attempt to employ an optical setup which demands a number of adjustments that may not be straightforward, it can be said that many positive results arised from the different steps of the implementation — from recording to reconstruction and particle field coordinates retrieval.

The side-scattering configuration employed for the particle object field worked very well, while in-line recombination with a clean reference wave also provided advantages, allowing separate control of reference and object beams. Moreover, this configuration was able to circumvent the impossibility of using an in-line forward scattering setup in the wind tunnel. Use of a microscope objective was fundamental for improving resolution and focus detection of the particles within the reconstructed volumes. Particle "tube" images and depth evolution graphs presented in chapter V show that indeed a good axial accuracy is achieved in particle detection, which translates to a quite low uncertainty in real-volume coordinates — average, for a particle with good signal-to-noise ratio in a mid-volume position, estimated as ± 8 μm (already including uncertainty in the estimation of d_i from calibration procedure, see Appendix C). Even closer to the wall, uncertainties decay considerably, and we believe that there is still room for improvement.

Analysis of all the quantifiable uncertainties and their effect on the overall estimated uncertainty in particle streamwise displacements is presented in Appendix C, and these estimations lead us to believe that, once the necessary adjustments are made in the optical setup, the configuration can provide near-wall average velocity measurements with improved accuracy as originally

proposed. Therefore, although good velocity profiles could not be extracted for the moment, the core goal of the thesis was achieved, not only because particle signal detection results show that profiles can be measured after some adjustments as stated above, but also because in the scientific process of developing a new measuring technique configuration, facing difficulties along the way is often helpful. The challenges make one think about aspects and details that might go uninvestigated if good enough results had been achieved in the first attempt.

For the moment, further investigation of other batches from the experiment needs to be carried out, in order to investigate in more detail the possible problems leading to differences between reconstructed particle fields from exposures 1 and 2, which in turn are currently preventing a particle tracking algorithm to properly evaluate the axial velocity distribution.

After analyzing the results, some considerations about improvements in the setup arised. Most of them address factors that could improve the quality of results independently of the issue concerning differences between frames 1 and 2, meaning they would affect both frames equally. Some of these aspects that can be reconsidered in a future experimental run are:

- Positioning of the objective lens system can be reconsidered; for the current configuration, as depicted in figure IV.18, the transversal magnification achieved for imaging the measurement volume goes from ~ 9.5 at the wall to ~ 5.5 for a plane 1.5 mm away from the wall. If this range of magnifications can be slightly increased, maybe particle detection could be further improved, along with resolution;
- Use of a more sophisticated microscope objective can be considered; usually objectives are supposed to work around the nominal magnification, whereas in our case, there is a range of magnifications. Since this range is large, perhaps a lens providing correction for a varying range of working distances could avoid possible optical aberrations.
- Different times between exposures can be tested; in a high-gradient small mesurement volume, this choice can be quite difficult to optimize.
- Tests to verify whether it is possible to increase particle density within the tunnel can be done. In terms of the hologram "capacity", it is possible to aggregate interferometric data from a more dense particle field. Once the problems are overcome and validated mean axial velocity profiles can be obtained from the technique, having more reconstructed particles

might enable evaluation of other statistical flow quantities and even instantaneous velocity fields.

But most importantly, the issue of the equivalence of the reconstructed fields from frames 1 and 2 has to be addressed, as it is the main reason why the algorithms could not detect all particle pairs. Although a careful procedure was used to equalize object and reference beam characteristics from both exposures, the results of the double exposure tests presented in figure V.16 — as well as a consistent average difference in the number of detected particles from exposures 1 and 2 — lead to believe that further optimization of the equivalence between exposures is possible and necessary. Now that considerable experience has been gained in manipulating the optical setup, we believe that, in a second run, improvements can be implemented. An aspect that might play an important role is polarization. In the side-scattering mode, different polarization states can lead to different characteristics in the pattern of the light scattered by a small particle. If polarization is not the same for beams 1 and 2, it is possible that this can contribute to slightly different interference patterns, and consequently to reconstructed particle image signals with distinct characteristics. Also, an even more solid and practical mounting arrangement can be implemented.

Having pointed out the issues that need to be considered and improved, it is important to emphasize one more time that the particle field reconstruction results shown in chapter V are quite positive. Those results alone are already a large step towards performing holographic *PIV* measurements in a facility such as the LML wind tunnel.

Thus, although average wall shear stress evaluation was not achieved to the moment, we have reasons to believe that — after the implementation of adjustments addressing the issues encountered here, it will, and uncertainty can be very low. Additionally, the whole software structure that was implemented is a valuable tool, ready to be used in future holographic experiments. As far as the thesis is concerned — its focus being in the initial development of the technique — most of the basis for a successful implementation of the proposed configuration was created and tested. Preliminary results are promising and provided some interesting discussions in terms of future adjustments.

Bibliography

[Adrian and Westerweel, 2011] R. Adrian and J. Westerweel. **Particle image velocimetry**. Cambridge University Press, New York, 2011. I.2.1

[Amili and Soria, 2009] O. Amili and J. Soria. **Measurements of near wall velocity and wall stress in a wall-bounded turbulent flow using digital holographic microscopic piv and shear stress sensitive film**. In *Progress in Wall Turbulence: Understanding and Modeling: Proceedings of the WALLTURB International Workshop in Lille, France*, 2009. I.2.1, I.2.2, I.2.2

[Atkinson *et al*, 2008] C. Atkinson, C. Dillon-Gibbons, S. Herpin and J. Soria. **Reconstruction techniques for tomographic piv (tomo-piv) of a turbulent boundary layer**. In *14th International Symposium on Applications of Laser Techniques to Fluid Mechanics, Lisbon, Portugal*, 2008. I.2.1

[Barnhart *et al*, 1994] D. Barnhart, R. Adrian and G. Papen. **Phase-conjugate holographic system for high-resolution particle-image velocimetry**. *Applied Optics*, 33(30):7159–7170, 1994. II.6

[Barricau *et al*, 2009] P. Barricau, G. Pailhas and Y. Touvet. **Friction measurement in zero and adverse pressure gradient boundary layer using oil droplet interferometric method**. In *Progress in Wall Turbulence: Understanding and Modeling: Proceedings of the WALLTURB International Workshop in Lille, France*, 2009. I.2.2

[Cao *et al*, 2008] L. Cao, G. Pan, J. de Jong, S. Woodward and H. Meng. **Hybrid digital holography imaging system for three-dimensional dense particle field measurement**. *Applied Optics*, 47(25):4501–4508, 2008. I.3

[Carlier and Stanilas, 2005] J. Carlier and M. Stanislas. **Experimental study of eddy structures in a turbulent boundary layer using particule image velocimetry**. *Journal of Fluid Mechanics*, 535(36):143–188, 2005. IV.1

[Chan *et al*, 1996] K. Chan, T. Leung and Y. Li. **Holographic imaging of side-scattering particles**. *Optics & Laser Technology*, 28(8):565–571, 1996. II.6

[Chan and Li, 1998] K. Chan and Y. Li. **Pipe flow measurement by using a side-scattering holographic particle imaging technique**. *Optics & Laser Technology*, 30:7–14, 1998. II.6

[Cuche *et al*, 1999] E. Cuche, P. Marquet and C. Depeursinge. **Simultaneous amplitude-contrast and quantitative phase-contrast microscopy by numerical reconstruction of fresnel holograms**. *Applied Optics*, 38(34):6994–7001, 1999. II.5

[Cuvier *et al*, 2011] C. Cuvier, C. Braud, J. Foucaut and M. Stanislas. **Characterization of a separated turbulent boundary layer for flow control purpose**. *in submission*, 2011. (document), IV.1, IV.2, V.1, V.4, V.17, V.4, V.4

[Dubois *et al*, 1999] F. Dubois, L. Joannes and J. Legros. **Improved three-dimensional imaging with a digital holography microscope with a source of partial spatial coherence**. *Applied Optics*, 38(34):7085–7094, 1999. II.5

[Dubois *et al*, 2006] F. Dubois, N. Callens, C. Yourassowsky, M. Hoyos, P. Kurowski and O. Monnom. **Digital holographic microscopy with reduced spatial coherence for three-dimensional particle flow analysis**. *Applied Optics*, 45(5):864–871, 2006. II.5

[Elsinga *et al*, 2006] G. Elsinga, F. Scarano, B. Wieneke and B. van Oudheusden. **Tomographic particle image velocimetry**. *Experiments in Fluids*, 41(6):933–947, 2006. I.2.1

[Elsinga *et al*, 2007] G. Elsinga, R. Adrian, B. van Oudheusden and F. Scarano. **Tomographic-piv investigation of a high reynolds number turbulent boundary layer**. In *7th International Symposium on PIV, Rome, Italy*, 2007. I.2.1

[Goodman and Lawrence, 1967] J. Goodman and R. Lawrence. **Digital image formation from electronically detected holograms**. *Applied Physics Letters*, 11:77–79, 1967. II.4

[Goodman, 1968] J. Goodman. **Introduction to fourier optics**. McGraw-Hill, San Francisco, 1968. II.1, II.4, III.2, IV.3

[Hanratty and Brooke, 1993] J. Brooke and T. Hanratty. **Origin of turbulence-producing eddies in a channel flow**. *Physics of Fluids A*, 5:1011–1022, 1993. I.1

[Johansson, 2009] T. G. Johansson. **Near wall measurements and wall shear stress**. In *Progress in Wall Turbulence: Understanding and Modeling: Proceedings of the WALLTURB International Workshop in Lille, France*, 2009. I.2.2, I.2.2

[Kähler *et al*, 2006] C. Kähler, U. Scholz and J. Ortmanns. **Wall-shear-stress and near-wall turbulence measurements up to single pixel resolution by means of long- distance micro-piv**. *Experiments in Fluids*, 41:327–341, 2006. I.2.2, I.2.2

[Kline *et al*, 1967] S. Kline, W. Reynolds, F. Schraub and P. Runstadler. **The structure of turbulent boundary layers**. *Journal of Fluid Mechanics*, 30(4):741–773, 1967. I.1

[Konrath *et al*, 2002] R. Konrath, W. Schröder and W. Limberg. **Holographic particle image velocimetry applied to the flow within the cylinder of a four-valve internal combustion engine**. *Experiments in Fluids*, 33:781–793, 2002. II.6

[Kravchenko *et al*, 1993] A.G.Kravchenko, H.Choi and P.Moin. **On the relation of near-wall streamwise vortices to wall skin friction in turbulent boundary layers**. *Physics of Fluids A*, 5:3307–3309, 1993. I.1

[Kreis *et al*, 1997] T. Kreis, M. Adams and W. Juptner. **Methods of digital holography: a comparison**. *Proc. SPIE*, 3098:224–233, 1997. II.4

[Kronrod *et al*, 1972] M. Kronrod, N. Merzlyakov and L. Yaroslavskii. **Reconstruction of a hologram with a computer**. *Sov. Phys. - Tech. Phys.*, 17:333–334, 1972. II.4

[Löfdahl *et al*, 2003] L. Löfdahl, V. Chernoray, S. Haasl, G. Stemme and M. Sen. **Characteristics of a hot-wire microsensor for time-dependent wall shear stress measurements**. *Experiments in Fluids*, 35:240–251, 2003. I.2.2

[Meng *et al*, 1993] H. Meng, W. Anderson, F. Hussain and D. Liu. **Intrinsic speckle noise in in-line particle holography**. *Journal of the Optical Society of America*, 10(9):2046–2058, 1993. II.6

[Meng and Hussain, 1995] H. Meng and F. Hussain. **In-line recording and off-axis viewing technique for holographic particle image velocimetry**. *Applied Optics*, 34(11):1827–1840, 1995. II.6

[Meng *et al*, 2004] H. Meng, G. Pan, Y. Pu and S. Woodward. **Holographic particle image velocimetry: from film to digital recording**. *Measurement Science and Technology*, 15:673–685, 2004. (document), I.2.1, II.4, II.11, II.6

[Naughton and Sheplak, 2002] J. Naughton and M. Sheplak. **Modern developments in shear-stress measurement**. *Progress in Aerospace Sciences*, 38:515–570, 2002. I.2.2, I.2.2

[Ng *et al*, 2007] H. Ng, J. M. I. Marusic, N. Hutchins and M. Chong. **Oil film interferometry in high reynolds number turbulent boundary layers**. In *16th Australasian Fluid Mechanics Conference, Crown Plaza, Gold Coast, Australia*, 2007. I.2.2

[Palero *et al*, 2007] V. Palero, M. Arroyo and J. Soria. **Digital holography for micro-droplet diagnostics**. *Experiments in Fluids*, 43(2):185–195, 2007. III.2, III.2

[Pan and Meng, 2003] G. Pan and H. Meng. **Digital holography of particle fields: reconstruction by use of complex amplitude**. *Applied Optics*, 42(5):827–833, 2003. II.6, III.2

[Prasad, 2000] A. Prasad. **Stereoscopic particle image velocimetry**. *Experiments in Fluids*, 29:103–116, 2000. I.2.1

[Pu and Meng, 2000] Y. Pu and H. Meng. **An advanced off-axis holographic particle image velocimetry (hpiv) system**. *Experiments in Fluids*, 29:184–197, 2000. (document), II.6, II.16, II.6

[Pu and Meng, 2003] Y. Pu and H. Meng. **Intrinsic aberrations due to mie scattering in particle holography**. *Journal of the Optical Society of America*, 20(10):1920–1932, 2003. II.6, II.6

[Pu and Meng, 2004] Y. Pu and H. Meng. **Intrinsic speckle noise in off-axis particle holography**. *Journal of the Optical Society of America*, 21(7):1221–1230, 2004. II.6

[Pu and Meng, 2005] Y. Pu and H. Meng. **Four-dimensional dynamic flow measurement by holographic particle image velocimetry**. *Applied Optics*, 44(36):7697–7708, 2005. II.6

[Robinson,1991] S. Robinson. **Coherent motions in the turbulent boundary layer**. *Annual Review of Fluid Mechanics*, 23:601–639, 1991. I.1

[Ruedi *et al*, 2003] J. Ruedi, H. Nagib, J. Osterlünd and P. Monkewitz. **Evaluation of three techniques for wall-shear measurements in three-dimensional flows**. *Experiments in Fluids*, 35:389–396, 2003. I.2.2, I.2.2

[Schlichting, 1979] H. Schlichting. **Boundary layer theory**. McGraw-Hill, 1979. I.1

[Schnars and Juptner, 1994] U. Schnars and W. Juptner. **Direct recording of holograms by a ccd target and numerical reconstruction**. *Applied Optics*, 33:179–181, 1994. I.2.1, II.4

[Scherer and Bernal, 1997] J. Scherer and L. Bernal. **In-line holographic particle image velocimetry for turbulent flows**. *Applied Optics*, 36(35):9309–9318, 1997. II.6

[Schroeder and Willert, 2008] A. Schroeder and C. Willert. **Particle image velocimetry: new developments and recent applications**. Springer, Berlin, 2008. I.2.1

[Sheng *et al*, 2006] J. Sheng, E. Malkiel and J. Katz. **Digital holographic microscope for measuring three-dimensional particle distributions and motions**. *Applied Optics*, 45(16):3893–3901, 2006. (document), II.5, II.15

[Sheng *et al*, 2008] J. Sheng, E. Malkiel and J. Katz. **Using digital holographic microscopy for simultaneous measurements of 3d near wall velocity and wall shear stress in a turbulent boundary layer**. *Experiments in Fluids*, 2008. (document), I.2.1, I.2.2, I.2, I.3, II.6

[Tropea *et al*, 2007] C. Tropea, A. Yarin and J. Foss. **Springer handbook of experimental fluid mechanics**. Springer, Berlin, 2007. I.2.2

[Young, 2000] M. Young. **Optics and lasers - including fibers and optical waveguides**. Springer, Berlin, 2000. II.1

[Zhang *et al*, 1997] J. Zhang, B. Tao and J. Katz. **Turbulent flow measurement in a square duct with hybrid holographic piv**. *Experiments in Fluids*, 23:373–381, 1997. II.6

[deJong and Meng, 2007] J. de Jong and H. Meng. **Digital holographic particle validation via complex wave**. *Applied Optics*, 46(31):7652–7661, 2007. V.3

A
Holographic Imaging: Image Locations, Magnification, and Wave Representation

This appendix provides a brief explanation about the holographic imaging process in a more general case. In chapter II, in which recording and reconstruction processes are introduced, although it was mentioned that in many cases the reconstruction wave is non-collimated and might also not be an exact replica of the reference wave, it was assumed that reference and reconstruction waves were identical.

In chapter IV, the holographic equations that will be presented here are used, in order to obtain the final calibration expressions that can correctly relate the coordinates of the volume reconstructed with *HPIVlml* software to the wind tunnel wall coordinates. In that chapter, an assumption was made of a $1:1$ holographic imaging process. This will be further clarified here.

The holographic imaging equations can predict position and magnification of reconstructed point source images for the more general case of non-collimated, non-identical waves. They can also account for effects of using laser sources of different wavelengths in recording and reconstruction, but here it will be assumed that $\lambda_R = \lambda_{R'}$.

Figure A.1 represents the recording and reconstruction geometries, respecting coordinates and signs from figure IV.18 presented in the calibration discussions in chapter IV. Here, an object point source p is considered. This illustrative point source could be any point within the object field. Such a simplified analysis would be valid for any given point in space, and is valid, by superposition, for their combination, i.e., for the object field as a whole.

In figure A.1, in which the **hologram reference frame** Z from figure IV.18 is used, Z_p is the distance from the object source to the hologram plane. In comparison to figure IV.18, it corresponds to Z_{ip}, and that is because in chapter IV an "i" was added before the"p" in the index to indicate that the

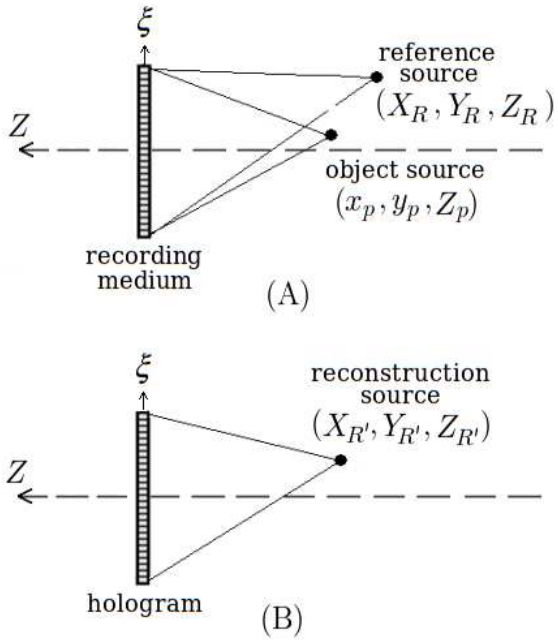

Figure A.1: Holographic (A) recording and (B) reconstruction geometries with respect to hologram frame from figure IV.18. Reference wave is generated by a point source located at coordinates (X_R, Y_R, Z_R). The object point source p is located at coordinates (x_p, y_p, Z_p). During reconstruction step, the hologram is assumed to be illuminated by a spherical wave originating from a point source at coordinates $(X_{R'}, Y_{R'}, Z_{R'})$. In the thesis experiment, both object and reference sources are located in the right side of the figure and are diverging waves, whereas the location of reconstruction wave source in the figure is in the right side, but can actually be chosen to be either in the left or the right side in the numerical implementation.

object point was part of a magnified object field, which was already the output of another imaging process (the objective lens imaging process $\S_I \mapsto \S_{II}$, see chapter IV).

Both Z_R, $Z_{R'}$ and Z_p are negative numbers for point sources lying to the right of the hologram recording plane (i.e., for diverging spherical waves), and positive numbers for points lying to the left of that plane in the figure (i.e., for converging spherical waves). This difference is explained in more detail in figure A.2, more specifically for the reconstruction wave R'. In situation (B.1), the reconstruction wave is diverging, with its source located at a negative position $Z_{R'} < 0$. In (B.2), the reconstruction source is located at a positive position $Z_{R'} > 0$ and the wave is converging.

This is illustrated here because in the numerical reconstruction process, we can choose either (B.1) or (B.2) as the reconstruction wave. In the hologram plane, both of them are modeled in the form

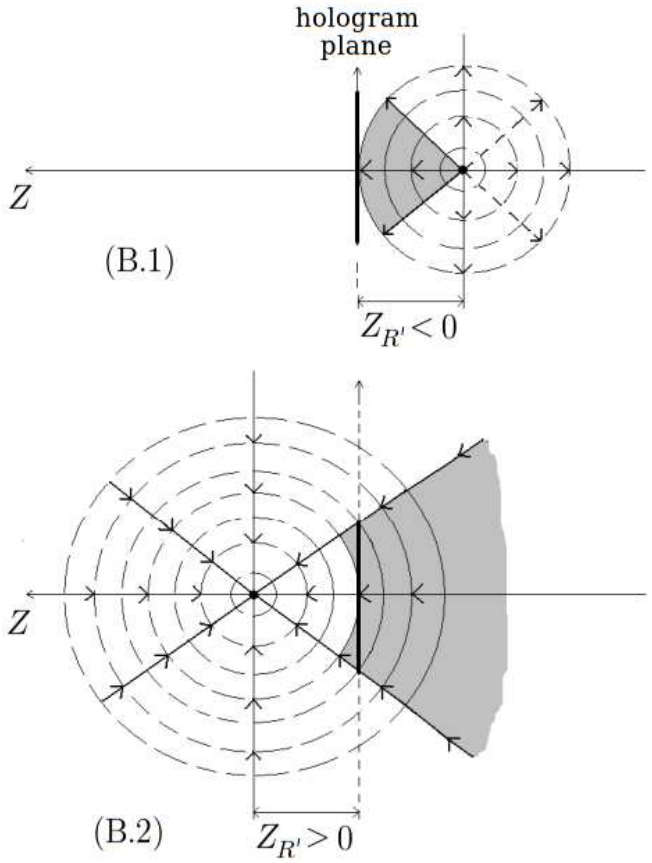

Figure A.2: Two different possibilities for reconstruction situation (B) in figure A.1: in (B.1), the reconstruction wave is diverging, thus having its source located at a negative position $Z_{R'} < 0$. In (B.2), the reconstruction wave is converging, with source located at a positive position $Z_{R'} > 0$. Here, in both cases, simply to facilitate visualization, $X_{R'}$ and $Y_{R'}$ have been set to zero (whereas in figure A.1 generic values are attributed), corresponding to waves centerd in the optical axis, that is, $R'(\xi,\eta) = \exp\left\{-\frac{j\pi}{\lambda Z_{R'}}\left[\xi^2+\eta^2\right]\right\}$.

$$R'(\xi,\eta) = \exp\left\{-\frac{j\pi}{\lambda Z_{R'}}\left[(\xi - X_{R'})^2 + (\eta - Y_{R'})^2\right]\right\}, \tag{A.1}$$

only varying the sign of $Z_{R'}$, as long as proper use of the holographic equations presented next follows this choice. If $X_{R'} = Y_{R'} = 0$, the wave is centered in the optical axis, as represented in figure A.2 for better visualization. In *HPIVlml* software, the reconstruction wave is represented as in B.2, but this was not mandatory.

Based on figures A.1 and A.2, the proper equations for the holographic imaging system can be written. The point source image is reconstructed at the distance Z'_p from the hologram given by

$$Z'_p = \frac{1}{\left(\frac{1}{Z_{R'}} \pm \frac{1}{Z_R} \mp \frac{1}{Z_p}\right)}, \tag{A.2}$$

and the lateral coordinates (x'_p, y'_p) of the image point are given by

$$\frac{x'_p}{Z'_p} = \mp\frac{x_p}{Z_p} \pm \frac{X_R}{Z_R} + \frac{X_{R'}}{Z_{R'}} \tag{A.3}$$

$$\frac{y'_p}{Z'_p} = \mp\frac{y_p}{Z_p} \pm \frac{Y_R}{Z_R} + \frac{Y_{R'}}{Z_{R'}}. \tag{A.4}$$

The upper set of signs applies for one image wave and the lower set of signs to the other. When Z'_p is negative, the image is virtual and lies to the right of the hologram, while in the case of a positive Z'_p, the image is real and lies to the left of the hologram in figure A.1.

The transverse and axial magnifications are given by

$$M_{xy} = |1 - \frac{Z_p}{Z_R} \mp \frac{Z_p}{Z_{R'}}|^{-1}, \tag{A.5}$$

$$M_z = {M_{xy}}^2. \tag{A.6}$$

When reference and reconstruction waves are collimated, a $1:1$ imaging process occurs, and $|Z'_p| = |Z_p|$, $|x'_p| = |x_p|$, $|y'_p| = |y_p|$, $M_t = M_a = 1$. In the context of the thesis experiment, reference wave is diverging, and in chapter IV an assumption was made that absolute source distances were identical, with R' being represented numerically as a spherical converging wave as in (B.2), so that $Z_{R'} > 0$, $Z_R < 0$ and $|Z_{R'}| = |Z_R|$. In this case, one of the images is reconstructed so that $|Z'_p| = |Z_p|$ and $M_t = M_a = 1$, but the other not. Hence, the upper set of signs was chosen such that a $1:1$ holographic imaging process could be assumed. Waves were also assumed to be centered in the axis.

In the end, given the experimental configuration and numerical implementation chosen in the thesis, object points were reconstructed on the opposite side of the original positions, in the positive Z axis, along space $\S_{III}$. That is, $Z_p < 0$, $Z'_p > 0$, $|Z'_p| = |Z_p|$, and magnifications are equal to 1. Of course, departures from the assumptions can cause errors.

B
Discretization in the Numerical Reconstruction Process

Here, implementation of the discretized functions involved in numerical reconstruction are quickly described. Digital holograms are discrete sets of numbers (grey level values), $H(K,L)$, with $K = 0 : (M-1)$ and $L = 0 : (N-1)$, the CCD sensor being an $M \times N$ matrix of square pixels with size Δ.

To implement the convolution operation from equation (II.4.13) in the discrete form, the first step is to multiply the grey-level distribution from the hologram image, pixel by pixel, by the corresponding local pixel value of the reconstruction wavefield in that plane. For that, it is important to verify the way images (and therefore the hologram image) are handled and stored in the computational image structure. As implemented in the *HPIVlml* code, the origin is not located in the center of the images, but in the corner as depicted in figure B.1, so that the discrete form of the reconstruction wavefront implemented in the code has to take that into account as:

$$R'(K,L) = \exp\left\{-\frac{j\pi}{Z_{R'}\lambda}\left[\left(\Delta\left(K-\frac{M-1}{2}\right)\right)^2+\left(\Delta\left(L-\frac{N-1}{2}\right)\right)^2\right]\right\}. \tag{B.1}$$

The next step in the implementation is the application of the first two-dimensional discrete Fourier transform operation, $DFT\{H.R'\}$, generating a pair of real/imaginary images. The discrete transform (represented above as DFT) decomposes a sequence of values into components of different spatial frequencies $f_x = \frac{K}{M(\Delta\xi)}$ and $f_y = \frac{L}{N(\Delta\eta)}$. A Fast Fourier Transform (FFT), which was implemented here, is a way to compute the result of the DFT more quickly (see www.fftw.org).

The transfer function $H_{Z'}$ is discretized as

$$H_{Z'}(K,L) = \exp\left\{-j\pi\lambda Z'\left[\left(\frac{K-\frac{M-1}{2}}{M\Delta}\right)^2+\left(\frac{L-\frac{N-1}{2}}{N\Delta}\right)^2\right]\right\} \tag{B.2}$$

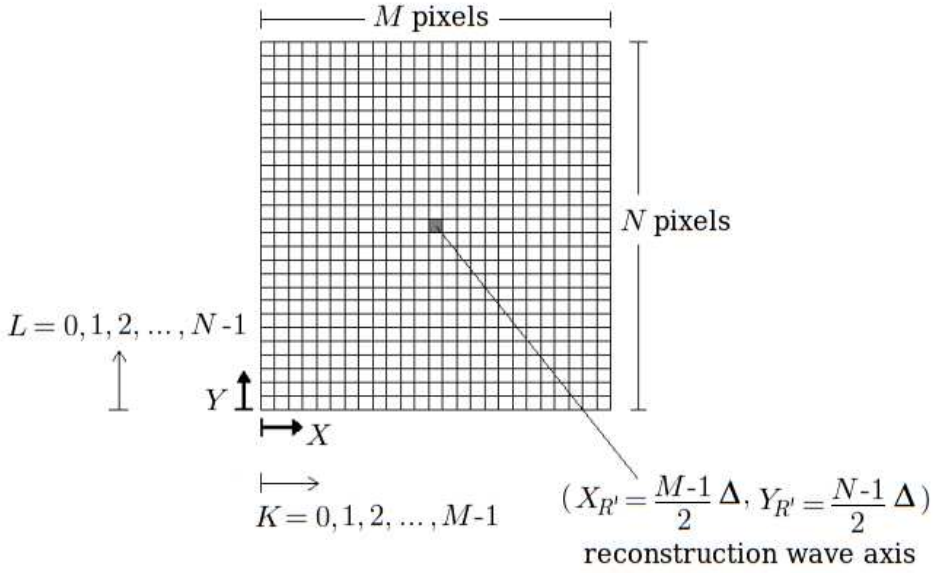

Figure B.1: Discretization in numerical reconstruction implementation. Reconstruction wave is centered in the optical axis.

The previous pair of images then goes through complex multiplication with the transfer function values as calculated from (B.2), and finally a discrete inverse transform operation is performed, generating a new pair of images that constitute the reconstructed complex field in the plane in question:

$$b'(K,L) = e^{jkz} DFT^{-1}\{DFT\{H.R'\}H_z\}. \tag{B.3}$$

Image $b'[0](K,L)$ is the real part of the reconstructed complex field, and image $b'[1](K,L)$ is the imaginary part.

C
Uncertainty Analysis

An analysis for uncertainty estimation in the evaluation of final particle positions and displacements is described here.

Real-volume depth coordinate z_{real_p} for a particle p in the measurement volume is given — as presented in chapter IV — by the following expression:

$$z_{real_p}(Z'_{i_p}) = \left[d_o - \frac{f(d_i - Z'_{i_p})}{f - (d_i - Z'_{i_p})} \right] - \varepsilon, \tag{C.1}$$

whereas the transversal magnification M_{t_p} in the particle's plane is given by

$$M_{t_p}(Z'_{i_p}) = \frac{f - d_i + Z'_{i_p}}{f}, \tag{C.2}$$

d_i and d_o being the imaging parameters evaluated from the pinhole calibration procedure, f the focal length of the objective lens, and ε a constant value. Value of d_o is calculated from d_i through the lens equation.

Hence, the uncertainty in z_{real_p} can be estimated from the uncertainties in d_i and in the estimation of Z'_{i_p} with the particle detection algorithms:

$$\delta z_{real_p} = \sqrt{\left(\frac{\partial z_{real_p}}{\partial d_i} \right)^2 (\delta d_i)^2 + \left(\frac{\partial z_{real_p}}{\partial Z'_{i_p}} \right)^2 \left(\delta Z'_{i_p} \right)^2}. \tag{C.3}$$

Analogously, uncertainty in M_{t_p} can be estimated by

$$\delta M_{t_p} = \sqrt{\left(\frac{\partial M_{t_p}}{\partial d_i} \right)^2 (\delta d_i)^2 + \left(\frac{\partial M_{t_p}}{\partial Z'_{i_p}} \right)^2 \left(\delta Z'_{i_p} \right)^2}. \tag{C.4}$$

From chapter IV, we know that the standard error in the evaluation of d_i through the pinhole holograms is $SE_{d_i} = 1.233mm = \delta d_i$. Also, from chapter V, we have $\delta Z'_{i_p} = 0.125mm$ for a particle with good signal-to-noise ratio.

Thus, after evaluating the dependency terms with a discrete incremental variation around the average value of d_i and around Z'_i corresponding to a mid-volume particle position, we have:

- $\delta z_{real_p} \sim 8\mu m$;
- $\delta M_{t_p} \sim 0.05$.

For a particle at a $0.1mm$ distance from the wall, δz_{real_p} goes to $\sim 4\mu m$.

As the lateral positions (x_{real}, y_{real}) are calculated from the transversal magnifications, their uncertainties can be estimated from δM_{t_p}. For a particle positioned in the measurement volume mid-height, experimenting an axial displacement of 1/4 of the lateral dimension of the volume, it is found that the uncertainty in the estimation of this particle displacement is around $\pm 2\mu m$.

Vélocimetrie par image de particules holographique pour les mesures de turbulence de paroi

L'amélioration continuée de la compréhension de la dynamique de la turbulence de paroi a été l'objectif de nombreuses études éxperimentales et numériques depuis de décennies. Le principal aspect pratique qui fait de cette conaissance si crucial est le fait que la contrainte de cisaillement pariétale est étroitement liée à la dynamique des structures turbulentes. Les techniques expérimentales en mécanique des fluides ont également connu un grand montant des avances ces dernières années. Cet ouvrage présente le développement d'une configuration expérimentale visant à fournir des mesures 3D-3C de l'écoulement dans la région proche de la paroi d'une installation de grande soufflerie, conduisant à l'évaluation de la contrainte de cisaillement à la paroi avec une précision améliorée. Avec cet objectif, une technique connue sous le nom de vélocimetrie par images de particules holographique est utilisée, et les mésures sont effectuées dans de petits volumes à proximité de la paroi dans la soufflerie au Laboratoire de Mécanique de Lille (LML). Mesures complètes dans des volumes aussi petits que 1.5mm^3 sont rendues possibles grâce l'utilisation d'un objectif de microscope pour l'agrandissement du champ objet. Les particules sont éclairées par le côté, le champ se disperse a 90^o et se recombine en ligne avec l'onde de référence pour l'enregistrement holographique. Une procédure d'étalonnage est réalisée afin de relier l'espace de reconstruction à de véritables coordonnées de volume de mesure. L'analyse de résultat des champs de particules montre que des images de particules sont reconstruits avec très bonne résolution axiale, ce qui conduit à croire que la configuration est en effet adaptée à cette type de mesure. Cependant, quelques optimisations et ajustements pourraient être nécessaires afin d'améliorer les résultats de *tracking* de particules.

Mots-clés: contrainte de cisaillement, holographie, turbulence de paroi, PIV

Holographic particle image velocimetry for wall turbulence measurements

Constinuously improving the understanding of wall turbulence dynamics has been the goal of many experimental and numerical studies for decades. The main practical aspect that makes this knowledge so crucial is the fact that the wall shear stress is closely related to the dynamics of the near-wall structures. Experimental techniques in fluid mechanics have also experienced a great amount of advances in recent years. The present work details the development

of an experimental configuration aimed at providing 3D-3C flow measurements in the very near-wall region of a large wind tunnel facility, which can lead to the assessment of the wall shear stress with improved accuracy. With that goal, a technique known as *Holographic Particle Image Velocimetry* is used, and measurements are made in small volumes close to the wall in the wind tunnel at the *Laboratoire de Mécanique de Lille*. Full measurements in volumes as small as 1.5 mm^3 are made possible with the use of a microscope objective for magnification of the object field. Particles are illuminated from the side and the 90^o scattered field recombines with reference wave for holographic in-line recording. A calibration procedure is performed in order to relate reconstruction space coordinates to real measurement volume coordinates. Analysis of resulting particle fields shows that particle images reconstruct with very good axial accuracy, leading to believe that the configuration is indeed suited for this type of measurement. However, in this first attempt to use this configuration, despite careful alignments and adjustments, the inherent sensitivity of the coherent holographic process with respect to different factors prevented particles from being detected with enough equivalence in *PIV* frames 1 and 2, and not all particle pairs could be retrieved successfully. Thus, some optimizations and adjustments which might be needed in order to improve the particle tracking results are discussed. Nevertheless, results are promising and discussions about them provide interesting insight to some important issues.

Keywords: shear stress, holography, wall turbulence, HPIV